# Highly Efficient Organic Devices Based on Electrically Doped Transport Layers

K. Walzer, B. Maennig, M. Pfeiffer, and K. Leo*

*Institut für Angewandte Photophysik, Technische Universität Dresden, 01062 Dresden, Germany*

*Received August 25, 2006*

## Contents



## 1. Introduction

Most present-day semiconductor devices use inorganic crystalline materials, with single-crystalline silicon dominating other materials like GaAs by about a factor of 1000. Despite the advantages of single-crystalline inorganic semiconductors like high room-temperature mobility (up to 1000 $cm^2/(V\ s)$) and high stability, these materials are less suitable for low-cost and large-area applications. Additionally, silicon is an indirect semiconductor and therefore is not well suited for optoelectronic applications like light-emitting diodes. Solar cells from silicon are expensive and require a large amount of energy for their fabrication, leading to a long energy payback time.

As an alternative, organic semiconductors have recently gained much attention (for review articles, see refs 1−3 (OLEDs), ref 4 (organic electronics in general), and refs 5 and 6 (organic solar cells)). Originally, much of the research concentrated on single crystals, which can have mobilities of a few $cm^2/(V\ s)$ at room temperature and even much higher values at low temperature, as shown in the pioneering work of Karl et al.[7] However, for practical applications, thin-film organic semiconductors with disordered morphology, such as evaporated small-molecule compounds or polymers processed from solution, are prevailing. Organic semiconductors are already broadly applied as photoconductors for copiers and laser printers.

* Corresponding author. E-mail: leo@iapp.de. Web address: www.iapp.de.

10.1021/cr050156n CCC: $65.00 
Published on Web 03/27/2007

Karsten Walzer was born in 1969. He studied at the Technische Universität Chemnitz, Germany, where he received both his Diploma (in 1995) and Ph.D. degrees in physics (2000). The work during his time in Chemnitz dealt mainly with scanning probe microscopies, with a focus on scanning tunneling microscopy and spectroscopy of organic–inorganic interfaces. During a postdoctoral stay from 2000 to 2002 in the molecular electronics group of Kurt Stokbro at Mikroelektronik Centret in Copenhagen, he continued this work, now with focus on the basic properties of molecular electronic devices made from nanocrystals or self-assembled monolayers. In late 2002, he joined the group of Karl Leo at Technische Universität Dresden, where he refocused his work to the development organic light-emitting diodes, which now is his main field of work. Since 2004, he is head of the Organic Light Emitting Diodes development group at Technische Universität Dresden.

Bert Männig studied physics in Bonn and Dresden. He obtained the Diplomphysiker degree from the University of Dresden in 2000. In 2004, he obtained the Ph.D. degree from the Technische Universität Dresden for his Ph.D. thesis about organic solar cells under supervision of Prof. K. Leo. From 2004 to 2005, he worked as a system engineer at the computer distributor company Bytec GmbH, Friedrichshafen. Since 2005, he has been a scientific co-worker at the Institut für Angewandte Photophysik, Technische Universität Dresden, and since 2006 he is leading the Organic Solar Cell group. His main interests are organic semiconductors and novel structures of highly efficient organic solar cells. In 2001, he was awarded with the Harry Dember Preis of the Zentrum für Angewandte Photonik Dresden acknowledging his diploma work in the field of doped organic semiconductors. Together with Prof. Dr. Karl Leo, Prof. Dr. Peter Bäuerle, Dr. Martin Pfeiffer, Jens Drechsel, and Dr. Harald Eggers, he founded the spin-off company Heliatek GmbH in 2006, which is focused on research, development, and production of organic photovoltaics and devices.

Martin Pfeiffer studied physics in Tübingen, Lancaster, and Dresden. He prepared his diploma thesis at the Technische Universität (TU) Dresden under supervision of Prof. Norbert Karl, Universität Stuttgart, and obtained his degree in 1995. In 2000, he obtained the Ph.D. degree from the TU Dresden for a thesis on "Doping of organic semiconductors for use in organic LED and organic solar cells" supervised by Karl Leo. From 2000 to 2006, he led the Organic Optoelectronics Group of the Institut für Angewandte Photophysik, TU Dresden. In 2002, he worked for 4 months at Princeton University as a Visiting Research Fellow in the group of Stephen Forrest. Together with Prof. Dr. Karl Leo, Prof. Dr. Peter Bäuerle, Dr. Bert Männig, Jens Drechsel, and Dr. Harald Eggers, he founded the spin-off company Heliatek GmbH in 2006, which is focused on research, development, and production of organic photovoltaics and devices.

Karl Leo obtained the Diplomphysiker degree from the University of Freiburg in 1985, working with Adolf Goetzberger at the Fraunhofer-Institut für Solare Energiesysteme. In 1988, he obtained the Ph.D. degree from the University of Stuttgart for a Ph.D. thesis performed at the Max-Planck-Institut für Festkörperforschung in Stuttgart under supervision of Hans Queisser. From 1989 to 1991, he was a postdoctoral fellow at AT&T Bell Laboratories in Holmdel, NJ. From 1991 to 1993, he was with the Rheinisch-Westfälische Technische Hochschule (RWTH) in Aachen, Germany. Since 1993, he has been full professor of optoelectronics at the Technische Universität Dresden; since 2002, he has also been at the Fraunhofer-Institute for Photonic Microsystems, presently as deputy director. His main current interests are novel semiconductor systems like semiconducting organic thin films with special emphasis to understand growth, basic device principles, and optical response. Recently, he has also worked on device development, such as highly efficient organic LED and solar cells. His work was recognized by several awards, including the Leibniz-Award (2002) by the DFG.

Organic semiconductors have several unique physical properties, which offer many advantages compared with inorganic semiconductors: (i) The extremely high absorption coefficients of some organic dyes in the visible range offer the possibility to prepare very thin photodetectors and photovoltaic cells.[8] (ii) Many fluorescent dyes emit strongly red-shifted to their absorption. Thus, there are almost no reabsorption losses in organic light-emitting diodes,[9] which, together with the low indices of refraction, circumvents the key problems of inorganic LEDs. (iii) Since organic semiconductors consist of molecular structures with saturated electron systems, the number of intrinsic defects in disordered systems is much lower than that in inorganic amorphous semiconductors having a large number of dangling bonds.

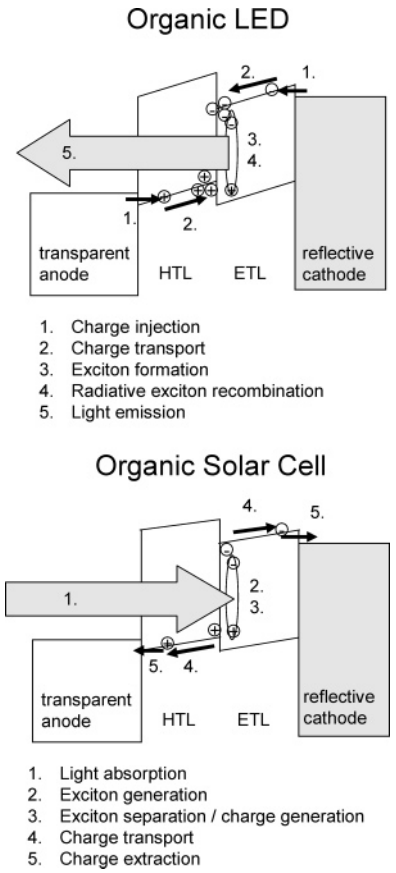


**Figure 1.** General operation principle of an OLED and an organic solar cell in comparison. For simplicity, we show two-layer devices. In the field of small molecule organic electronics, usually additional layers are used to improve the efficiency of the devices. Nevertheless, all these devices follow the general layout as sketched here.

(iv) A nearly unlimited number of chemical compounds is available, and it is possible to prepare tailor-made materials. (v) Organic semiconductors can usually be deposited on room-temperature substrates and are very well compatible with flexible substrates.

Currently, a large part of the work on organic semiconductor devices is addressing organic light-emitting diodes (OLEDs) and organic solar cells (OSCs). Although light emission and photovoltaic effects have been observed in organic materials long ago, the breakthrough came with the realization of thin film devices based on a double layer structure by Tang and van Slyke.[8,9] The basic working principle is that in both cases, an organic double layer is sandwiched between two contacts acting as anode and cathode (see Figure 1).

In both types of device, charge carrier transport in the thin films to the active zone (OLED) or away from it (OSC) is crucial. To make this transport as efficient as possible (i.e., with a low Ohmic loss), highly conductive transport layers are useful. Also, in both kinds of devices, carriers need to be either injected from inorganic contacts (OLED) or extracted to such contacts (OSC). Here, an efficient injection or extraction requires low energetic barriers or thin space charge layers, which can be tunneled through, or both.

It is important to emphasize that the breakthrough of the classical silicon technology came in the very moment the conduction type was no longer determined by impurities but could be controlled by doping. Unlike inorganic semiconductors, up to now, organic semiconductors are usually prepared in a nominally undoped form. However, controlled and stable doping is desirable for the realization and the efficiency of many organic-based devices. If one succeeds in shifting the Fermi level toward the transport states, this could reduce Ohmic losses, ease carrier injection from contacts, and increase the built-in potential of Schottky or p−n junctions.

Here, we review recent work on doping of organic semiconductors, both on fundamental principles and on device applications. In our own work, we have concentrated on evaporated layers, which were doped by coevaporation with a molecular dopant. The advantage of the molecular doping approach compared with the use of other substances, such as metals and gases, is the high stability that can be reached with molecular dopants. First, we will discuss the basic physics of doping, both for p-type[10−13] and for n-type[14−17] materials.

In both cases, the conductivity can be raised many orders of magnitude, well above the intrinsic conductivity of pure materials or the arbitrary conductivity caused by background impurities. While p-type doping is rather straightforward for most of the interesting materials (e.g., for the typical hole transport materials in OLEDs and organic solar cells), the molecular n-type doping has turned out to be a challenge due to the energetic position of the orbitals required for n-type doping.

We will also review some elementary model devices to understand basic device principles, particularly the first organic p−n homojunctions, which have recently been realized,[18] showing extremely large built-in voltages. However, these organic homojunctions also show the limits of the traditional semiconductor descriptions: The experimental results strongly deviate from the Shockley model, which is generally used for inorganic semiconductors.

Finally, we discuss the application of electrically doped organic layers in devices. In particular, we discuss organic light-emitting diodes where the introduction of doped transport layers leads to several improvements:

As a first important step, the Ohmic resistance of the transport layers is reduced, so that the transport layers are nearly field-free under operation (see Figure 2). In the top part, the band structure of a typical inorganic LED is schown schematically. In such a device, the emitter layer (center, with lower band gap) is sandwiched between two highly n- and p-doped transport layers. Due the high conductivity of these layers, the Ohmic losses are very small and the band edges are nearly flat since there is nearly no voltage drop. The operating voltage of the device is then close to the photon energy of the light emitted.

In organic light-emitting diodes with undoped transport layers, the carrier concentration is lower, leading to Ohmic losses and a higher field to drive the currents. In the extreme case, as shown in the bottom part of Figure 2, there is a large field needed across the device to drive the carriers, so that the operating voltage might be a multiple of the photon energy emitted.

While a low voltage drop may also be achieved by using very thin layers, there exist at least three major reasons to use somewhat thicker doped layers: Thick layers reduce the probability of short cuts, allow higher stability during the preparation process, and allow tuning of the optical microcavity in layered optoelectronic devices for an optimized field distribution.

Another very important fact is that doped transport layers lead to very narrow space charge regions at the contacts,

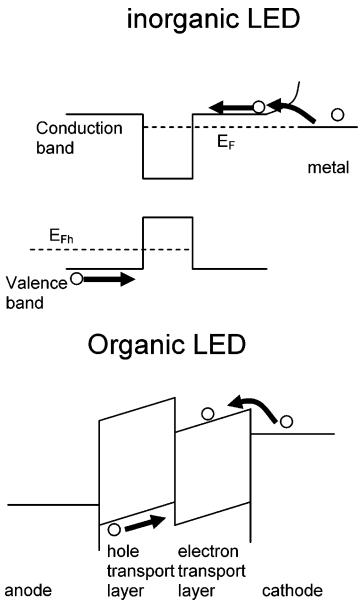


**Figure 2.** Typical inorganic LED (top), which is close to flat band conditions under operation (the injection at the contacts is by tunneling through thin space charge layers) and an undoped organic LED (bottom), in which due to the low charge carrier concentration, the energy levels are no longer flat but rather possess a slope needed to drive the lower number of injected carriers.

thin enough to allow the carriers to tunnel through, as schematically shown in the top part of Figure 2. Thus, it is possible to realize Ohmic contacts even when there are large energetic barriers between the transport layer and the contact. This is very advantageous, since in OLEDs with undoped transport layers, the optimization of the barriers requires additional processing effort, the use of rather unstable low work function contact materials, or both. OLEDs with doped transport layers are therefore much more flexible in terms of contact materials choice. This is particular advantageous for top-emitting or inverted OLEDs.

A second class of devices where doping is very advantageous is organic solar cells. There are a number of issues where doped layers can improve these devices:

- Doped window layers with nearly arbitrary thickness can be used to optimize the optical properties of the devices, that is, locate the maximum optical field near the absorber layers.
- Doping can help to achieve Ohmic contacts, which is even more essential in solar cells, which operate at very low voltages, where any voltage drop considerably reduces the performance.
- Finally, doping plays a crucial role in achieving efficient charge recombination contacts for stacked cell structures.

We will discuss experiments where these advantages have been proven in organic solar cell devices.

To conclude the introductory section, we now list the key materials discussed in the review (see Figure 3).

## 2. Doping Fundamentals

The basic principles of doping in organic semiconductors are similar to those in inorganic materials: Mobile carriers are generated by electron donors or acceptors. In organics, one has to add constituents, which either donate electrons to the lowest unoccupied orbital (LUMO) states (n-type doping) or remove electrons from the highest occupied orbital (HOMO) states to generate holes (p-type doping) (Figure 4). However, there are a number of differences between organics and classical semiconductors, which have to be taken into account when a detailed understanding is desired:

- The transport mechanism in organics is usually hopping, in contrast to band transport in classical semiconductors.
- The correlation energies in organics are much higher; for example, the exciton binding energy is on the order of 0.2−0.5 eV[19] compared with 4 meV in GaAs.[20]
- Polaronic effects are important in organic materials.

It was previously reported that high conductivities can be achieved when organic dyes with a weak donor character like the phthalocyanines are exposed to strongly oxidizing gases, such as iodine or bromine.[21] However, this technique is not suitable to prepare thermally stable bipolar devices like p−n or p−i−n junctions, since such small dopants can easily diffuse in the layers. Similar considerations hold for doping by other small atoms like lithium, cesium, or strontium[22,23] or small molecules like Lewis acids.[24]

As an example for the doping effect, we refer to Figure 5, where Parthasarathy and co-workers showed by ultraviolet photoemission spectroscopy (UPS) how the Fermi level in an organic semiconductor, in this case the well-known electron transporter bathocuproine (BCP), shifts upward upon doping with lithium. The lithium ions fill gap states in the BCP band gap.

A better approach toward electrical doping for stable devices is to use larger aromatic molecules, which are strong $\pi$-electron donors or acceptors. Several results on molecular doping have been reported in literature in the last decades. For instance, phthalocyanines have been doped by adding organic acceptor molecules like orthochloranil,[25] tetracyanoquinodimethane (TCNQ), or dicyano-dichloroquinone (DDQ).[26,27] Covalently bound stacked phthalocyanines[28] and oligothiophenes[29] have been doped by DDQ.

However, until recently systematic investigations of the influence of doping on fundamental semiconductor parameters like the Fermi level or the carrier density have still been rare. A proper thermodynamic description of the doping process is still a challenge. Apart from that, only a few attempts have been described in the literature to apply molecularly doped dye layers in semiconductor devices.[26,29]

In our group, we have systematically studied the physics of molecular doping of organics for several years.[10,13,14,30] In particular, we have successfully applied electrically doped transport layers to both OLEDs[11,31−34] and solar cells.[35,36] In the following, we will discuss the approach of doping by coevaporation of dopants with the organic matrix. We first discuss p-type doping, where we have performed extensive investigations with both polycrystalline and amorphous matrix materials, and then some selected results on n-type doping, which is challenging since it is difficult to find suitable stable molecules that can deliver an electron at an energy that is high enough to reach the LUMO of typical organic semiconductors.

### 2.1. p-Type Doping

#### 2.1.1. Fundamentals

Phthalocyanines are well suited as as model systems for p-type doping since they are known as a stable organic semiconductors and have a comparatively high lying HOMO; it

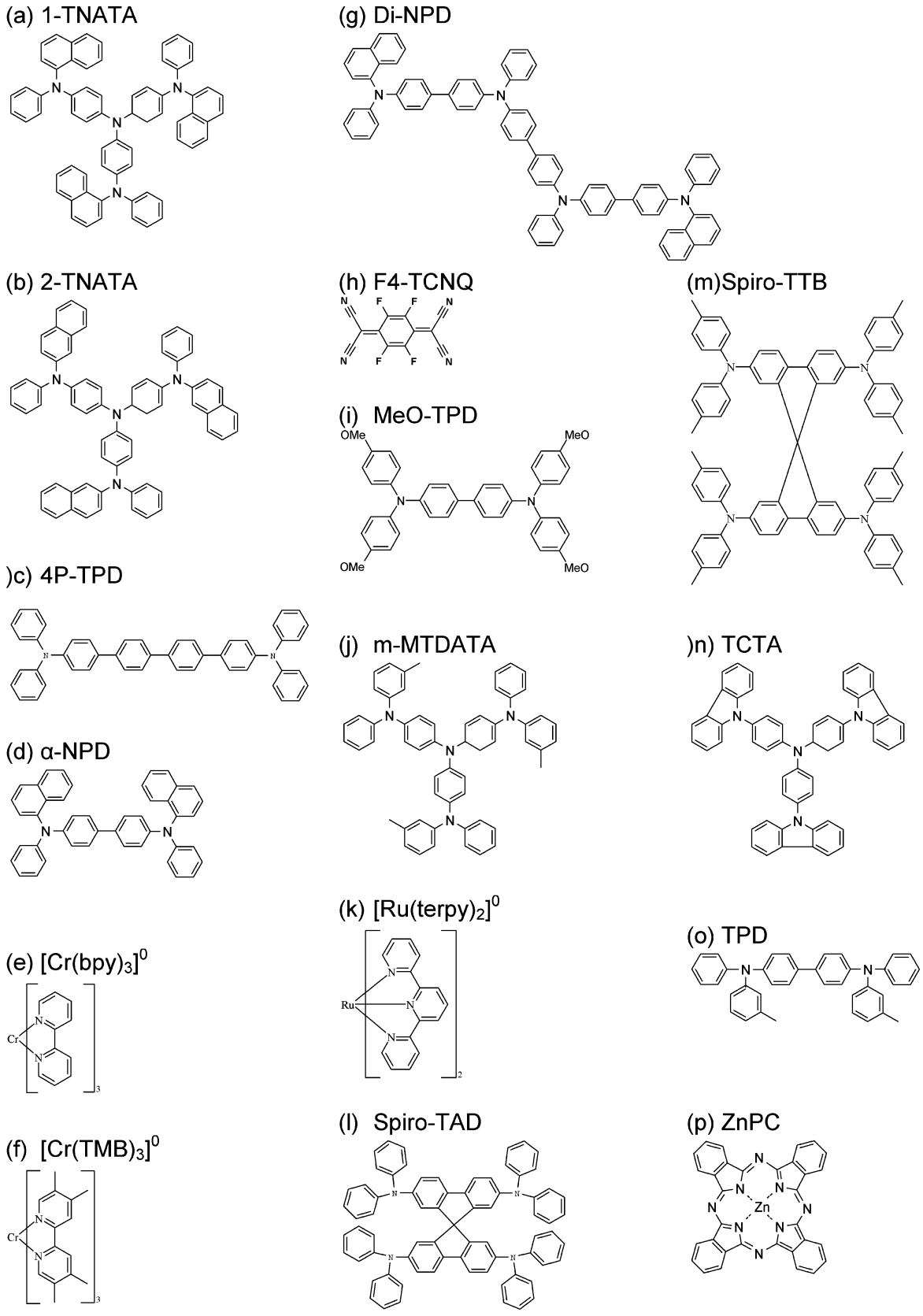


**Figure 3.** Key materials used in this paper: (a) 1-TNATA, 4,4′,4″-tris(1-naphthylphenylamino) triphenylamine; (b) 2-TNATA, 4,4′,4″-tris(2-naphthylphenylamino) triphenylamine; (c) 4P-TPD, 4,4′-bis-(*N*,*N*-diphenylamino)-quaterphenyl; (d) α-NPD, *N*,*N*′-di(naphthalen-2-yl)-*N*,*N*′-diphenyl-benzidine; (e) $[Cr(bpy)_3]^0$ (bpy = 2,2′-bipyridyl); (f) $[Cr(TMB)_3]^0$ (TMB = tetramethylbenzidine); (g) di-NPD, *N*,*N*′-diphenyl-*N*,*N*′-bis(4′-(*N*,*N*-bis(naphth-1-yl)-amino)-biphenyl-4-yl)-benzidine; (h) $F_4$-TCNQ, 2,3,5,6-tetrafluoro-7,7,8,8-tetracyanoquinodimethane; (i) MeO-TPD, *N*,*N*,*N*′,*N*′-tetrakis(4-methoxyphenyl)-benzidine; (j) *m*-MTDATA, 4,4′,4″-tris(3-methylphenylphenylamino) triphenylamine; (k) $[Ru(terpy)_2]^0$; (l) spiro-TAD, 2,2′,7,7′-tetrakis(*N*,*N*-diphenylamino)-9,9′-spirobifluorene; (m) spiro-TTB, 2,2′,7,7′-tetrakis(*N*,*N*′-di-*p*-methylphenylamino)-9,9′-spirobifluorene; (n) TCTA, 4,4′,4″-tris(*N*-carbazolyl)triphenylamine; (o) TPD, 4,4′-bis(3-methylphenylphenylamino) biphenyl; (p) ZnPC, zinc phthalocyanine.

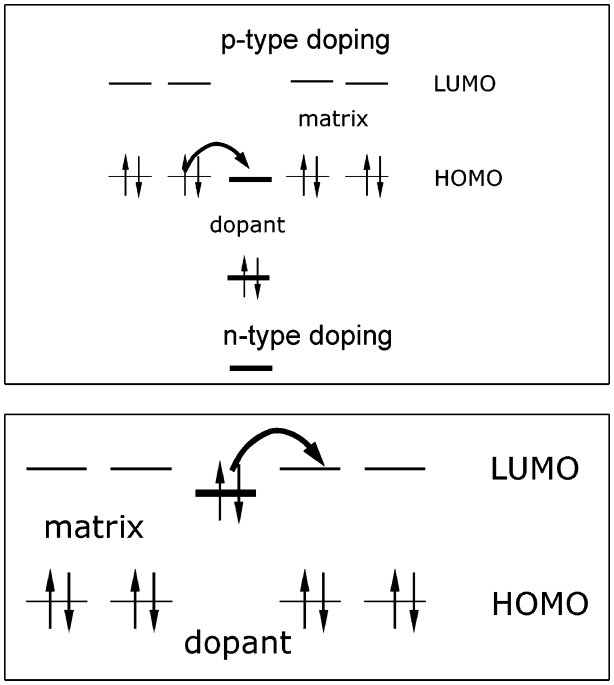


**Figure 4.** Doping mechanisms of molecular p-type (top) and n-type doping (bottom). In p-type doping the molecular dopant acts as acceptor and in n-type doping as donor. A sufficient energetic overlap of matrix and dopant energy levels is required for efficient doping.

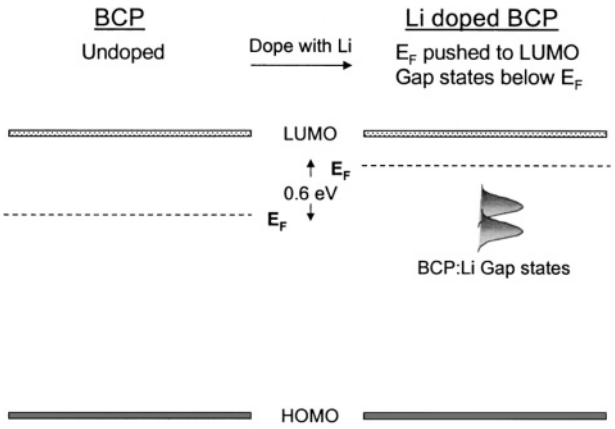


**Figure 5.** Proposed energy level scheme of undoped (left) and Li-doped (right) BCP thin films. The lowest unoccupied and highest occupied molecular orbitals are labeled LUMO and HOMO, respectively. Reused with permission from G. Parthasarathy, C. Shen, A. Kahn, and S. R. Forrest, *Journal of Applied Physics*, *89*, 4986 (2001). Copyright 2001, American Institute of Physics.

is thus rather easy to find acceptor-like molecules that lead to the generation of mobile holes in the organic matrix. In our study, we have used the strong acceptor $F_4$-TCNQ (see Figure 3) and have applied a number of characterization techniques to obtain a comprehensive understanding of the doping mechanisms, which shall be described in the following.

Figure 6 shows the conductivity of two different sample series of ZnPc doped with $F_4$-TCNQ as a function of the molecular doping ratio. The two most important points are that (i) the conductivity can be reproducibly controlled over more than 2 orders of magnitude by the doping ratio and (ii) the conductivity is many orders of magnitude higher than the background conductivity of nominally undoped ZnPc ($10^{-10}$ S/cm *in vacuo*).

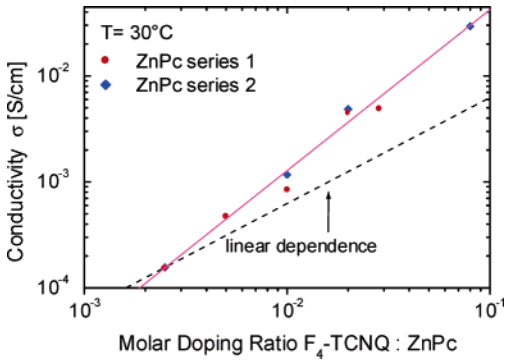


**Figure 6.** Conductivity of two different sample series of ZnPc doped with $F_4$-TCNQ as a function of molar doping ratio. For both samples, the conductivity is reproducibly increased by the doping. The dashed line symbolizes a linear relationship between doping ratio and conductivity. Obviously, the experimental data show a superlinear relationship.

The dashed line in Figure 6 shows that the conductivity rises much faster than linearly with the doping ratio, which is explained within a percolation model by a subtle interplay between charge carrier release by doping and a filling of a distribution of more or less localized states.[13] Details will be discussed below (see section 2.1.3).

We have performed measurements of the thermoelectric effect (Seebeck effect) in these materials[10,13] to better understand the energetics of the transport in these doped materials. The Seebeck effect is a useful and simple tool to measure the distance between the transport states (which we denote $E_\mu$ here) and the Fermi level, $E_F$. In a simple analysis, it turns out that the Seebeck coefficient, $S(T)$, as the relation between thermovoltage and temperature difference between the contacts can be expressed by[37]

$$S(T) = \frac{k_B}{e}\left[\left(\frac{E_F(T) - E_\mu}{k_B T}\right) + A\right] \quad (1)$$

where $A$ is a numerical factor that accounts for the kinetic energy of the charge carriers and can therefore be assumed to be negligible in low mobility organic materials.

Figure 7a shows the position of the Fermi level in ZnPc as a function of molecular doping concentration. It is obvious that the Fermi level shows the typical behavior of a doped semiconductor. With increasing doping, the Fermi level moves toward the transport states. These conclusions still hold in the framework of a more elaborate percolation model,[13] even if such a model implies that not only the Fermi level but also the dominant transport level $E_\mu$ slightly moves with temperature and doping level (see Figure 7).

It is also important to note that in this case, the Seebeck measurements are a proof that the conduction mechanism in our doped samples is not by hopping from dopant to dopant but indeed takes place in the valence states of the organic semiconducting matrix: if the carrier would move by hopping from dopant to dopant molecule, the Seebeck coefficient would be very small or even negative. Also, together with the conductivity results as a function of doping, the thermovoltage data make it highly unlikely that the conductivities result from the motion of ion impurities.

We have investigated p-type doping using $F_4$-TCNQ with a variety of hole transport matrices. It turned out that doping is a general effect that works for a large number of materials. For applications of doped layers in optoelectronic devices like OLEDs and solar cells, it is especially important that

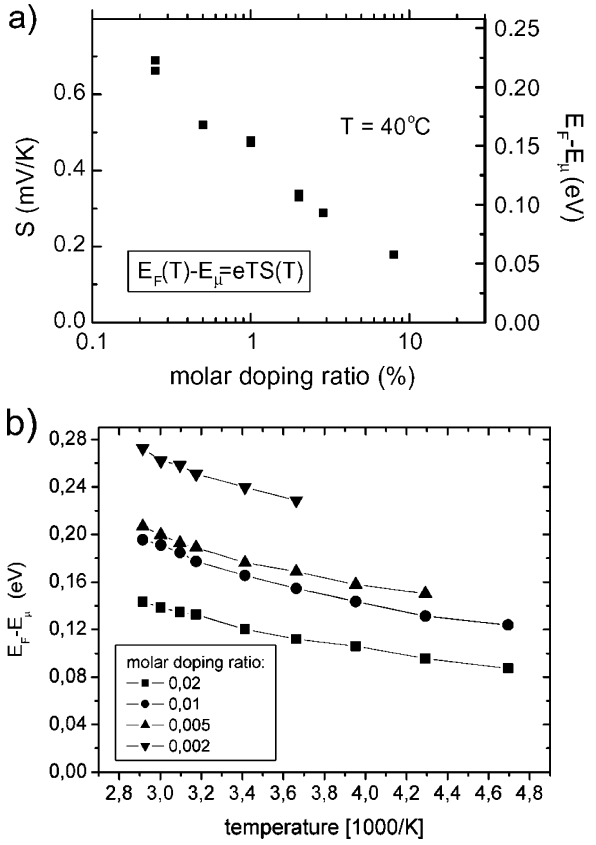


**Figure 7.** (a) Seebeck coefficient, *S* (left axis), and distance (right axis) between the Fermi energy level, $E_F$, and the dominant transport energy level, $E_\mu$, at 40 °C, calculated according to the equation given in the inset, for ZnPc layers doped with $F_4$-TCNQ as a function of the doping concentration. The Fermi level behaves in close agreement with inorganic semiconductors; that is, it moves toward the transport state with increasing doping concentration. Reprinted from ref 38, Copyright 2003, with permission from Elsevier. (b) Shift of Fermi level with temperature. For experimental details, see refs 10 and 38.

amorphous wide gap hole transport materials such as 4,4′,4″-tris-*N*,*N*-diphenyl-amino-triphenylamine (TDATA) can be doped as well.[39] The resulting conductivities for TDATA are on the order of $1 \times 10^{-7}$ to $1 \times 10^{-5}$ S/cm at a doping level of 2% $F_4$-TCNQ,[32] that is, much lower than that for the polycrystalline phthalocyanine as shown in Figure 6. The reason for the lower conductivity is the much lower mobility of the amorphous material; the carrier concentrations are comparable: for the highest doping concentrations (a few percent dopant), they are around $10^{20}$ $cm^{-3}$. It is important to note that in inorganic semiconductors, such doping levels would lead to metallic behavior due to the long-range coupling of the dopant atom. In organic materials, such high doping levels still lead to semiconducting properties due to the high density of states in the LUMO level and the weak coupling of the dopant energy levels.

Using infrared spectroscopy, it is possible to follow the charge transfer from the matrix molecules to the acceptor dopant.[13] The precise frequency of the stretching mode of the C−N triple bond in the cyano groups is sensitive to the degree of charge transfer from the organic matrix to the acceptor molecule and thus provides direct information on the degree of charge transfer, *Z*. The results for a number of materials are listed in Table 1. A complete charge transfer ($Z = 1$) is found for matrix materials like the phthalocyanines and TDATA derivatives. They have ionization energies around 5 eV, which is close to the electron affinity of $F_4$-TCNQ.[30,40] When TCNQ instead of $F_4$-TCNQ is used as a dopant, the degree of charge transfer is low even in ZnPc ($Z = 0.2$), and consequently, the conductivity at 2% doping is only in the order of $1 \times 10^{-6}$ S/cm for TCNQ instead of $1 \times 10^{-3}$ S/cm for $F_4$-TCNQ in ZnPc. It is thus obvious that only the enhancement of electron affinity by about 0.5 eV by fluorination of TCNQ was the crucial step to achieve an efficient molecular doping.[10]

On the other hand, we observe an only partial charge transfer for $F_4$-TCNQ in TPD ($Z = 0.64$) due to its higher ionization energy of around 5.4 eV.[41] Accordingly, the conductivity for a given doping ratio of 2 mol % is lower for TPD ($1 \times 10^{-7}$ S/cm) than for *m*-MTDATA ($3 \times 10^{-7}$ S/cm) even though the intrinsic hole mobility in *m*-MTDATA ($3 \times 10^{-5}$ $cm^2/(V\ s)$)[42] is more than 1 order of magnitude lower than that in TPD ($1 \times 10^{-3}$ $cm^2/(V\ s)$).[43] By attaching one electron-pushing methoxy group to each of the four outer benzene rings of TPD, its ionization energy can be reduced. This material, *N*,*N*,*N*′,*N*′-tetrakis(4-methoxyphenyl)-benzidine (MeO-TPD) seems to have similarly high hole mobility as TPD but a higher degree of charge transfer ($Z = 0.73$) and thus yields a high conductivity ($5 \times 10^{-6}$ S/cm at 2% doping) for the amorphous hole transport materials, which is well suitable for OLEDs and organic solar cells. When doped by 2% $F_4$-TCNQ, the hole mobility of MeO-TPD is $1 \times 10^{-4}$ $cm^2/(V\ s)$.[44]

Obviously, the conductivity drops very quickly if the charge-transfer ratio, *Z*, falls below unity. Here, it should be noted that *Z* is not a probability for a complete charge transfer but rather has to be understood in terms of mixing coefficients for an electron that occupies an orbital being a linear combination of the acceptor LUMO and the matrix HOMO.

To summarize, these results show that the doping effect is rather general provided that the energy alignment of the organic matrix and the dopant allows an efficient electron transfer.

### *2.1.2. Comparison of Amorphous and Polycrystalline Materials*

Morphology is a crucial parameter for the conductive properties of any solid. Organic semiconductors used in devices are typically prepared by vapor deposition in high vacuum or by spin-coating from solution and have a polycrystalline or amorphous morphology. As shown in the previous section, the doping process in polycrystalline dyes can largely be described by the standard description used for crystalline inorganic semiconductors.[14,30] Amorphous materials are in particular popular for OLEDs, mainly because they form smooth layers and do not degrade by crystallization (if the glass transition temperature is high enough). Also, amorphous materials are simpler model systems and allow, for example, the exclusion of effects caused by grain boundaries. It is thus very interesting to clarify how the doping process depends on the morphology of the organic layers.

In the following, we discuss our investigations of the semiconducting behavior of polycrystalline and amorphous vacuum-deposited layers.[13] We have used again zinc phthalocyanine (ZnPc) as a model matrix material and tetrafluoro-tetracyanoquinodimethane ($F_4$-TCNQ) as dopant because the doping process is quite efficient for these two materials, as discussed above. Polycrystalline and amorphous ZnPc films

**Table 1. p-Doping of Various Hole Transport Materials by TCNQ Derivatives**[a]

| matrix/dopant | ZnPc/$F_4$-TCNQ | ZnPc/TCNQ | *m*-MTDATA/$F_4$-TCNQ | TPD/$F_4$-TCNQ | MeO-TPD/$F_4$-TCNQ |
|---|---|---|---|---|---|
| $I_s$ (eV) | 5.1[12] | 5.1 | 5.1[45] | 5.4[41] | |
| $Z$ | 1 | 0.2 | 1 | 0.64 | 0.74 |
| $\sigma$ (S/cm) | $1 \times 10^{-3}$ | $1 \times 10^{-6}$ | $3 \times 10^{-7}$ | $1 \times 10^{-7}$ | $1 \times 10^{-5}$ |

[a] The table shows the solid-state ionization energy, $I_s$, of the matrix materials, the degree of charge transfer from the matrix to the dopant, derived from the position of the $b_{1u}\nu_{18}$ mode of the TCNQ derivatives, and the conductivity at a doping level of 2 mol % for a series of matrix/dopant combinations.

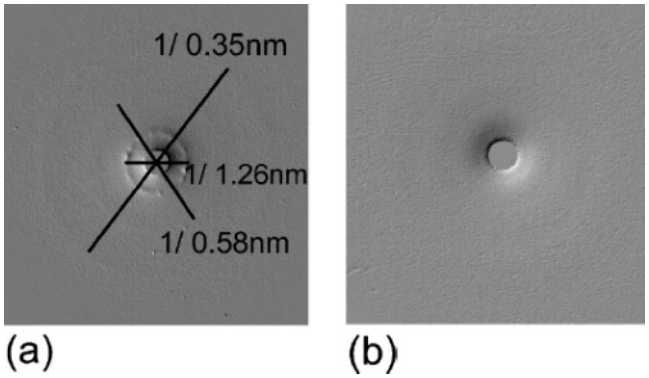


**Figure 8.** Differentiated electron diffraction images of two ZnPc layers (50 nm thick) on a carbon foil. The layers were prepared at a substrate temperature of (a) 25 and (b) −150 °C. The numbers in panel a denote the distance in nanometers of the corresponding crystallographic planes. Note that we display differentiated images since the original diffraction images are difficult to analyze because of the very low intensity. Reprinted Figure 2 with permission from Maennig, B.; Pfeiffer, M.; Nollau, A.; Zhou, X.; Leo, K.; Simon, P. *Phys. Rev. B, 64*, 195208, 2001 (http://link.aps.org/abstract/PRB/v64/e195208). Copyright 2001 by the American Physical Society.

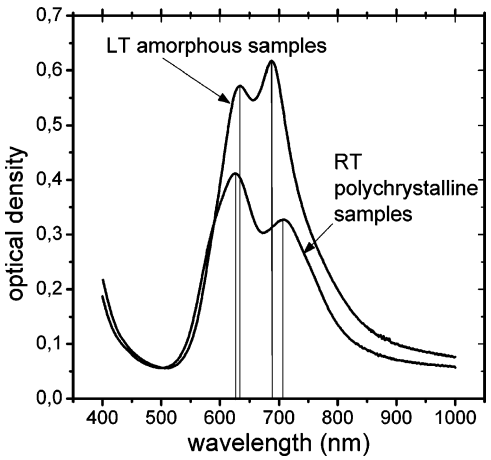


**Figure 9.** Absorption spectra of ZnPc layers (50 nm thick). The RT polycrystalline sample was prepared at 25 °C substrate temperature and the LT amorphous sample at −150 °C substrate temperature. Reprinted Figure 3 with permission from Maennig, B.; Pfeiffer, M.; Nollau, A.; Zhou, X.; Leo, K.; Simon, P. *Phys. Rev. B, 64*, 195208, 2001 (http://link.aps.org/abstract/PRB/v64/e195208). Copyright 2001 by the American Physical Society.

were prepared by variation of the substrate temperature during layer growth. The films were electrically characterized by temperature-dependent measurements of the conductivity, the thermopower (Seebeck effect), and the field-effect mobility. From the Seebeck coefficient, we can calculate the hole density, $p$. In combination with the measured conductivity, $\sigma$, we obtain the hole mobility, $\mu_h$, assuming $\sigma = ep\mu_h$. The field-effect measurements allow direct determination of the hole mobility and comparison to the calculated values. The results for $\mu_h$ obtained from the different measurements are largely consistent. We will then show that a comprehensive description requires a percolation model both for polycrystalline and for amorphous materials.

To vary the morphology of the films, we used the well-known substrate temperature dependence.[46] A polycrystalline film (α-phase) grew when the substrate was held at room temperature (25 °C, RT samples), and an almost amorphous film grew when the substrate was cooled to below −100 °C (here −150 °C, LT samples). This behavior is observed for different substrate materials like silica, KBr, and carbon foil. Details of the sample preparation and the conductivity and Seebeck measurements are described in ref 35. The field-effect mobility was determined with a thin film transistor arrangement using either a silicon oxide gate layer thermally grown on a highly doped n-type silicon wafer or a polymeric gate insulator on indium tin oxide (ITO).

First, the structural characterization of the samples was done by X-ray diffraction. Differentiated diffraction patterns of the RT and LT samples are shown in Figure 8.

The RT sample shows Debye−Scherrer rings and some discrete diffraction spots due to the polycrystalline morphology of the phthalocyanine (Figure 8a). The rings correspond to the (2 0 0), (4 0 −2), and (3 1 −2) lattice planes, indicating the low-temperature α-phase crystalline modification of ZnPc. The crystalline domains had an average size of about 20−30 nm. In the diffraction pattern of the LT sample, the Debye−Scherrer rings are missing, and only amorphous halos corresponding to 1.26, 5.80, and 0.35 nm were observed. The amorphous phase was stable up to a temperature of 50 °C. The absorption spectra of the RT and LT samples are shown in Figure 9.

The absorption spectrum of ZnPc in solution shows only one peak at 679 nm in the depicted energy range.[47] In the solid state, this electronic excitation splits up in two parts because of molecular interactions.[48] The positions of the peaks are 625 and 710 nm for the polycrystalline sample and 635 and 688 nm for the amorphous sample, respectively. The separation of the peaks is smaller for the amorphous than for the polycrystalline phase, which is a strong hint at a lower interaction of the molecules of the LT sample, corresponding well with the lower degree of order.

We now discuss the results of the conductivity and Seebeck studies. The conductivity of undoped ZnPc is below $10^{-10}$ S/cm.[13] In Figure 10a, the conductivity is plotted versus the reciprocal temperature for the doped samples grown at different substrate temperature. The molar dopant concentration is 1% in both samples. At room temperature, the conductivity is 6 orders of magnitude higher than that in the undoped samples. The conductivity shows a thermally activated behavior in the measured temperature range. For the polycrystalline sample, the activation energy is $E_{act} = 0.18$ eV. In comparison, the activation energy is $E_{act} = 0.24$ eV for a molar dopant concentration of 0.2%; that is the activation energy slightly decreases with increasing dopant

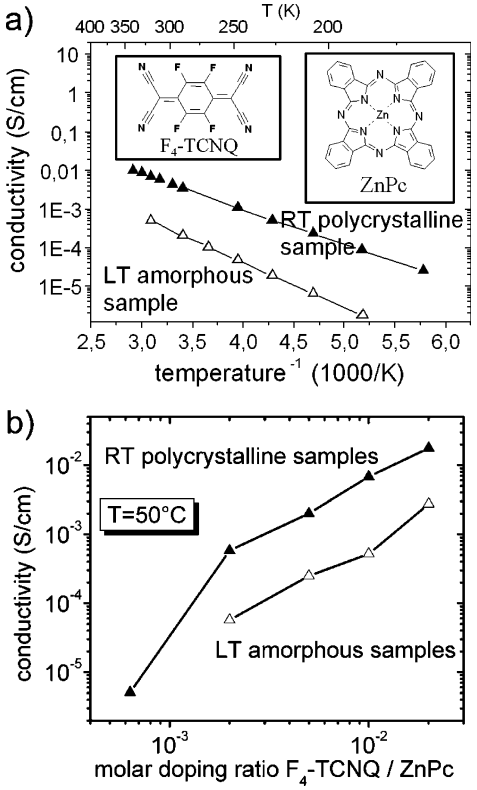


**Figure 10.** Conductivity of ZnPc layers (30 nm thick) doped with 1% $F_4$-TCNQ: (a) Arrhenius plot for a RT polycrystalline and LT amorphous samples; (b) conductivity vs molar doping ratio for the RT polycrystalline and LT amorphous samples. The conductivity of the LT amorphous samples is about 1 order of magnitude lower compared with that of the RT samples. Reprinted Figure 4 with permission from Maennig, B.; Pfeiffer, M.; Nollau, A.; Zhou, X.; Leo, K.; Simon, P. *Phys. Rev. B*, *64*, 195208, 2001 (http://link.aps.org/abstract/PRB/v64/e195208). Copyright 2001 by the American Physical Society.

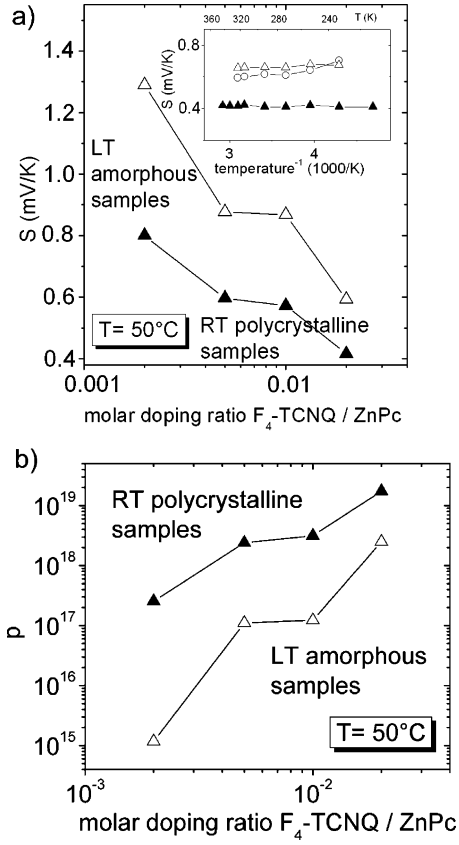


**Figure 11.** (a) Seebeck coefficient, *S*, vs molar doping ratio for ZnPc layers (30 nm thick) doped with $F_4$-TCNQ. The values of the LT amorphous samples are about 0.2−0.3 mV/K higher than those for the RT polycrystalline samples. The inset shows the Seebeck coefficient vs temperature for a RT and LT sample with a molar doping ratio of 2% and a 400 nm thick LT sample with a molar doping ratio of 1.2%. Here, the slight increase of *S* with 1/*T* for the thin LT sample (○) is due to problems of the measurement because of the low current in the thin film. For the thicker layer (△), *S* stays constant. (b) Hole density vs molar doping ratio. Reprinted Figure 5 with permission from Maennig, B.; Pfeiffer, M.; Nollau, A.; Zhou, X.; Leo, K.; Simon, P. *Phys. Rev. B*, *64*, 195208, 2001 (http://link.aps.org/abstract/PRB/v64/e195208). Copyright 2001 by the American Physical Society.

concentration. For the amorphous sample, the activation energy is 0.23 eV. Again, the activation energy is higher for a molar dopant concentration of 0.2% (0.29 eV).

Figure 10b shows the conductivity vs the molar doping ratio. Surprisingly, the conductivity increases strongly superlinearly with the concentration of $F_4$-TCNQ for both types of samples. Generally, the conductivity of the amorphous samples is about 1 order of magnitude lower than that for the polycrystalline samples.

To further characterize the samples, thermovoltage measurements were performed to determine the Seebeck coefficient, $S(T)$. For a first analysis, the simplest model of only one relevant transport level can be used. It will be later seen that this model cannot completely explain the measurements. As discussed above, for unipolar charge carrier transport at one transport level $E_\mu$, $S$ reveals the transport type (n or p) from its sign and the energetic difference between the Fermi level, $E_F$, and the relevant transport level, $E_\mu$, from its value (see eq 1)). It is important to mention that this holds regardless of the details of the transport mechanism. For instance, it applies to band transport (as long as the bandwidth is small compared with $kT$) and to hopping transport.[37] All Seebeck coefficients $S$ measured for ZnPc/$F_4$-TCNQ are positive (see Figure 11a).

The Seebeck coefficient $S$ of the LT amorphous samples is about 0.2−0.3 mV/K higher than that for the RT samples. For all samples, $S$ is basically temperature independent (see inset of Figure 11a).

For the further evaluation of the Seebeck measurements, it was assumed that the effective density of states, $N_\mu$, at the transport level $E_\mu$ is comparable to the density of molecules, $N_m$. This is equivalent to the assumption that every molecule contributes one transport state. For α-ZnPc, the density of molecules is about $N_m = 1.7 \times 10^{21}$ cm$^{-3}$. The density of holes, $p$, in the transport state is then given by

$$p = N_\mu \exp\left(-\frac{E_F(T) - E_\mu}{kT}\right) = N_\mu \exp\left(-\frac{eS}{k}\right) \quad (2)$$

with $k$ as the Boltzmann constant. The Maxwell−Boltzmann approximation can be used since the distance between Fermi level and transport states is much larger than the thermal energy. However, we already note here that the effective density of states, $N_\mu$, is not known in our materials and that for a comprehensive understanding of the measurements, one has to go beyond the assumption of only one relevant transport level, which is discussed in the percolation model below. Therefore, the values of the hole density determined this way from the Seebeck coefficient are an upper limit because the effective density of states will always be lower than the density of molecules.

The hole density obtained ranges from $10^{15}$ to $10^{19}$ $cm^{-3}$ (Figure 11b). They show the same characteristic behavior upon doping as the conductivity: the hole density increases strongly superlinearly with the concentration of the dopant, and the values for the LT amorphous samples are about 1 order of magnitude lower than those for the RT samples.

The combination of the Seebeck measurements with the conductivity results allows then deduction of the hole mobility by application of the equation

$$\sigma = ep\mu_h \tag{3}$$

The resulting hole mobility is independent of the doping density and has the same value of about $5 \times 10^{-3}$ $cm^2/(V\ s)$ at room temperature for both the polycrystalline and amorphous samples.

Altogether, we obtain qualitatively the same behavior for the polycrystalline and the amorphous samples upon doping. It is therefore very unlikely that the superlinear increase of the conductivity with doping is caused by structural effects like high conductance paths or an accumulation of the dopant molecules at grain boundaries: such structural effects are not expected in an amorphous phase. Accordingly, they should be much more pronounced in the polycrystalline RT samples than in the LT samples, which are largely amorphous.

The (free) hole density appears to be temperature independent because the Seebeck coefficient is temperature independent. To explain this temperature behavior in the standard semiconductor statistics, we would have to assume that the acceptors form shallow states, that is, all acceptors are ionized, and that there are only shallow traps (or no traps).[49] Otherwise, $p$ would increase with temperature. However, for the shallow acceptor case, hole density and conductivity should increase linearly with the doping density, which is in clear contradiction to our measurements. To understand this phenomenon, we now consider the evolution of the field-effect mobility upon doping.

It is common to use the basic equations of the silicon-based metal−insulator−semiconductor field-effect transistor (MISFET) to describe the organic-based thin film transistor (TFT) although the device structure of the organic TFTs differs from that of the conventional MISFETs.[50,51] The drain current, $I_D$, is then given by

$$I_D = \frac{W}{L}\mu_{FE}C_i\left[(V_G - V_{th})V_D - \frac{1}{2}{V_D}^2\right] \tag{4}$$

for $V_D < V_G - V_{th}$. Here, $W$ is the width of the source and drain electrodes, $L$ is the channel length, $\mu_{FE}$ is the field-effect mobility, $C_i$ is the capacitance per unit area of the insulating layer, $V_G$ and $V_D$ are the applied gate and drain voltage, and $V_{th}$ is the threshold voltage. The field-effect mobility is an effective mobility, which is related to the mobility, $\mu_h$, of the holes by

$$\mu_{FE} = \mu_h \frac{p}{p + p_t} \tag{5}$$

in the model of only one relevant transport level for a p-type semiconductor. Here, $p$ is the free hole density, $p_t$ is the density of trapped holes, and $\mu_h$ is the mobility of free holes.

The transfer characteristics of the thin film transistor measured at 67 °C are given in Figure 12a for a polycrystalline sample. The drain current changes between 700 and 950 nA by variation of the gate voltage between +10 and −10 V. The output characteristics are completely in the linear regime. The drain current cannot be reduced to zero because the density of the induced charge carriers is small compared with the charge density due to doping. Additionally, the depletion width (approximately 8 nm) is smaller than the thickness of the ZnPc layer so that the layer cannot be completely depleted.

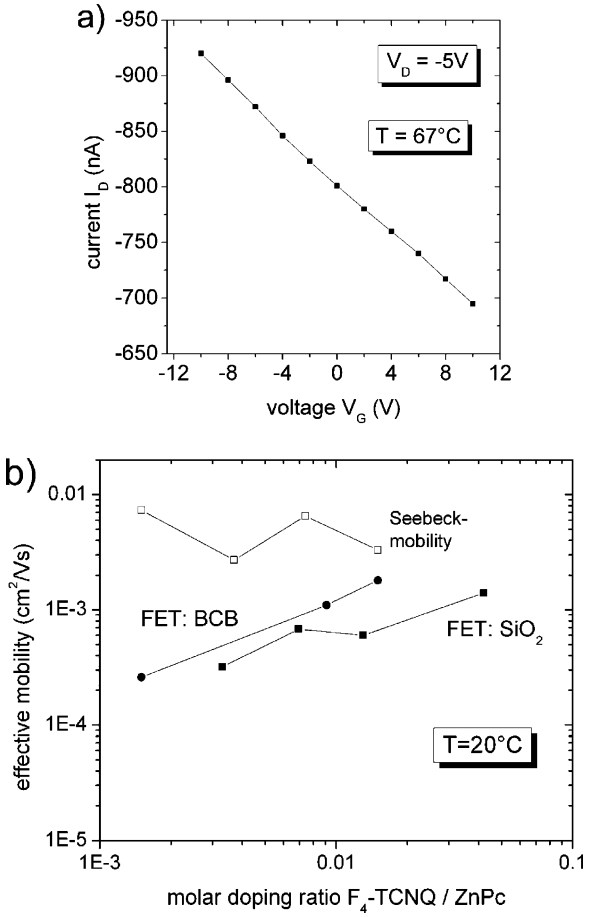


**Figure 12.** (a) Transfer characteristics of a thin film transistor (type I) using a 30 nm polycrystalline ZnPc layer as active semiconductor (doping ratio 0.7%) and (b) field-effect mobility and Seebeck mobility vs molar doping ratio. The field-effect mobility increases with increasing dopant concentration and the Seebeck mobility seems to be independent of the doping concentration (within experimental error). Reprinted Figure 6 with permission from Maennig, B.; Pfeiffer, M.; Nollau, A.; Zhou, X.; Leo, K.; Simon, P. *Phys. Rev. B*, *64*, 195208, 2001 (http://link.aps.org/abstract/PRB/v64/e195208). Copyright 2001 by the American Physical Society.

Since the threshold voltage, $V_{th}$, is unknown, the field-effect mobility can be best calculated from the slope of the curves in the transfer characteristics:

$$\frac{dI_D}{dV_G} = \frac{W}{L}\mu_{FE}C_iV_D \tag{6}$$

For a drain voltage of −5 V, we obtain $\mu_{FE} = 7 \times 10^{-4}$ $cm^{-3}$ at 20 °C, which is a typical value for ZnPc and other polycrystalline organic materials.[52] The values of the field-effect mobility for the polycrystalline samples determined for thin film transistors of type I and type II are given in Figure 12b. No FET data could be obtained for the LT samples. For the thin film transistors of type I and type II,

the values are in the same range with a deviation of 50%, which is probably due to the different growth behavior of ZnPc on different substrates, different interface trap densities, or both. The field-effect mobility increases with increasing dopant concentration, which is explained as follows: The measured field-effect mobility is the mobility of the charge carriers additionally induced by the gate voltage. With increasing doping concentration, the traps in the material become gradually filled. As a result, the additionally induced charge carriers have a lower probability to be trapped. The effective mobility thus increases according to eq 5 because the ratio of $p$ and $p_t$ increases.

The field-effect mobility shows a thermally activated behavior with the same activation energy as the conductivity.[13] This is again a strong hint for shallow acceptor states, because it implies that the total hole density, $p + p_t = \sigma/(\mu_{FE}e)$, is temperature independent. For comparison, the mobility derived from the combination of the Seebeck and conductivity measurements, which will be denoted as Seebeck mobility, $\mu_{SE}$, in the following, is also given in Figure 12b. The Seebeck mobility seems to be independent of the doping concentration (within the experimental error) and is about a factor of 5 higher than the field-effect mobility at high doping ratios. The Seebeck mobility and the field-effect mobility are thus in the same order of magnitude. The assumption that the effective hole density, $N_\mu$, is equal to the density of molecules appears therefore realistic. The Seebeck mobility is equal to the mobility of free holes (eq 5) and therefore must be higher than the field-effect mobility. A comparison of Seebeck and field-effect mobility allows an estimate of the hole trap density $p_t$: from eq 5, we can estimate $p_t = (1-3) \times 10^{19}$ cm$^{-3}$ for high doping concentrations.

### 2.1.3. Explanation of Transport Results with a Percolation Model

The previous section has given a qualitative explanation for the superlinear behavior of the conductivity as a function of doping: With increasing doping density, the traps (or lower lying low mobility states) are filled and the effective mobility rises. Together with the shallow and thus fully ionized acceptor states, this causes a superlinear increase.

To explain our findings more comprehensively, we have developed a more detailed percolation model.[13] Figure 13 shows the measured conductivity of the RT samples together with the theoretical curves. In the model, three fit paramters are used: $\sigma_0$ is a constant prefactor of the conductivity, $T_0$ describes the width of the exponential distribution of the localized transport states, and $\alpha$ is the Bohr radius of the localized wavefunctions, which are assumed to be s-like.

In agreement with the results given in ref 53 for pentacene and poly(thienylene vinylene), the main difference between the materials appears not in $\sigma_0$ nor in the width of the exponential distribution $T_0$, but in the fit parameter $\alpha$ (Table 2). Its value increases from 0.37 Å$^{-1}$ for polycrystalline ZnPc up to 1.39 Å$^{-1}$ for TDATA. The activation energy of the conductivity also increases in this order. Because the value of $\alpha^{-1}$ is <3 Å, that is, smaller than the size of one molecule, one cannot interpret $\alpha^{-1}$ simply as the Bohr radius but as an overlap parameter determining the tunneling process.[53] Note that the conductivity data of one material at different doping levels can be modeled with the same values of $T_0$ and $\alpha$. This is a strong indication that the molecular doping does not lead to changes in the layer structure or in the energy

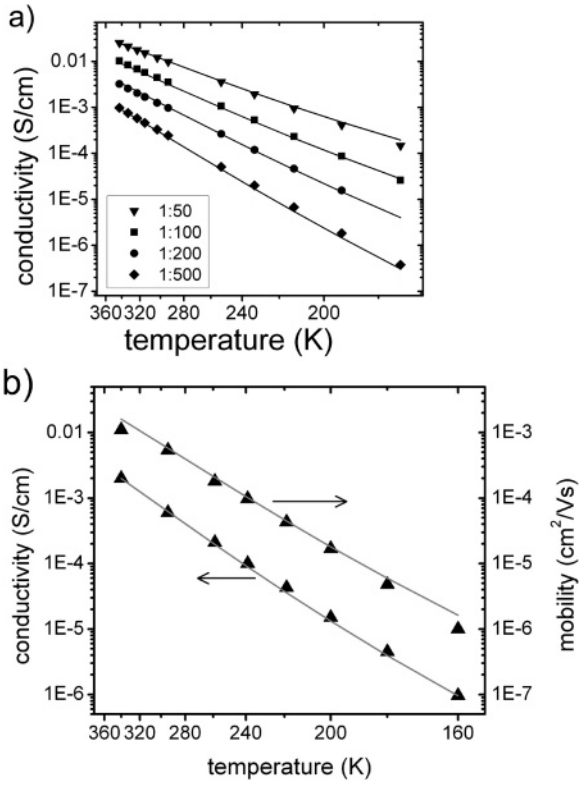


**Figure 13.** (a) Conductivity of the RT polycrystalline samples vs temperature. The solid lines are the fit curves. (b) Conductivity and field-effect mobility of a RT polycrystalline sample (type I, doping ratio 0.7%) vs temperature. Reprinted Figure 7 with permission from Maennig, B.; Pfeiffer, M.; Nollau, A.; Zhou, X.; Leo, K.; Simon, P. *Phys. Rev. B, 64*, 195208, 2001 (http://link.aps.org/abstract/PRB/v64/e195208). Copyright 2001 by the American Physical Society.

distribution, that is, the density of states, at least for the doping ratios considered here. We investigated the influence of doping on the morphology for the system ZnPc doped with $F_4$-TCNQ by electron diffraction. Here, for doping levels up to 5%, no indication for a new crystallographic phase appears.[49]

Among the given materials, ZnPc displays the best doping efficiencies. We can explain this in the following way: The higher value of $\alpha^{-1}$ is due to a larger overlap of the wavefunctions. Therefore, the tunneling process is easier and the conductivity higher. In the amorphous samples, the molecules are less ordered, which results in a smaller overlap of the wavefunctions compared with the polycrystalline samples. For the different materials, the activation energy of the conductivity increases with decreasing $\alpha^{-1}$. The reason for this is that for a lower value of $\alpha^{-1}$, tunneling over wide distances is rather improbable, so the charge transport can only take place in an energetic region where the density of states is high, that is, far away from $E_F$. Accordingly, the activation energy of the critical hop is high. For each material, the activation energy of the conductivity decreases with increasing dopant concentration, which is to be expected because doping shifts $E_F$ closer to an energetic region with high density of states.

In the meantime, Schmechel has shown that the experimental values as mentioned above can also be described quantitatively by a semiconductor model.[54,55] Here, the description is based on the Miller−Abrahams model for hopping transport in a disordered material and utilizes the so-called transport energy concept.

**Table 2. Conductivity at 40 °C, Activation Energy of the Conductivity (Dopant Density 1% for Both), and Fit Parameters $\sigma_0$, $T_0$, and α for Polycrystalline ZnPc, Amorphous ZnPc (Both 30 nm Thick Layers), VOPc (Vanadyl Phthalocyanine, Polycrystalline, 500 nm), and TDATA (4,4′,4″-Tris(*N*,*N*-diphenylamino)-triphenylamine, Amorphous, 500 nm)[a]**

| material | $\sigma$ (S/cm) | $E_{act}$ (eV) | $\sigma_0$ ($10^5$ S/m) | $T_0$ (K) | α (Å$^{-1}$) |
|---|---|---|---|---|---|
| ZnPc (polycrystalline, RT) | $5.8 \times 10^{-3}$ | 0.18 | $12 \pm 3$ | $485 \pm 15$ | $0.37 \pm 0.01$ |
| ZnPc (amorphous, LT) | $4 \times 10^{-4}$ | 0.23 | $11 \pm 6$ | $455 \pm 15$ | $0.64 \pm 0.02$ |
| VOPc (polycrystalline) | $2.3 \times 10^{-5}$ | 0.32 | $6 \pm 1$ | $485 \pm 15$ | $1.00 \pm 0.04$ |
| TDATA (amorphous) | $5.9 \times 10^{-7}$ | 0.34 | $3 \pm 1$ | $515 \pm 15$ | $1.39 \pm 0.03$ |

[a] Here, $\sigma_0$ is a prefactor, $T_0$ describes the width of the exponential distribution of localized states, and α is an overlap parameter determining the tunneling process. Reprinted Table 1 with permission from Maennig, B.; Pfeiffer, M.; Nollau, A.; Zhou, X.; Leo, K.; Simon, P. *Phys. Rev. B, 64,* 195208, 2001 (http://link.aps.org/abstract/PRB/v64/e195208). Copyright 2001 by the American Physical Society.

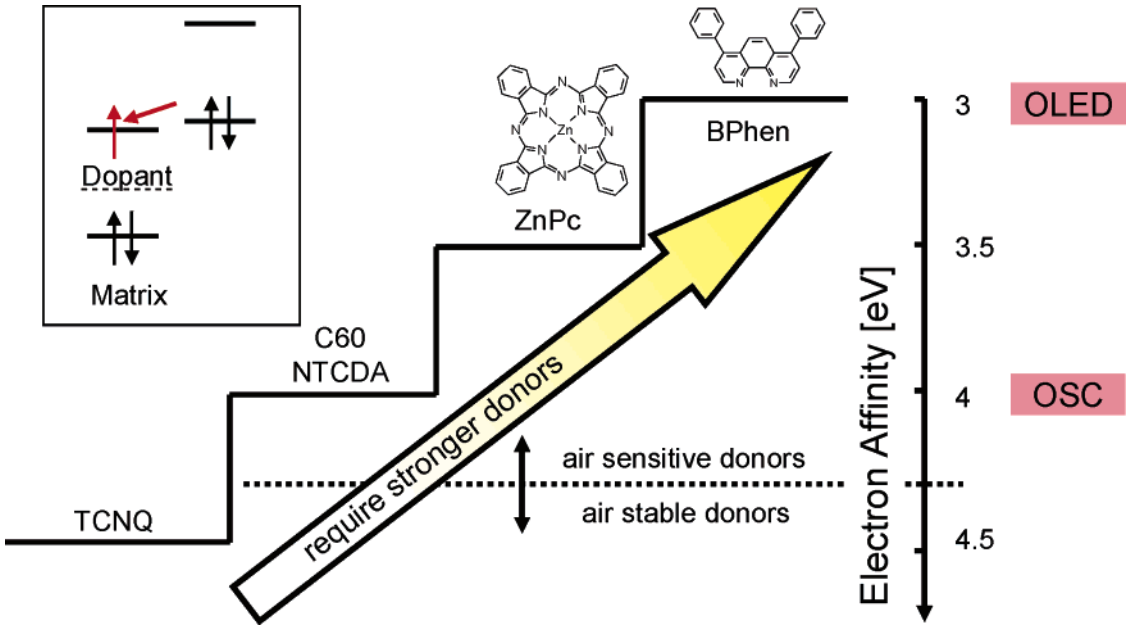


**Figure 14.** n-Type doping of molecular materials relevant for OLED and organic solar cells requires different electron affinities. While organic solar cells may be doped with donors having a HOMO around 4.0 eV, OLEDs require stronger donors with a HOMO at about 3.0 eV. Such materials are increasingly unstable in air, which requires handling under protective atmosphere only. The "staircase" shows typical host materials for OLEDs and OSCs.

## 2.2. n-Type Doping

In contrast to p-type doping, n-type molecular doping is intrinsically more difficult due to the following fact (see Figure 14): For efficient doping, the HOMO level of the dopant must be energetically above the LUMO level of the matrix material (inset), which makes such materials unstable against oxygen. With increasing LUMO energy, the difficulty to find suitable materials is increased.

For materials with low-lying LUMO level, that is, high electron affinity, we have achieved reasonable conductivities using the dopant bis(ethylenedithio)tetrathiafulvalene (BEDT-TTF).[14] For solar cells, where the electron transporters have such a low-lying LUMO, this dopant could work. However, it is not applicable for typical OLED electron-transporting materials, which have a rather low electron affinity of around 3.0 eV. For efficient doping by an organic material, this would require strong donors with a HOMO in this range, which consequently causes rapid oxidation by air.

In the following, we discuss three different approaches to obtain efficient n-type doping, even for materials with a comparatively high-lying LUMO:

- A first approach is the use of alkali metals, which has frequently been used to improve electron injection in OLEDs.
- A second approach is the search for new molecular compounds that have extremely high-lying HOMOs but are thus not air-stable.
- Finally, we discuss a novel approach with cationic salts, which circumvents the use of materials that are not air-stable.

### 2.2.1. n-Type Doping Using Alkali Metals

In the 1970s, alkali metals have been reported for n-doping of organics,[56] followed by several experimental[57] and theoretical studies. The first reports of a Li doping for OLED cathode interfaces date back to the 1990s.[58,59] For this interface doping, lithium is often deposited as a monolayer film of Li, $Li_2O$, or LiF between the organics and the metal cathode.

Another option is the coevaporation of Li from a dispenser source together with an organic material forming electrically doped bulk material of desired thickness. In most cases, the metal cathode is deposited afterward, such that there is a high energy input into the device, which causes the Li atoms to diffuse into the organic layers, resulting in an n-doped organic film of usually unknown thickness, see below. The most widely used system is tris(8-hydroxyquinoline)aluminum ($Alq_3$)/Li(F)/Al, where (F) shall describe the decomposition of LiF leading to chemical doping. Such devices

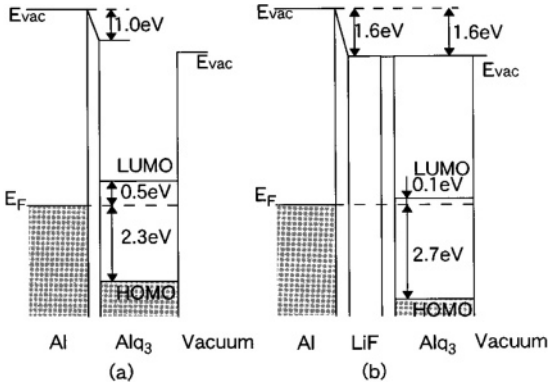


**Figure 15.** Energy diagrams of (a) the undoped $Alq_3$/Al interface and (b) the doped $Alq_3$/LiF/Al interface. Reused with permission from T. Mori, H. Fujikawa, S. Tokito, and Y. Taga, *Applied Physics Letters, 73*, 2763 (1998). Copyright 1998, American Institute of Physics.

possess a good electron injection and normally low driving voltages. An example for an OLED comprising a Li-doped $Alq_3$ layer is shown in Figure 28 (see section 4.2.3), where the Kodak group studied the influence of LiF on the OLED performance. Here, it should be noted that not the deposition of LiF itself on, for example, $Alq_3$ leads to a doping effect: Hung et al. could show by X-ray photoelectron spectroscopy (XPS) that LiF remains undissociated upon sublimation and deposition on $Alq_3$.[118] However, as shown in a later study by the same group, the deposition of Al onto the $Alq_3$/LiF stack leads to a dissociation of LiF by an exothermic reaction of LiF with Al under the presence of $Alq_3$, which may release free $Li^+$ ions into the organic layer underneath.[60] However, no $Li^+$ ions could be detected during these experiments. Other groups investigated the same interface also by XPS, such as Grozea et al., who lifted off the organic from its metal interface.[61] In these experiments, they found both Li−F bonds and C−F bonds indicating a reaction that may release Li.

The energetics of the $Alq_3$/LiF/Al interface has been studied in detail, for example, by Mori using UPS.[62] They showed nicely the Fermi level shift caused by Li doping for this frequently used electron injection system, see Figure 15.

In 1998, Kido reported efficient OLEDs with an electron transport layer consisting of bathophenanthroline (BPhen) with Li doping of the bulk.[63] Parthasarathy et al. studied the Li doping of organic material in detail.[22] For Li-doped BCP, they found a conductivity, $\sigma$, of $3 \times 10^{-5}$ S/cm for a 100 nm thick Li/BCP film, which is a suitable value for OLED applications. The sample setup for this experiment was ITO/organics (10−640 nm)/Li (0.5−1 nm)/Al, where the organics were BCP, $Alq_3$, and copper phthalocyanine (CuPc). An analysis of Li diffusion into the organics by secondary ion mass spectrometry (SIMS) depth profiling showed a strong Li diffusion up to 80 nm into the organic material. In contradiction to these findings are data of D'Andrade[154] for the penetration depth of Li into BPhen, as determined by ellipsometry. They found a penetration depth of only 10 nm into BPhen from a 0.8 nm thick Li layer. The difference between both experiments was the metal deposition: Parthasarathy coated the organics/Li stack with metal, whereas D'Andrade did not. This indicates that bulk doping can be reached by Li deposition on top of the organics layers, if it is followed by metal deposition. The high temperature during metal deposition may cause the Li ions to diffuse into the organics.

However, the same effect is also a drawback: In long-term studies, one finds often a short lifetime for Li-doped OLEDs, which is attributed to Li diffusion into other layers where Li is not desired. For example, Li may act as luminescence quencher when it diffuses into the emission layer.[23]

Similar to lithium, cesium (Cs) acts as an efficient electron donor in organic films. Cs is often directly coevaporated with an organic material. A mixed layer of 1:1 Cs atoms/organic molecules is usually prepared. As lithium, Cs may be also deposited either from a salt by thermal evaporation or from a dispenser source containing a Cs salt or alloy. The main advantage of Cs doping compared with Li is the lower diffusivity of Cs because of its atomic dimensions, which makes the devices less sensitive to temperature and which helps to isolate Cs in the charge-transport layers only. This is important with respect to the above-mentioned emission quenching caused by alkali metal ions in the emission layer.[23]

### *2.2.2. n-Type Doping by Organic Materials with a High-Lying HOMO*

A first study of controlled n-type doping in molecular organic semiconductors was presented by Nollau et al.[14] They doped naphthalene tetracarboxylic dianhydride (NTCDA) by cosublimation with the donor molecule bis(ethylenedithio)-tetrathiafulvalene. It was shown that the Fermi level shifted toward the transport level and that the magnitude of conductivity was increased. However, the conductivities achieved were rather low and only 1−2 orders above the background conductivity of nominally undoped NTCDA.

More recently, the n-type doping of the two organic semiconductors, hexadecafluorophthalocyaninatozinc ($F_{16}ZnPc$) and tris(8-hydroxyquinoline)aluminum ($Alq_3$), by the dopant molecule tetrathianaphthacene (TTN) was investigated by UPS.[64] The dependence of the UPS spectra on the doping suggested that TTN acts as an efficient donor in $F_{16}ZnPc$; the doping effect for $Alq_3$ was almost zero. The results could be explained by the energetic position of the energy levels, which allow an energy transfer from the dopant to the phthalocyanine LUMO but not to the higher lying $Alq_3$ LUMO.

Another spectroscopic study of n-type doping was reported by the Kahn group: They investigated the n-doping of an electron-transport material, a tris(thieno)hexaazatriphenylene derivative, with the strongly reducing molecule bis(cyclopentadienyl)-cobalt(II) (cobaltocene, $CoCp_2$). As techniques, ultraviolet, X-ray, and inverse photoemission spectroscopies and current−voltage measurements were used.[65] Cobaltocene was chosen because condensed $CoCp_2$ films have an ionization energy of 4 eV, being unusually low for vacuum-deposited molecular material. This makes cobaltocene a promising material for molecular n-doping. A doping effect on the tris(thieno)hexaazatriphenylene derivative by cobaltocene was indicated by a 0.56 eV shift of the Fermi level toward the unoccupied states of the host. Additionally, a 3 orders of magnitude current increase in devices where the compound was interfacially doped with cobaltocene was demonstrated.

Other examples for materials with high-lying LUMO are the compounds proposed by Elliott et al.[66] shown in Figure 16. Unfortunately, these materials are still not strong enough donors to obtain sufficient n-type conductivity in typical OLED electron transport materials. Recently, a proprietary material was released by Novaled AG,[67] which was suc-

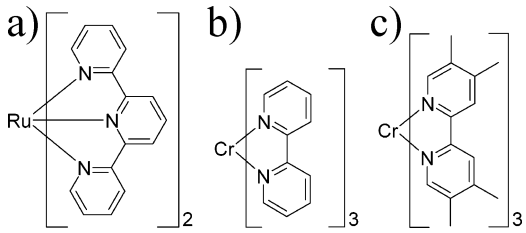


**Figure 16.** Structures of metal complexes suitable as molecular n dopant: (a) $[Ru(terpy)_2]^0$; (b) $[Cr(bpy)_3]^0$; (c) $[Cr(TMB)_3]^0$. Reprinted with permission from ref 66. Copyright 2003 American Chemical Society.

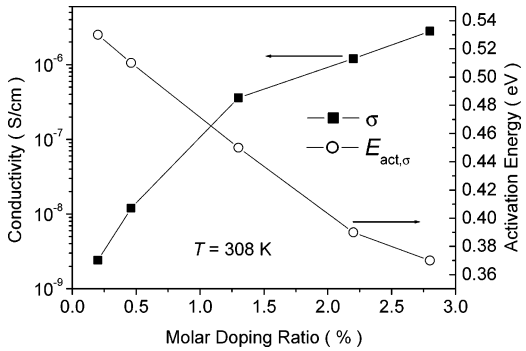


**Figure 17.** Conductivity (■) at room temperature and activation energy (○) of the conductivity in $[Ru(terpy)_2]^0$ doped ZnPc thin fims as a function of doping ratio.

cessfully used for n-type doping of OLEDs. The main advantages of such materials compared with metal doping are the higher temperature stability and the easier control of the evaporation.

We now briefly discuss some n-type doping experiments that we have used in the quest to realize a p−n homojunction. To obtain a suitable n-dopant, we used the results of Bloom et al.,[66] who have demonstrated that the electrochemically reduced form of the transition metal complex bis(terpyridine)ruthenium, $[Ru(terpy)_2]^0$, can be a promising electron-injecting cathode material in OLEDs due to its low work function. The oxidation potential of $[Ru(terpy)_2]^0$ is as low as −1.7 V vs $Ag/Ag^+$.[68,69] We have chosen ZnPc as the matrix because its reduction potential of approximately −0.93 V vs SCE (approximately −0.9 V vs $Ag/Ag^+$)[70] should allow an electron transfer from the donor $[Ru(terpy)_2]^0$. Furthermore, the properties of p-type ZnPc (p-ZnPc) layers doped with tetrafluoro-tetracyanoquinodimethane ($F_4$-TCNQ) are well investigated.

The donor compound $[Ru(terpy)_2]^0$ was synthesized in its $2^+$ oxidation state and electrochemically reduced.[66] Matrix and dopant were coevaporated from ceramic crucibles in an ultrahigh vacuum (UHV) chamber. All handling of $[Ru(terpy)_2]^0$ was carried out in an inert atmosphere.

For a molar doping ratio of 1:35 of $[Ru(terpy)_2]^0$ in ZnPc, we achieved conductivities of $2.7 \times 10^{-6}$ S/cm at room temperature (Figure 17). The conductivity increases superlinearly with the doping ratio, indicating shallow donor states according to the model of Maennig et al.[13] Field-effect measurements confirm n-type conduction for a molar doping ratio of 1:41. From the conductivity and field-effect mobility, one obtains an electron concentration of $7 \times 10^{17}$ $cm^{-3}$.

### 2.2.3. n-Type Doping with Cationic Salts

As discussed above, the conventional approach requires donor molecules with high-lying HOMOs, namely, low oxidation potentials. An approach for n-doping by organic molecules with a fixed positive charge in a nonconjugated side group has recently been presented by Gregg et al. and yields very high conductivities.[71] However, this approach is unfortunately limited to solution-processed films, because these dopants cannot be evaporated.

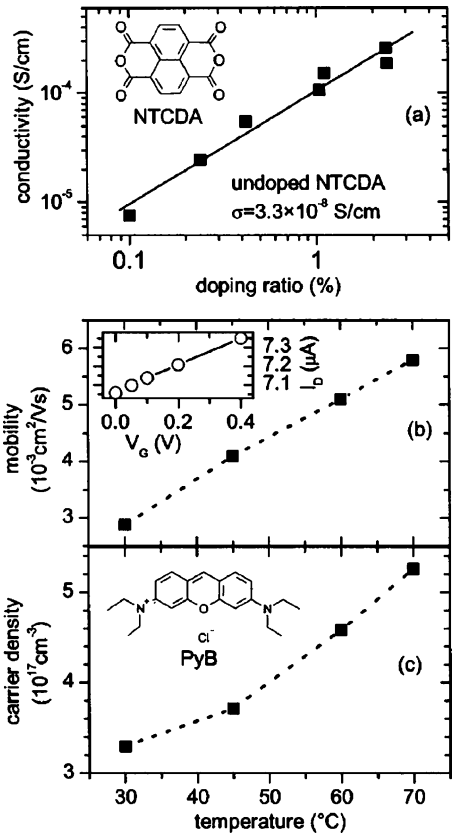


**Figure 18.** Electrical properties of doped NTCDA thin films: (a) conductivity of doped NTCDA layers vs doping concentration; (b) field-effect mobility of a 1:91 doped NTCDA layer (inset, typical field-effect signal); (c) electron density derived from field-effect measurement. Reused with permission from A. G. Werner, F. Li, K. Harada, M. Pfeiffer, T. Fritz, and K. Leo, *Applied Physics Letters*, *82*, 4495 (2003). Copyright 2003, American Institute of Physics.

Recently, we have developed an alternative novel doping method using salts of cationic dyes like rhodamine B as stable precursors for strong molecular donors.[15,16,17] In this approach, the volatile donor was created *in situ* from a stable precursor compound. As an example, we show data for the n-doping of NTCDA with pyronin B chloride (see ref 15). It is obvious that the coevaporation of the dopant increases the conductivity of NTCDA by several orders of magnitude (Figure 18).The doping effects of the system NTCDA/pyronin B have also been investigated by the Kahn group. Experimental techniques applied were ultraviolet photoelectron spectroscopy (UPS), inverse photoelectron spectroscopy (IPES), and current−voltage ($I-V$) measurements.[72] The authors demonstrated that the deposition of small amounts of pyronin B (PyB) on NTCDA films leads to a shift of all the molecular levels away from the Fermi level by nearly 0.20 eV, indicating the n-type doping effect. Similarly, the interface and bulk energy levels of coevaporated layers show efficient n-doping. Additionally, electrical measurements proved a 4 orders of magnitude increase in current in doped films. The data showed that both the leuco and neutral radical forms are present in the condensed phase, with the leuco

PyB having a higher concentration. The neutral radical form was identified by the authors as the species mainly responsible for doping.

In another study, combined FT-IR, UV/vis/NIR, and mass spectroscopic measurements suggested the formation of leuco bases of the cationic dyes during the sublimations of xanthene cationic dyes (pyronin B and rhodamine B) and triphenylmethane cationic dyes (malachite green and crystal violet).[16,17] It was observed that the leuco forms are transformed back to the dye cation upon oxidation. Consequently, cationic dyes and their bases give a similar doping effect in organic electron transport materials with low-lying LUMOs. The availability of the leuco base of cationic dyes, such as leuco crystal violet (LCV) and leuco malachite green allowed direct testing of the proposed role of the leuco base as an intermediate species in the course of n-type doping. The leuco base itself is not a strong electron donor and cannot directly donate electrons to matrices because of its higher oxidation potential. Electron transfer between donors and acceptors, accompanied by a hydride transfer, leads to an n-type doping effect. We have also observed that for moderate electron acceptors such as $C_{60}$ doped with cationic dyes or their bases, an irreversible electron-transfer reaction leading to a stable n-doping effect can only be induced by illumination or heating.

To discuss this observation, we select LCV and $C_{60}$ as samples to illustrate the process of light-induced electron transfer between leuco bases of cationic dyes and electron transport materials with low-lying LUMOs, as shown in Figure 19. When LCV is excited by light, an electron is lifted from the HOMO to the LUMO. Subsequently, this electron moves to the lower-lying LUMO of the adjacent $C_{60}$ (Figure 19a) to reach an energetically more favorable state. In this way, two radical ions, $LCV^{+\bullet}$ and $C_{60}^{-\bullet}$, are formed (Figure 19b). Now, the radical electron in the LUMO of $C_{60}$ could return to the HOMO of LCV, which would not correspond to a permanent doping process. However, at this stage there is obviously a competing, nonreversible reaction channel, namely, a hydride transfer reaction of $LCV^{+\bullet}$ to $C_{60}$. By this hydride transfer, the unstable LCV radical cation with a half-filled HOMO is transformed into the stable, nonradical CV cation with a fully occupied HOMO (Figure 19c); that is, back transfer of the electron on $C_{60}$ is no longer possible and a permanent doping effect with an enhanced equilibrium electron density on $C_{60}$ is achieved. Such transfer reactions have been observed when LCV meets stronger oxidants such as DDQ or TCNQ. LCV can be oxidized directly to a CV cation by the hydride transfer accompanied by electron transfer.[73−75] For weaker acceptors like $C_{60}$, the combined hydride and electron-transfer reaction obviously has to be supported by outer activation (light or heating).

Conductivity studies of organic electron transport materials (with low-lying LUMOs) doped with the cationic dyes have been carried out as well.[16,17] All dopants used in the study give rise to an increase of several orders of magnitude in conductivity with dopant concentration compared with undoped organic thin flms. Table 3 gives conductivity and activation energy results for doped and undoped thin flms.

The novel cationic doping method has already been successfully applied for solar cells where materials with lower lying LUMOs are used for electron transport.[36,76] Already at a doping level of 0.2%, the conductivity was well above $10^{-5}$ S/cm, which is high enough to achieve negligible Ohmic losses in a 50 nm thick electron transport layer of an organic solar cell.

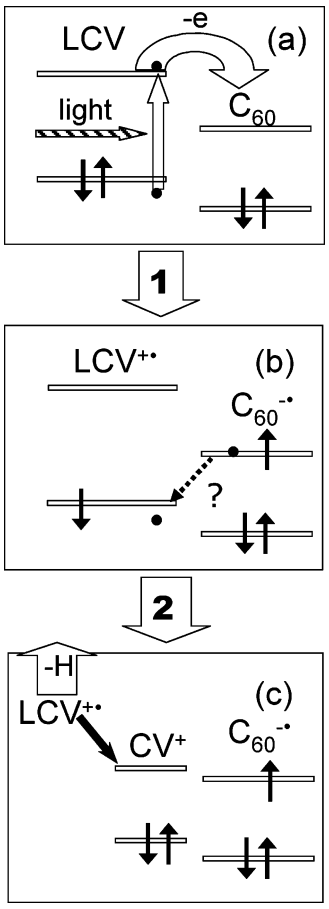


**Figure 19.** Illustration of the proposed mechanism of photoinduced electron transfer from LCV to $C_{60}$. The n-doping effect becomes permanent by the stabilization of the positive charge on the dopant by hydride transfer to $C_{60}$.

However, cationic dyes and their bases have not allowed achievement of a significant n-type doping effect for electron transport materials used in OLEDs. The electron transport materials such as $Alq_3$ or 3-(4-biphenylyl)-4-phenyl-5-tert-butylphenyl-1,2,4-triazole (Bphen) obviously require dopants with even lower oxidation potential.

## 2.3. Contacts with Doped Semiconductors

As argued above, doping leads to higher conductivities, which reduce the operating voltages of devices due a lower potential drop in the transport layers. A second effect, which actually might be even more important for device applications has been outlined in the comparison with inorganic LEDs in the introduction: The energetic alignment at the contact plays a crucial role when making Ohmic contacts with metals (or highly doped transparent oxides, as frequently used in OLEDs). Ideally, one would choose the contact materials such that the work function of the metals or conductive oxides aligns with the LUMO level at the electron injection contact or with the HOMO at the hole injection contact.

However, due to constraints in materials choices, this is rarely possible. For instance, the typical OLED electron transporting materials have electron affinities around 3 eV, which would require very reactive materials for Ohmic contacts. On the hole side, the typical conductive oxides have

**Table 3. Conductivity and Activation Energy of Several Matrices Using Various Cationic Dyes as Dopants[a]**

| matrix | dopant | doping ratio (mol %) | conductivity (S/cm) | activation enegy (eV) |
|---|---|---|---|---|
| C60 | undoped | 0 | $3.80 \times 10^{-8}$ | 0.64 |
| | pyronin B | 2.90 | $1.39 \times 10^{-3}$ | 0.27 |
| | crystal violet | 3.52 | $7.90 \times 10^{-3}$ | 0.14 |
| $F_{16}$ZnPc | undoped | 0 | $5.60 \times 10^{-11}$ (50 °C) | 0.91 |
| | pyronin B | 2.06 | $3.70 \times 10^{-5}$ | 0.34 |
| | malachite green | 3.00 | $1.19 \times 10^{-6}$ | 0.39 |
| NTCDA | undoped | 0 | $6.20 \times 10^{-11}$ (40 °C) | 0.54 |
| | pyronin B | 2.06 | $9.29 \times 10^{-4}$ | 0.22 |
| | malachite green | 2.00 | $1.94 \times 10^{-4}$ | 0.21 |
| | crystal violet | 3.38 | $6.67 \times 10^{-4}$ | 0.29 |

[a] All conductivity data are measured at 30 °C unless specified differently in the table.

work functions that are too small for hole injection. In most contact systems for inorganic semiconductors, these problems are solved by introduction of highly doped space charge layers. Many contact materials for inorganic devices are compounds consisting of a noble metal with an admixture of another metal that produces a doping effect. After deposition, the contacts are then annealed at a temperature where the admixture diffuses into the semiconductor and forms a highly doped space charge region. This region leads to a thin barrier where the carriers can easily tunnel through.

We have shown in a spectroscopic study that there is an exactly corresponding effect for organic contacts.[12] The experiments used X-ray and ultraviolet photoemission to study the energetic levels of contact materials and organic semiconductors close to the interface. As model system for the organic semiconductor, zinc phthalocyanine and $F_4$-TCNQ was chosen. As substrates, both ITO and polycrystalline gold were used. The organic layers were evaporated in steps on the substrates; after each step, spectra were taken to follow the energy levels as a function of the thickness of the organic layers. The work function and the HOMO levels were determined using well-established methods of photoelectron spectroscopy.[12]

Figure 20 shows the results for nominally undoped ZnPc (top) and 1:30 doped ZnPc (bottom) on an ITO substrate. In both cases, a rather large energy barrier for holes of about 1.2 eV is visible; also, both cases show a small interface dipole, which is probably caused by a local charge transfer at the interface. For the undoped samples, there is a weak level bending observable in the organic semiconductor, leading to a space charge region of approximately 15 nm. The HOMO level of the ZnPc is about 0.8 eV away from the Fermi level, which is consistent with an undoped semiconductor where the Fermi level is in the band gap center. There is a weak level bending on spatial dimensions of tens of nanometers for which we have no definite explanation. Possibilities are impurities or oxygen released from the ITO surface.

For the doped semiconductor, there is a much stronger level bending of 0.9 eV. The Fermi level is now only 0.23 eV away from the HOMO level, which is consistent with the data presented in section 2.1. The space charge layer is now very thin, below the experimental resolution of 5 nm. A calculation using the Poisson equation yields 2.5 nm.

Most interesting are the electrical properties of such contacts: Undoped phthalocyanines on ITO form blocking contacts, as is expected for the energetic alignment in Figure 20, top. Contacts with doped phthalocyanines, however, are Ohmic despite the rather large barrier. One can thus conclude that the basic mechanism of forming an Ohmic contact by thin tunnel barriers works as well as in inorganic semiconductors. In Figure 21, the difference in the device performance for the different contacts of ITO/ZnPc and ITO/p-ZnPc is shown.

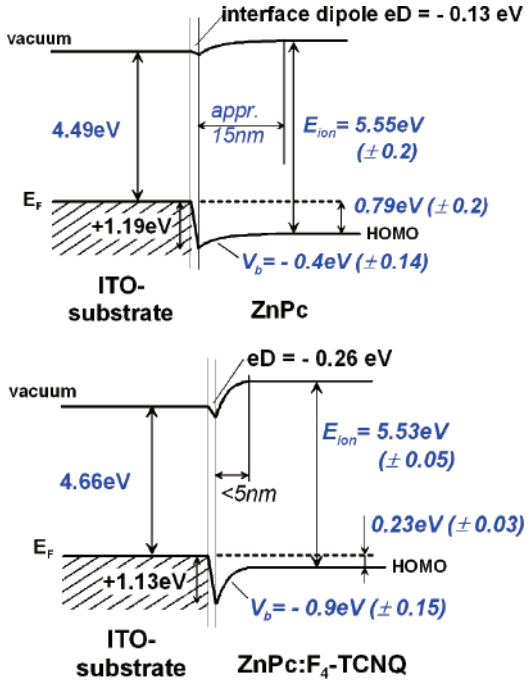


**Figure 20.** Energy diagram as derived from UPS/XPS spectroscopy for the organic semiconductor ZnPc on ITO: top, undoped ZnPc on ITO; bottom, ZnPc doped with $F_4$-TCNQ. Reprinted from ref 12, Copyright 2001, with permission from Elsevier.

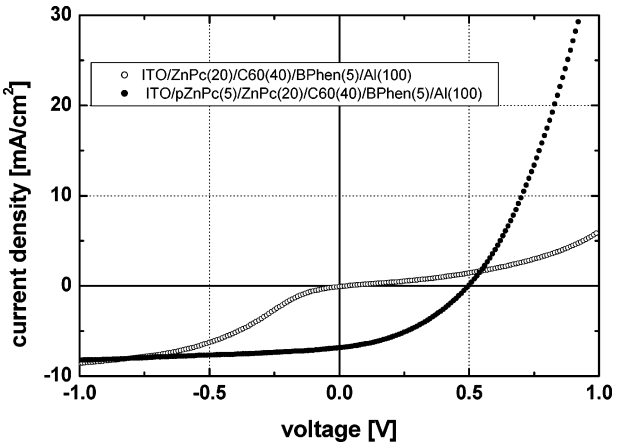


**Figure 21.** Comparison of $I-V$ characteristics of two samples with ITO/p-doped ZnPc (●) and ITO/undoped ZnPc (○) contacts. The latter sample shows clear evidence of a contact barrier.

Another issue of comparable importance is the influence of electrical doping on organic−organic heterojunctions. The first study to investigate this issue was reported in ref 77. The authors studied the interface molecular level alignment at organic−organic heterojunctions using photoemission spectroscopy. Specifically, the interfaces between hole transport layers (HTLs) and electron transport layers (ETLs) were investigated as a function of p-doping of the HTLs. It was shown that doping induced the formation of an interface dipole with corresponding shift in the relative position of molecular levels across the interface, which was explained by the presence of doping-induced excess holes at the interface.

We would like to mention here that in the past few years many groups have improved the understanding of contacts between organics and metals by spectroscopic experiments.[78−83] In particular, our work on the interface of doped organics of metals was extended to many other systems.[84−86]

## 3. p−n Homojunctions

### 3.1. Background

The archetype of any semiconductor device is a diode, using the same matrix material in p- and n-doped form. Despite the fact that organic semiconductors have been investigated for decades and have been used in commercial products for some years, a reproducible and stable p−n homojunction had not been presented until recently.[18] The main challenge to be solved in realizing such a device was to find a set of materials that allows the simultaneous p- and n-type doping with a suitable device design: since organic semiconductors have to be highly doped to overcome the typically rather high impurity concentrations, it is necessary to use a p−i−n junction design to achieve blocking behavior.

In previous work, despite some attempts with less well-defined systems,[87,88] no stable and reproducible p−n homojunction could be achieved, and no detailed study of the junction formation and properties was carried out. In particular, it was not possible to investigate whether such an organic p−n junction follows the standard Shockley model[89] for p−n junctions. This is an interesting question since, for example, for semiconductor junctions based on amorphous silicon, deviations from the Shockley model due to recombination at defects in the intrinsic layer distributed in energy and space[90,91] have been reported.

The main problem connected with simultaneous n- and p-type doping is the energetics of the dopant molecules: For p-type doping, molecules are needed with the lowest unoccupied orbital (LUMO) energetically located near or below the highest occupied molecular orbital (HOMO) of the organic semiconductor host. For the case of n-type doping, the HOMO of the dopant has to be near or above the LUMO of the host semiconductor (see Figure 22 for a scheme).

It is thus clear that for doping the same matrix with both n- and p-type dopants, one has to obtain dopant molecules that have very high and low lying orbitals, respectively. Thus, a p−n heterojunction is much easier to realize: the two different host materials can be chosen in a way that the energy difference between the LUMO of the n-host and the HOMO of the p-host is small. However, it is also obvious that the open-circuit voltage of such an arrangement is limited, compared with a true homojunction. Furthermore, from a scientific point of view, it is interesting to study the properties of a junction where the effect of the heterojunction is not superimposed.

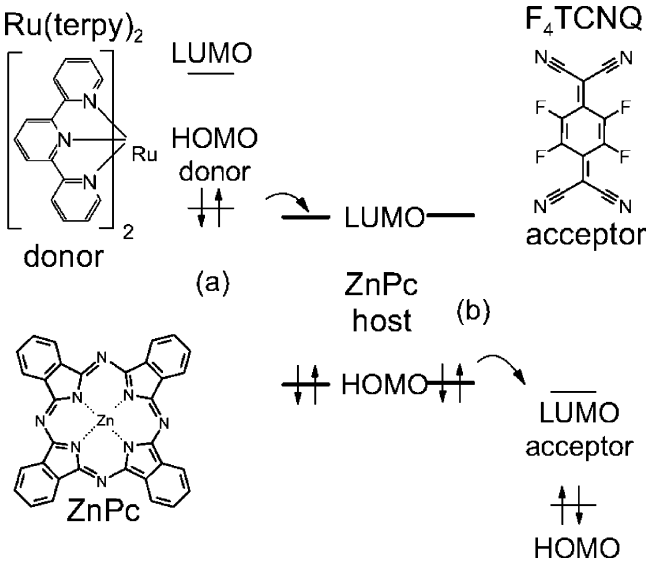


**Figure 22.** Energy level scheme of n-type (a) and p-type (b) doping of an organic material, shown at the example of ZnPc. Reprinted Figure 1 with permission from Harada, K.; Werner, A. G.; Pfeiffer, M.; Bloom, C. J.; Elliott, C. M.; Leo, K. *Phys. Rev. Lett.*, *94*, 036601, 2005 (http://link.aps.org/abstract/PRL/v94/e036601). Copyright 2005 by the American Physical Society.

**Table 4. Doping Parameters and Layer Structures of the Homojunctions**

| | doping ratio/thickness of layer (nm) | | |
|---|---|---|---|
| type of junction | p-ZnPc | i-ZnPc | n-ZnPc |
| p−i−n homo | 1:38/15 | −/30 | 1:46/40 |
| M−i−n | | −/50 | 1:41/100 |

### 3.2. Experiments

As reported above, efficient p-type doping of various organic hole transport materials, including zinc phthalocyanine (ZnPc), has been obtained previously,[10,13] achieving rather high carrier concentrations of up to $10^{20}$ $cm^{-3}$. Due to the high carrier concentrations mentioned above, the space charge regions of organic semiconductors are comparatively narrow and typically in the range of a few nanometers.[12] Thus, the space charge layer of an intimate p−n junction would be easily tunneled through by charge carriers so that a clear rectification effect is probably not observed. Therefore, the diodes require an undoped *intrinsic layer* between the p- and n-layers to enable good rectification characteristics. The p−i−n homojunction is thus formed by three ZnPc layers: p-ZnPc/i-ZnPc/n-ZnPc.

We have also realized for comparison a metal−semiconductor (Schottky) junction: The M−i−n diode consists of ITO/i-ZnPc/n-ZnPc, where ITO plays the role of the metal. The layer structures and doping parameters of these junctions are given in Table 4; the schematics of the diode structures are shown as insets in Figure 23a. We use impedance spectroscopy and current−voltage ($I-V$) characteristics to study our diodes, as discussed in the following.

We have used capacitance−voltage ($C-V$) spectroscopy to determine the built-in potential, $V_{bi}$, of the diodes. The capacitance of a diode is mainly controlled by the width of the depletion layer, being a function of the applied bias voltage, $V$. Forward bias reduces the width of the space

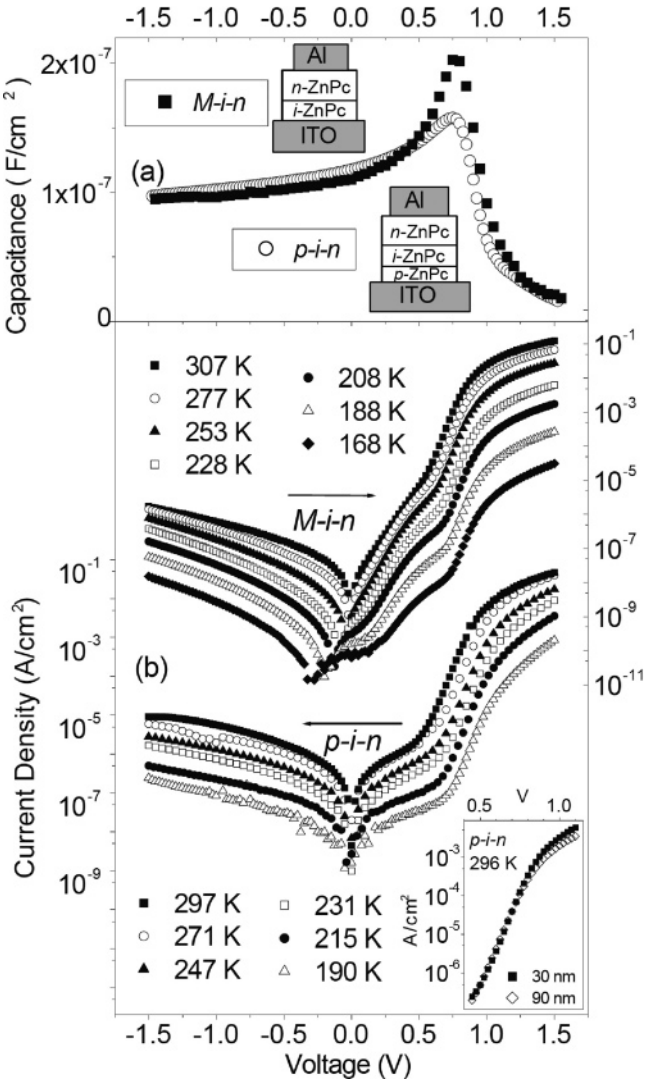


**Figure 23.** (a) $C-V$ spectra of a p−i−n junction measured at 3 kHz and the M−i−n homojunction measured at 2 kHz (insets depict the schematics of both p−i−n and M−i−n samples) and (b) $I-V$ characteristics of the M−i−n junction and p−i−n homojunction (i thickness 30 nm) at various temperatures. The linear part between 0.5 and 0.8 V reflects the junction properties, while the characteristics are controlled by an inevitable shunt resistance below 0.5 V. The inset shows $I-V$ characteristics of p−i−n samples with i thicknesses of 30 and 90 nm at room temperature. Reprinted Figure 2 with permission from Harada, K.; Werner, A. G.; Pfeiffer, M.; Bloom, C. J.; Elliott, C. M.; Leo, K. *Phys. Rev. Lett., 94*, 036601, 2005 (http://link.aps.org/abstract/PRL/v94/e036601). Copyright 2005 by the American Physical Society.

charge region, and the space charge region finally vanishes when $V$ reaches $V_{bi}$.

Figure 23a displays the $C-V$ spectra of the two types of junctions. The capacitance collapses for both samples for applied voltages exceeding 0.8 V; that is, the p−i−n and M−i−n diodes have a built-in potential of approximately 0.8 V at room temperature. This is, for example, considerably larger than that for doped organic heterojunction solar cells[36] consisting of ZnPc and fullerene $C_{60}$. Additionally, we prepared another ZnPc p−i−n homojunction with a Au contact (ITO/Au contact couple), instead of the Al top contact. The ITO/Au sample yields a similar $I-V$ curve and a comparable built-in potential to the ITO/Al sample. Since only a negligible, or even negative, work function difference is expected between ITO and Au, it is clear that a significant influence of the metal work function of the Ohmic contacts can be excluded for the $I-V$ characteristics. Therefore, the built-in potentials of our homojunctions are due to the difference in the Fermi levels of the doped ZnPc layers, rather than to the work function differences of the metal electrodes. The work function of ITO is similar to i-ZnPc.[12] Therefore, almost no built-in potential is expected between the ITO and the i-ZnPc layer. Consequently, n-doping of ZnPc with $[Ru(terpy)_2]^0$ quite efficiently moves the Fermi energy of the matrix to the conduction states of the LUMO.

The general diode equation,

$$J = J_0\left[\exp\left(\frac{qV}{nkT}\right) - 1\right] \tag{7}$$

describes the $I-V$ characteristics of both p−n junctions and Schottky diodes. Here, $J_0$ is the saturation current, $V$ is the applied voltage, $k$ is the Boltzmann constant, $T$ is the temperature, and $n$ is the so-called ideality factor. This factor $n$ is unity in the Shockley theory for p−n junctions in the absence of recombination, as well as for thermionic emission theory and diffusion theory for Schottky diodes. The parameters ideality factor and the saturation current can be obtained from the slope and the intercept, respectively, of the linear part (approximately in the interval from 0.5 to 0.8 V) of the semilogarithmic plot of $J$ vs $V$. Figure 23b displays the temperature dependence of $I-V$ plots from the p−i−n homojunctions and the M−i−n junction. Both types of junction show blocking behavior. In the forward direction, the $I-V$ curves below 0.5 V are dominated by excessive currents due to shunt resistances. Between 0.5 and about 0.8 V, the curves are determined by the junction properties and accordingly show an exponential increase. Above the built-in voltage of 0.8 V, the currents level off.

The data in Figure 23b illustrate that the standard diode equation with a temperature-independent $n$ does not agree with our data since the slopes of the linear parts of the semilogarithmic $I-V$ plots only weakly depend on temperature; that is, $n$ increases when the temperature $T$ decreases. The $n$-factors of our p−i−n and M−i−n samples at room temperature are $n = 1.8-2.0$, which can be observed for inorganic semiconductors as well if the current is strongly influenced by recombination at traps. However, for decreasing temperature, the value of $n$ strongly increases up to values of about 4, as is visible in Figure 24a. Such behavior is not observed in crystalline inorganic semiconductors and is not explicable in the Shockley model, if the case of the p−i−n diode is considered.

The deviation from the Schottky theory for the M−i−n is also obvious from another experimental finding. The Schottky barrier height, $\Phi_B$, of the M−i−n diode can be estimated by fits to the saturation currents at various temperatures, see Figure 24b. The best fit is obtained for $\Phi_B = 0.34$ V, that is, surprisingly much lower than the $V_{bi}$ obtained from the $C-V$ plot. For the p−i−n diode, the saturation current exhibits a temperature dependence similar to the M−i−n junctions, Figure 24b. In Shockley theory, the temperature dependence is determined by the band gap of the semiconductor. For ZnPc, we estimate the gap to be at least 1.6 eV from the energy of the lowest absorption band.[13] This value again exceeds the value obtained by the saturation current by a large factor.

Before proceeding further, we here summarize the arguments above and the perspective for the following discussion. Each $I-V$ curve of our diodes can be described either by

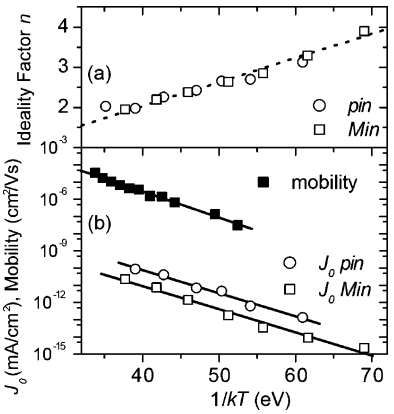


**Figure 24.** Temperature dependence of (a) the ideality factors, *n*, and (b) the saturation current, $J_0$, of p−i−n and M−i−n samples. For comparison, in panel b, the field-effect mobility of a [Ru(terpy)$_2$]$^0$/ZnPc (1:41) layer is given. Reprinted Figure 3 with permission from Harada, K.; Werner, A. G.; Pfeiffer, M.; Bloom, C. J.; Elliott, C. M.; Leo, K. *Phys. Rev. Lett., 94*, 036601, 2005 (http://link.aps.org/abstract/PRL/v94/e036601). Copyright 2005 by the American Physical Society.

the Shockley theory or by the diffusion theory. However, the temperature dependence of the diode parameters is not described by the classical models: that is, the ideality factor *n* does not follow the 1/(*kT*) rule, and the saturation current, $J_0$, does not depend in the expected way on the built-in potential. The Shockley theory of p−n junctions neglects the presence of the local field for the derivation of the current equation. In the following, we discuss a diffusion model for the M−i−n characteristics taking into account the local field in the intrinsic layer. This diffusion theory had to be modified in order to explain the experimental results. The behavior of the p−i−n sample with thick intrinsic layer could be described in nearly the same way as the M−i−n sample using the diffusion theory, which is also indicated by the nearly identical behavior of *n* and $J_0$. In principle, the diffusion theory seems to be most applicable to describe the M−i−n diode characteristics because the very low charge carrier mobility in organic solids is included.

We have shown that the temperature dependence of the ideality factor and the low barrier height obtained from the *I*−*V* plot can be explained by considering deviations from the Einstein relation in disordered systems.[18] This approach suggests that first, the ideality factor should scale with 1/*T* as is indeed obtained for our diodes (see Figure 24). Second, the thermal activation of $J_0$ is solely given by the temperature dependence of the mobility, $\mu$. Field-effect measurements of a doped n-ZnPc layer (doping ratio 1:41) yield an activation energy of 0.34 eV for the mobility, which is comparable to the slopes of ln $J_0$ vs 1/*T* for both diodes (0.34 eV). The evident similarities of the parameters for M−i−n and p−i−n diodes indicate that the latter is likewise described by a diffusion-limited theory,[92] rather than Shockley theory.

## 4. Organic Light-Emitting Diodes (OLEDs) with Doped Transport Layers

### 4.1. OLEDs: A Brief Introduction

#### 4.1.1. General Considerations

Electrically stimulated light emission from organic molecular crystals was observed already in 1953, when Bernanose et al. discovered the AC electroluminescence of acridine orange and quinacrine.[93,94] However, it remained a scientific curiosity until 1987, when Tang and Van Slyke[95] in a pioneering work developed the first thin-film heterojunction organic light-emitting diode (OLED) based on a fully organic heterojunction of a hole-transporting and an electron-transporting material, the latter being at the same time the light-emitting layer. The organic stack was embedded between two suitable Ohmic electrodes. An OLED of this type relies on a transparent, high work function anode (usually glass coated with electrically conductive indium tin oxide (ITO)), an organic hole injection and transport layer, an organic emission and electron transport layer, and a reflective cathode with low work function, like MgAg or Al.

Since then, the field of OLEDs has undergone tremendous development, leading not only to scientific breakthroughs, but also to first commercial devices. With the introduction of light emitting polymers by the group of Friend in 1990,[96] the field of OLEDs split into two branches, dealing with either small molecule OLEDs (also called SM-OLEDs) or polymeric OLEDs (or PLEDs). In 1997, the Japanese company Pioneer introduced a car stereo with an OLED display. Nowadays, a large number of academic research groups and companies develop OLEDs, following both the polymeric and the small molecule routes. Commercially, up to now mostly passive matrix displays with display diagonals up to 3.8 in. have been addressed. However, meanwhile also larger demonstrators with display diagonals up to 40 in. have been presented.[97] As a new branch, OLED lighting and signage is currently developing, using the OLED not in a patterned high-value, small-size device but in a low-cost, large-area arrangement to obtain a novel source for general lighting. Due to these differences, the challenges of OLED lighting are unique from those in OLED display development, such that OLED lighting requires independent solutions.

#### 4.1.2. A Few Remarks on the Efficiency Limitation of OLEDs

The efficiency of an OLED may approximately be calculated by

$$\eta_{\text{external}} = b_{\text{I}} \frac{h\nu}{eU} \eta_{\text{recomb}} \eta_{\text{optical}} \tag{8}$$

where $\eta_{\text{external}}$ is the total power efficiency of the device, $b_{\text{I}}$ is the carrier balance, *U* is the operating voltage, $\eta_{\text{recomb}}$ is the quantum efficiency of carrier recombination, and $\eta_{\text{optical}}$ is the efficiency of the optical outcoupling from the device. In SM-OLEDs, due to their multilayer structure, the charge carrier balance, $b_{\text{I}}$, may be adjusted rather simply by choosing suitable blocking layers, which confine the carriers inside the emission zone and force them to recombine with their counterpart within the emission layer.

The second issue is driving voltage. Ideally, it should approximately correspond to the energy of the emitted photons. Initially, organic light-emitting diodes had rather high operating voltages, since the injection at the contacts was characterized by rather large barriers, and the carrier transport in the nominally undoped layers caused further voltage drops. As we show in this work, doping the charge transport layers reduces their internal electrical losses, leading to drive voltages in the range of the energy of the emitted light plus the exciton binding energy. A detailed description

of the voltage limits of OLEDs has been discussed recently by Meerheim et al.[98]

The third factor that defines the efficiency of an OLED is the ratio of radiative recombination of excitons to the total number of excitons. When examined more closly, it is composed of two factors:

$$\eta_{\mathrm{recomb}} = \eta_{\mathrm{ST}} \frac{\eta_{\mathrm{r}}}{(\eta_{\mathrm{r}} + \eta_{\mathrm{nr}})} \tag{9}$$

Here, $\eta_{\mathrm{ST}}$ is the ratio of singlet and triplet excitons contributing to the radiative recombination and

$$\frac{\eta_{\mathrm{r}}}{(\eta_{\mathrm{r}} + \eta_{\mathrm{nr}})} \tag{10}$$

is the ratio of radiative recombination of excitons versus the total number of excitons. The latter ratio can be assigned to the photoluminescent (PL) quantum yield, which is a substance-specific quantity. For some substances, such as the molecule *fac*-tris-(2-phenylpyridine) iridium [$Ir(ppy)_3$], the PL quantum yield may even reach unity when incorporated in an appropriate solid matrix material.[99]

By spin statistics, $\eta_{\mathrm{ST}}$, which is the ratio of singlet and triplet excitons, should be $\eta_{\mathrm{ST}} = 0.25$, since parallel spin pairs will recombine to triplet excitons while antiparallel spin pairs will recombine to singlet and triplet excitons. Thus, for fluorescent emitters, we find $\eta_{\mathrm{ST}} = 0.25$, which is a severe limitation of quantum efficiency of an OLED. It was shown in the pioneering work of Thompson and Forrest that this limitation can be overcome when phosphorescent emitters are used.[100−102] In the presence of strong spin−orbit coupling, the quantum mechanical selection rules are relaxed, leading to $\eta_{\mathrm{ST}}$ up to unity. Such a strong spin−orbit coupling requires a heavy metal central atom inside the fluorophore. Most commonly, iridium is chosen for this purpose, but also other heavy atoms such as Pt, Os, or Pd may be used. Emitters using both singlet and triplet excitons are called triplet emitters or phosphorescent molecules. One of the most efficient triplet emitters is the above-mentioned molecule $Ir(ppy)_3$. Kawamura showed for this molecule a PL efficiency of 97% when dissolved at 1.5% in *N*,*N*-bis(carbazolyl)-4,4′-biphenyl (CBP),[99] which is a combined effect of efficient exciton recombination and perfect use of both singlet and triplet excitons. For a deeper understanding of the mechanisms underlying the excitonic processes in triplet emitters, we refer to a review giving insight to the energetic pathways in triplet emitters.[103]

The last critical factor for an efficient OLED is the optical outcoupling efficiency, $\eta_{\mathrm{optical}}$. A simple estimation regarding the OLED as classical optics device shows that a flat device with typical refractive index of the organics layers of 1.7, deposited on ITO/glass, achieves approximately 20% outcoupling.[104] A large number of methods have been studied since to improve light outcoupling, where typically the improvement was on the order of 20−30% for highly efficient devices and up to 100% for devices of low internal efficiency. Among these methods for improving light outcoupling are, for example, the use of a resonant cavity,[105] the excitation of surface plasmons,[106] insertion of a thin layer of very low refractive index such as silica aerogel,[107] the use of periodic structures placed in the optically active layer to introduce Bragg scattering normal to the substrate plane,[108] and the addition of an organic outcoupling capping layer atop of top-emitting OLEDs.[109] Common to all these methods are unfortunately also undesirable attributes such as an angle-dependent electroluminescence (EL) spectrum and angular variations of emission intensity. Such problems are less severe or even fully circumvented by the use of rough, sand-blasted glass substrates to improve outcoupling by scattering, the use of microlenses,[110] or even millimeter-sized lenses.[111]

## 4.2. Doped Layers and Simple OLEDs Made Thereof

### *4.2.1. Influence of p-Type Doping on Carrier Injection at Contacts*

The injection of carriers at the contacts is a basic process for any LED. In first approximation, the injection of, for example, holes into organics may be carried out by matching the metal work function with the highest molecular orbital (HOMO) of the molecules within the organic layer. The same is true for the matching of metal work function and lowest unoccupied molecular level (LUMO) for electron injection. Therefore, a large work function metallic anode may be taken for hole injection. More suitable are ITO films or thin Au films. For a better matching of the work function, often also an interlayer with a HOMO between the HOMO of the hole transport layer and the work function of the anode is used. Frequently, phthalocyanines are used for this purpose, as well as thin conducting polymer layers, such as poly(3,4-ethylene dioxythiophene)/poly(styrene sulfonate) (PEDOT/PSS). While the first may cause problems due to the crystallinity of the phthalocyanine film and thus show a tendency of short circuit formation, the application of a polymeric hole injection layer requires wet-chemical processing in an otherwise vacuum-based series of processes. All this may be circumvented by the use of electrically doped molecular charge transport layers, as we will describe next.

The effect of doping on the injection behavior is demonstrated in Figure 25 for two samples based on 4,4′,4″-tris-(3-methylphenylphenylamino) triphenylamine (*m*-MTDATA), a typical hole transport material for OLEDs. As opposed to the phthalocyanines such as ZnPc or VOPc, its molecular structure favors the formation of very smooth glassy layers. Thus, it becomes possible to make interlayers of well-defined thickness and conductivity. The samples shown in Figure 25 compare two hole-transporting samples of the layer sequence ITO/*m*-MTDATA (undoped, thickness *w*)/*m*-MTDATA (p-doped with 2 mol % $F_4$-TCNQ, 100 nm)/Au. The device with doped MTDATA only ($w = 0$) acts as a good hole conductor, with nearly symmetric $j-V$ characteristics, as the energetic barrier for hole injection from ITO or Au into doped MTDATA is nearly the same. In case of the device with additional undoped MTDATA layer ($w = 50$ nm), the $j-V$ characteristics becomes asymmetric. Here, the gold top contact is generally Ohmic, while there is a considerable injection barrier for holes from ITO to *m*-MTDATA. Accordingly, devices with an undoped interlayer ($w > 0$) behave as metal−intrinsic−p-type ("M−i−p-type") diodes,[112] having a built-in field due to Fermi level adjustment between the ITO and the doped *m*-MTDATA across the undoped interlayer. While the forward currents of these diodes are only weakly affected by the thickness *w* of the undoped interlayer, currents at reverse bias increase systematically with decreasing *w*. With $w = 50$ nm, we observe a rather high rectification ratio in excess of 1000:1 at ±1 V. The barrier for hole injection from ITO into *m*-MTDATA

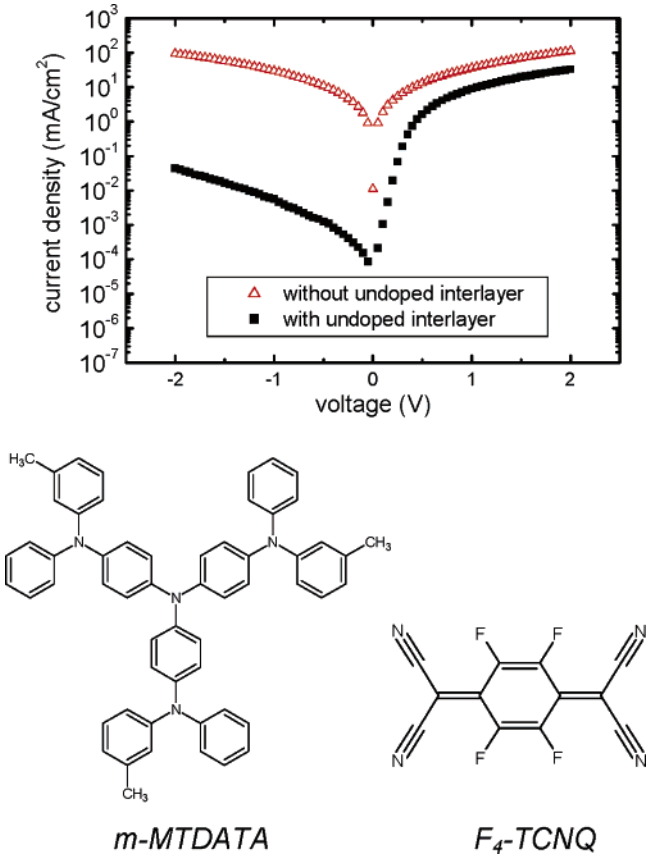


**Figure 25.** Current−voltage characteristics for junctions between ITO and p-doped *m*-MTDATA (100 nm, doped with 2 mol % $F_4$-TCNQ), with and without an interlayer of 50 nm undoped *m*-MTDATA. Gold is used as a nearly Ohmic contact to the p-doped layer.

is obviously high for untreated ITO. On the other hand, the device without an undoped interlayer has basically symmetric $I-V$ characteristics demonstrating the improved hole injection from ITO into doped *m*-MTDATA.

### 4.2.2. Simple OLEDs with Doped p-Layer

The ability to dope organic semiconductor materials with strong donor or acceptor molecules for creating a significant amount of excess charge carriers, as it was described in the previous sections, opened a completely new approach to improve OLEDs. As Blochwitz and co-workers showed in 1998,[31] OLEDs of the Tang−Van Slyke type may be improved by the use of p-type doped organic layers. They employed vanadyl phthalocyanine (VOPc) as the host and tetrafluoro-tetracyanoquinodimethane ($F_4$-TCNQ) as the dopant. The experiments showed that already a rather small concentration of $F_4$-TCNQ, well below 0.5 wt %, may lead to a significant decrease in driving voltage and, thus, to an increase in power efficiency at a given luminance. For a device consisting of glass/ITO/hole transport layer (200 nm)/$Alq_3$ (100 nm)/Al (100 nm) with various doping content of $F_4$-TCNQ in VOPc (from <0.5 to 3 wt %) as hole transport layer, it was found that with increasing doping levels, the light output started at correspondingly lower driving voltages. Today, a doping level of 2−4 wt % is established as the most suitable value for efficient devices. Furthermore, the use of vacuum gradient sublimation for purification of the organic substances beyond the purity obtained by chemical methods was a significant prerequisite for the success of this study, since also undesired chemical species may act as dopants. Gradient sublimation purification has also become a well-proven way to obtain highly efficient organic devices.[113] Still, the overall device efficiency of the OLED reported in ref 31 was rather low compared with today's devices, which can be explained by the simple device structure and by the less suitable electronic and structural properties of phthalocyanines with respect to the demands of an OLED.

It should be noted here that at the same time as the first electrically doped small molecule OLED was reported, similar experiments were carried out with polymeric materials as well, showing the same trend of decreased driving voltage and increased power efficiency.[114] Since polymeric devices are not the topic of this review, we will not discuss this in more detail.

Nowadays, molecular glasses with a HOMO around 5 eV have proven to be well-suited materials for hole transport layers in OLEDs, which is due to their ability to make smooth layers, which prevent shunts. Typical materials are triphenylamines, such as *N*,*N*′-bis(3-methylphenyl)-*N*,*N*′-diphenyl-benzidine (TPD), *N*,*N*,*N*′,*N*′-tetrakis(4-methoxyphenyl)-benzidine (MeO-TPD), and *N*,*N*′-di(naphth-1-yl)-*N*,*N*′-diphenyl-benzidine (α-NPD), or starburst-like substances, such as 4,4′,4″-tris(*N*,*N*-diphenylamino)triphenylamine (TDATA),[115] 4,4′,4″-tris(3-methylphenylphenylamino) triphenylamine (*m*-MTDATA), 4,4′,4″-tris(1-naphthylphenylamino) triphenylamine (1-TNATA), and 4,4′,4″-tris(2-naphthylphenylamino) triphenylamine (2-TNATA). For the molecular structure of such materials, see Figure 26. Many of the materials have also been used successfully as hole injection and transport layers in undoped devices; for an overview see, for example, the work of Shirota.[116]

Zhou et al.[117] studied the enhancement of hole injection and transport in OLEDs using doped hole transport layers from this group of materials. In these devices, the host TDATA was doped with $F_4$-TCNQ at different concentrations. The device structure and corresponding $j-V$ curves are shown in Figure 27. The data show that at a given voltage, the currents for the doped samples are several orders of magnitude higher than those for the undoped device. This finding is in agreement with the data from model devices, which show an improvement of the carrier injection into the transport layer. The very low currents for the undoped device are because the ITO has not been treated by oxygen plasma or ozone to increase its work function.

Figure 27a shows the luminance−voltage curves of the samples. Due to the much higher currents, the samples with doped transport layers reach higher luminance at a given voltage. Note that the doping level is not very critical both for current density and for luminance. However, the current efficiency of these devices is still very low (<1 cd/A) and even decreases with increased doping. We qualitatively explain this behavior by the formation of an interface exciplex between the TDATA HOMO and the $Alq_3$ LUMO, which leads to an inefficient, red-shifted fluorescence. Further, due to the p-doped transport layer, these interface excitons are close to a high concentration of holes, which leads to a high probability for nonradiative recombination. This causes high recombination currents in the device without generation of light at the $Alq_3$ emission wavelength. A solution to this problem is the insertion of blocking layers, as we will discuss below.

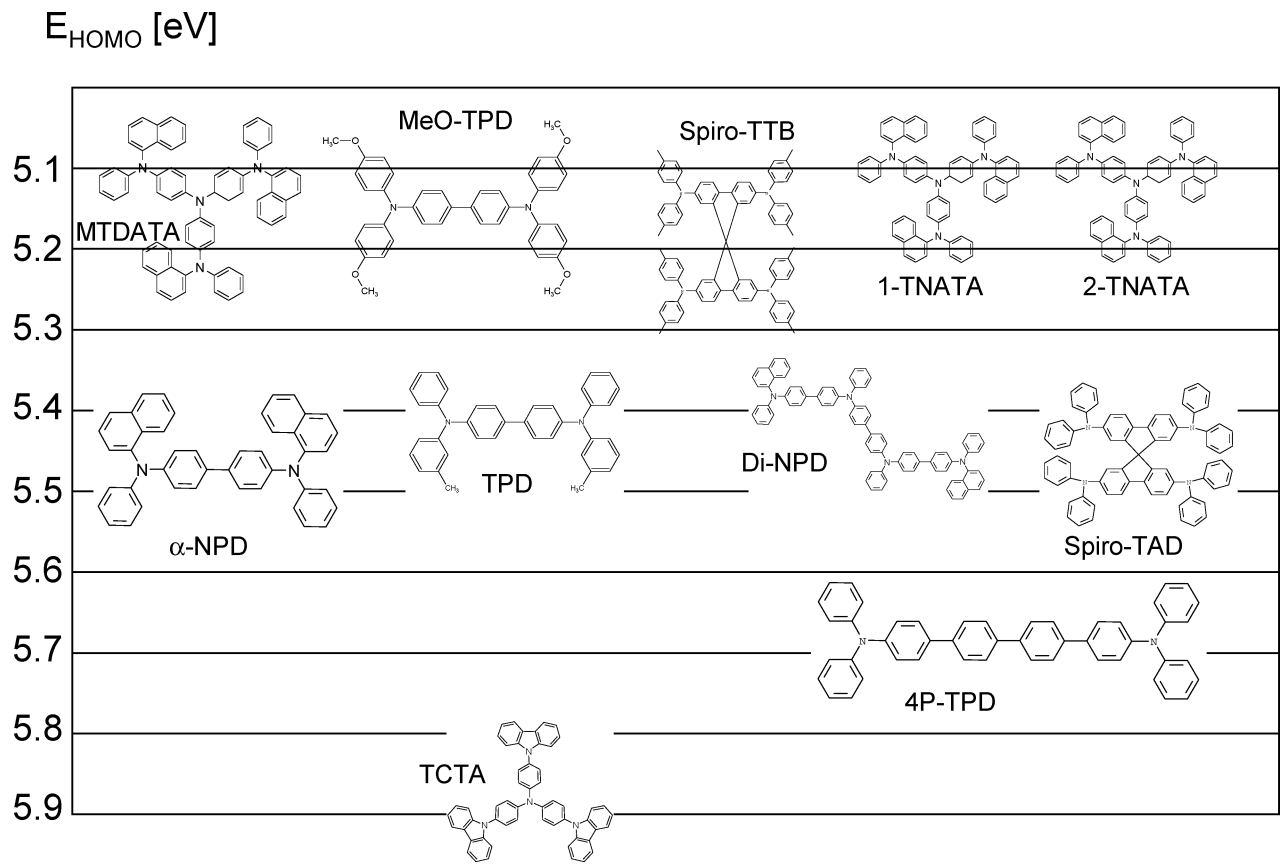


**Figure 26.** Molecular structures of typical hole transport materials with high glass transition temperature.

#### *4.2.3. Simple OLEDs with n-Doped Transport Layers*

The most common and simple OLED structure using n-type doping is the widely used electron injection system Al/LiF/$Alq_3$. Often, this system is not called a doped structure but a charge injection layer, since it is very difficult to prove the $Li^+$ ion distribution in the organic stack. As we have described earlier in this review, in the case of Al deposition onto a thin layer of LiF atop $Alq_3$, $Li^+$ ions are released such that one can really speak about doping. In a detailed study, Hung et al. showed quite nicely the influence of a 1 nm thick LiF interlayer between the organics stack of an OLED and the metal cathode.[118] The Li doping leads to an improved charge injection and transport and thus to higher current density at low operating voltage (Figure 28). The OLEDs in this work comprised the well-known stack of ITO/CuPc/NPD/$Alq_3$/(LiF)/cathode and are therefore a good reference.

### 4.3. Highly Efficient OLEDs with Doped Transport Layers

#### *4.3.1. p–i–n Devices: Monochromic OLEDs*

Combining the knowledge about p- and n-doped charge transport layers, the next step is the design of a p-type−intrinsic−n-type (p−i−n) structure, that is, an OLED with doped transport layers for both kinds of charges. The result is a three-layer OLED with an electrically intrinsic emission layer (EML) between a hole transport layer (HTL) and an electron transport layer (ETL). Although this three-layer concept works rather well, one often faces problems with lacking charge balance, interface exciplexes, or exciton quenching by excess charge carriers. For this reason, the introduction of additional blocking layers between the charge transport layers and the emission zone has been established as a concept to reach devices of high stability. This leads directly to a five-layer p−i−n OLED design, consisting of two doped transport layers, two undoped blocking layers, and an emitter layer.[32] An example for such an OLED is shown in Figure 29. Here, the hole transport layer consists of $F_4$-TCNQ-doped *m*-MTDATA, followed by an electron blocking layer of TPD, $Alq_3$ as emission layer, BPhen as hole blocking layer, and a Li-doped BPhen layer as electron transport layer. To enhance electron injection, an additional LiF interlayer has been deposited underneath the cathode. This device displays excellent current−voltage curves with exponential behavior up to current densities of a few tens of mA/cm$^2$. The luminance−voltage curve (Figure 29b) is exponential well up to a brightness of about 1000 Cd/m$^2$; 100 Cd/m$^2$ are reached at 2.55 V, which approximately corresponds to the photon energy of this green-emitting device. The peak current efficiency is more than 5 Cd/A, which is a remarkable value for bulk $Alq_3$ as emitter. For comparison, the same device has been made without n-doping. One may clearly see the significantly increased voltage to reach the same luminance as with the p−i−n device. This is caused by the insufficient electron transport in the p−i−i device.

#### *4.3.2. p–i–n OLEDs Comprising Triplet Emitters*

In collaboration between the groups of Dresden and Princeton, the p−i−n architecture has been extended to phosphorescent OLEDs. Using CBP/$Ir(ppy)_3$ as the emitter system, green electrophosphorescent OLEDs with extremely low operating voltages and high quantum efficiency were demonstrated.[119] These p−i−n-type devices attain a brightness of 1000 cd/m$^2$ at only 3 V, with an external quantum

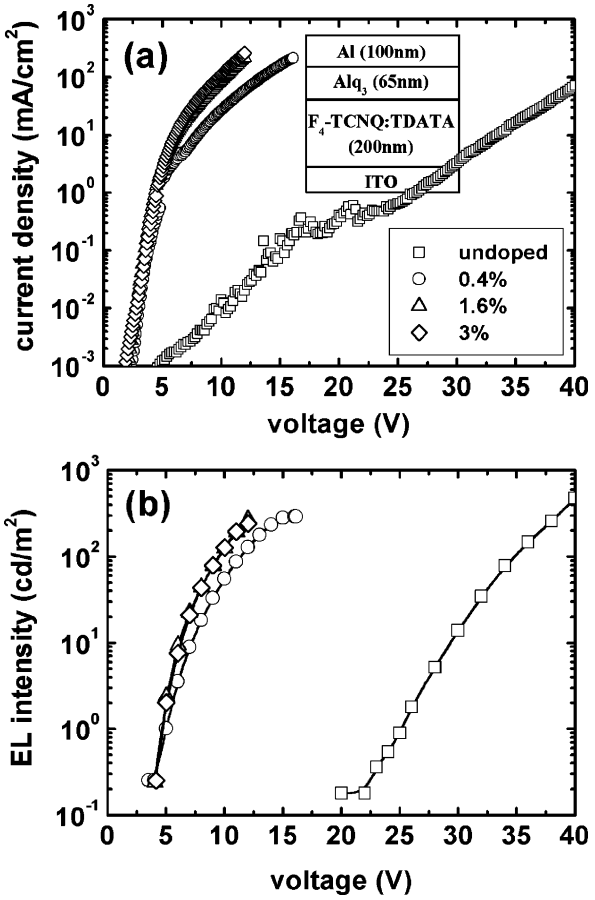


**Figure 27.** (a) Current−voltage characteristics for a series of OLEDs with the layer sequence ITO/$F_4$-TCNQ−TDATA (200 nm)/$Alq_3$ (65 nm)/LiF (1 nm)/Al and (b) luminance−voltage characteristics for the same series of OLEDs. Reprinted with permission from ref 117. Copyright 2001 Wiley-VCH.

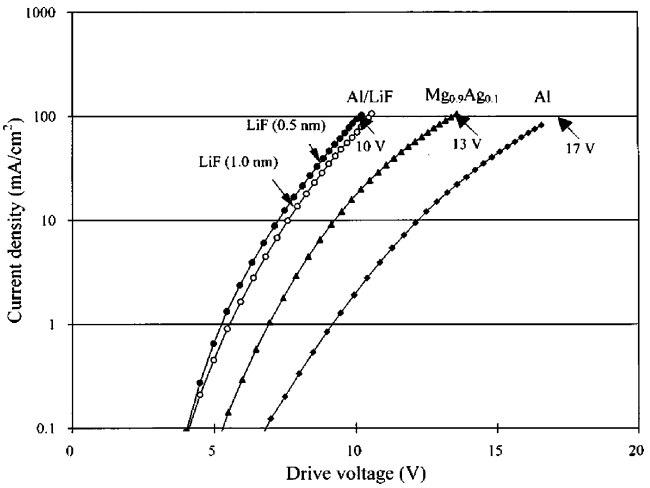


**Figure 28.** Comparison of OLEDs with $Alq_3$ as emission and hole transport layer, with and without Li doping. Reused with permission from L. S. Hung, C. W. Tang, and M. G. Mason, *Applied Physics Letters*, *70*, 152 (1997). Copyright 1997, American Institute of Physics. Note the significantly lower driving voltages needed when Li doping is employed.

efficiency of 9% and a power efficiency of 28 lm/W, see Figure 30. At 4.0 V, the devices already reach 10 000 cd/m$^2$, and the external quantum efficiency is 7% at a luminous power efficiency of 22 lm/W.

Remarkable for these OLEDs is their low driving voltage for bright electrophosphorescence: 100 cd/m$^2$ were reached

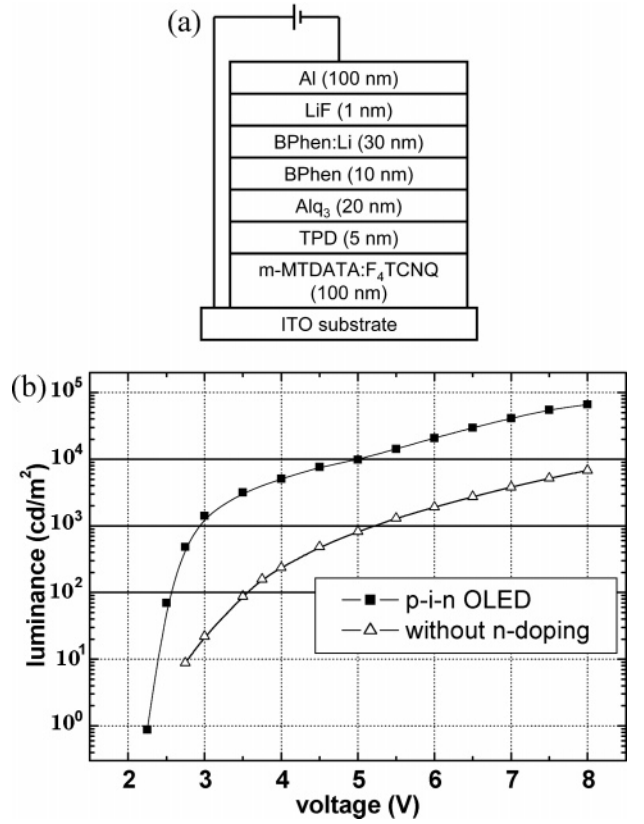


**Figure 29.** Panel (a) shows a layer stack of a p−i−n OLED with $Alq_3$ emitter. In panel (b), we show the luminance−voltage characteristics of this OLED with and without Li doping in the BPhen layer. The p−i−n doped device needs a significantly reduced driving voltage.

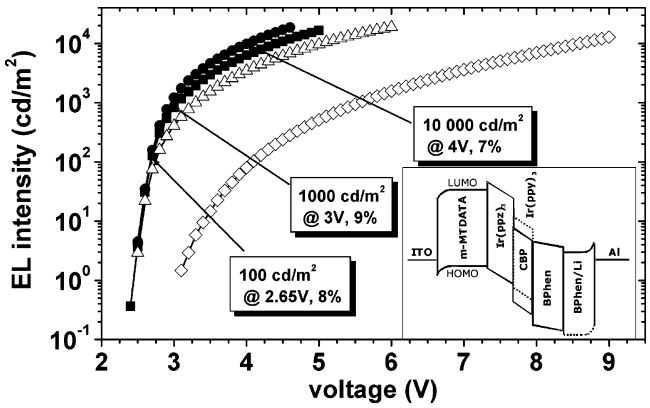


**Figure 30.** EL and efficiency data of three different p−i−n OLEDs with doped transport layers comprising triplet emitters, compared with a reference device without doped transport layers (◇). Reprinted with permission from ref 119. Copyright 2002 Wiley-VCH.

at 2.6 V, which is close to the equivalent of the photon energy (2.4 eV, corresponding to the triplet energy in $Ir(ppy)_3$). This is particularly remarkable, given that the generation of a triplet exciton from a pair of free carriers should involve a substantial energy loss. The $Ir(ppy)_3$ singlet energy is around 3 eV (estimated from the absorption edge), which implies that the energy of a free electron−hole pair, that is, the electrical gap of $Ir(ppy)_3$, is at least 3.5 eV. Therefore, one can conclude that the electroluminescence process must involve a direct generation of triplet excitons on the emitter from a pair of carriers on different molecules A and B. Only in that case the energy of the free carrier pair can be in resonance with the triplet exciton energy.

For CBP/Ir(ppy)$_3$-based devices, the process may be explained as follows: CBP has a much higher ionization energy than Ir(ppy)$_3$,[45] such that holes are injected from the HTL directly into the HOMO of neutral Ir(ppy)$_3$ molecules where they can move by hopping from dopant to dopant. On the other hand, electrons are injected from the ETL into the LUMO of CBP, the latter being lower than the LUMO of Ir(ppy)$_3$. In other words, Ir(ppy)$_3$ forms an antitrap for electrons in CBP and electrons do not enter the LUMO of neutral Ir(ppy)$_3$ molecules. However, once the Ir(ppy)$_3$ carries a hole, the LUMO is shifted downward by reduced electron−electron repulsion and the molecule becomes accessible for electrons from CBP, at least if the electron and the hole have the same spin, and the electron can directly enter the triplet state of Ir(ppy)$_3$.

Comparing doped[119] and undoped[45] OLEDs of similar device setup from different research groups, which employ the same CBP/Ir(ppy)$_3$ emitter system and appropriate charge transport and blocking layers, one finds similar quantum efficiencies in the range of 8−10% but a reduction in driving voltage by several volts using doped transport layers. Assuming the same emission spectrum and quantum efficiency, this means that the doping of the transport layers significantly increases the power efficiency.

### *4.3.3. Optimized Monochromic p–i–n OLEDs*

Electrically doped OLEDs in the three basic colors, red,[98,120] green,[121−124] and blue (RGB),[125] as well as other colors,[126] have been investigated. Some papers from industry summarize recent results of the commercial development of RGB p−i−n OLEDs.[127,128]

The p−i−n OLEDs described in the previous chapters may be improved in different ways:

(1) By using more appropriate charge blockers, the driving voltage may be reduced further, while the charge carrier balance inside the emission layer is improved. Also, the leakage of excitons or the formation of exciplexes may be suppressed further.

(2) Triplet emitters may be used exclusively for harvesting all excitons created in the emission zone. Until now, this has been realized for red and green devices, while for deep blue, an efficient and stable triplet emitter is still missing.

(3) The emission zone can be improved. By a widened emission zone with ambipolar character, the agglomeration of excitons at the interfaces to the blockers may be suppressed, leading to a lower exciton density and thus to a reduced exciton−exciton quenching. To achieve this, Zhou et al. introduced a double emission layer into the p−i−n OLED, using Ir(ppy)$_3$ as emitter.[121] This concept uses a preferably hole-transporting host on the hole injection side of the EML and a preferably electron-transporting host at the electron injection side. While Zhou used only a LiF interlayer for improved electron injection in an otherwise p−i−i-type OLED, G. He and co-workers introduced a fully doped p−i−n OLED with MeO-TPD/$F_4$-TCNQ on the hole side and BPhen/Cs for the electron side.[122,123,129] For device structure and efficiency improvement by the double emission layer (D-EML) concept, see Figure 31a. Especially for high current density/high brightness applications, the double emission layer principle is beneficial. Due to the broad local distribution of excitons, the exciton−exciton annihilation by high exciton densities is reduced. Further, the D-EML OLED reaches nearly 20% external quantum efficiency, corresponding to internal quantum efficiency close to unity.

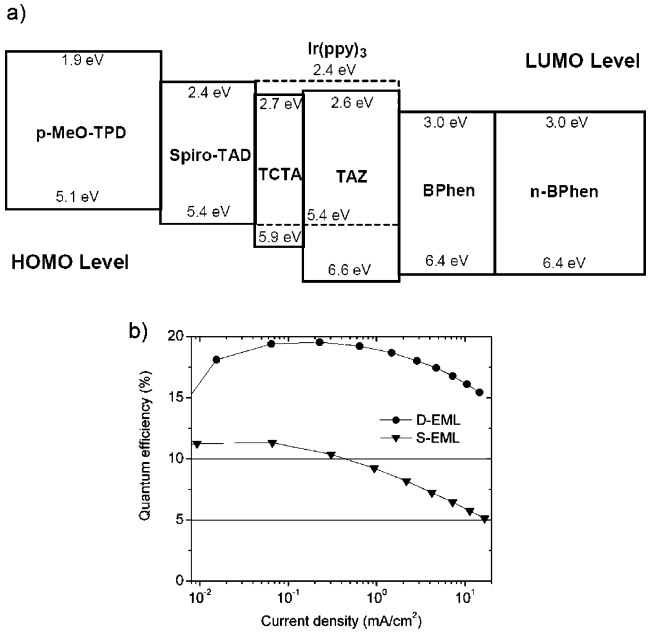


**Figure 31.** (a) Device structure of a double emission layer OLED. While the TCTA host is preferably hole transporting, 3-(4-biphenylyl)-4-phenyl-5-tert-butylphenyl-1,2,4-triazole (TAZ) conducts mainly electrons, such that a flat exciton creation profile leads to a wide emission zone. (b) Quantum efficiency data of the device shown in panel (a). Reprinted with permission from ref 129. Copyright 2004 the International Society for Optical Engineering (SPIE).

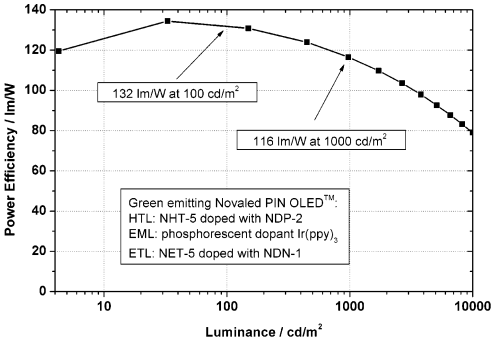


**Figure 32.** Performance data of a green bottom-emitting p−i−n OLED comprising the phosphorescent emitter Ir(ppy)$_3$ and Novaled proprietary charge carrier transport materials and dopants (p-dopant, NDP-2; n-dopant, NDN-1). At 100 cd/m$^2$, a power efficiency of more than 130 lm/W was measured. Even at 1000 cd/m$^2$, 116 lm/W is obtained, which is a remarably small efficiency roll-off. Reprinted from ref 130. Permission for Reprint, courtesy Society for Information Display.

(4) Another way to improve the p−i−n OLEDs described before is the use of more efficient and more stable dopants. For example, the evaporation temperature and the glass transition temperature of $F_4$-TCNQ is too low for applications under higher temperatures than room temperature. However, because this field was until now mainly of commercial interest and most of the improved dopants are proprietary material, we will not discuss this in detail. For interested readers, we refer to refs 127 and 128.

Novaled reported a green OLED with a p−i−n-type structure and Ir(ppy)$_3$ as emitter, reaching well above 100 lm/W, see Figure 32.[130] The device contained optimized molecular p- and n-type dopants with high stability developed by the company.

In early 2007, the group of Kido reported similarly high efficiencies of a green phosphorescent OLED, using a somewhat different approach for the charge transport layers.[131] They rely on a p-type doped polymer as hole injection layer atop the ITO comprising a TPD-like polymeric host and a molecular salt as dopant. CBP/$Ir(ppy)_3$ serves as emitter. For hole injection, they used a Li-doped electron transport layer from a new material having a very high electron mobility. The device reached 107 lm/W at 1000 cd/$m^2$ and an external quantum efficiency as high as 26%. Unfortunately, the authors did not comment on the stability of their device, which most probably may be limited by Li diffusion.

### 4.3.4. p–i–n Devices: White OLEDs

White OLEDs may be used in displays, signage, and lighting. In displays, white OLEDs may be used as liquid crystal display (LCD) backlights or for OLED displays using color filters (color-by-white). The key challenges for OLEDs in the field of lighting are high efficiency to save energy and, at the same, low cost to be competitive with existing lighting technologies.

Doped charge transport layers may be an important ingredient in OLEDs fulfilling these target applications. Doping mainly addresses the topic of high efficiency but may also be beneficial for the cost-effectiveness, since it allows the use of a broader choice of substrates. The actual work function of the substrate is of less importance in doped than in undoped devices. Therefore, also cheaper and rougher substrates may be used for OLED lighting.

Over the past few years, significant work was carried out in the field of white OLEDs, following many different approaches. Due to the high activity in this field, we will cite only a few, mainly early, works here; giving a complete list of references would require an extra review. As in all previous sections, there are competing activities for polymers and small molecules. Only the latter will be addressed here.

White OLEDs may be distinguished, for example, by the number of dyes they contain, that is, as two-[52,132−134] or three-color[132,135] based devices, or by the type of emitters used, that is, singlet emitters,[132,135,136] triplet emitters,[137−140] or a combination of both.[141−144] Further techniques, such as the exploitation of exciplexes[145,146] or down-conversion from a blue OLED by inorganic phosphors,[147] have been reported as well. A review on white OLEDs by D'Andrade summarizes the different approaches as of 2004.[148] Also for white OLEDs, the doping of transport layers is beneficial in reaching high efficiency. Still, it is amazing how few groups report on white OLEDs with doped transport layers, especially, because power efficiency is one of the key parameters of white OLED devices. The only exception is the use of a Li-doped charge injection layer, which is meanwhile rather common both for RGB and white OLEDs.[138,140,143,149−151] A paper from the Forrest group[143] shows that very high power efficiencies of white OLEDs may be achieved using the LiF interlayer doping method, with a power efficiency as high as 23.8 lm/W at 500 cd/$m^2$, a brightness relevant for white OLED applications.

Also, CsF-based injection layers have been reported, which follow the same principle of operation as the LiF-based layers.[152] Another option is the use of Li-doped bulk organic layers, made by coevaporation of Li and an organic material. Kanno reported on a two-color white OLED with a Li-doped BPhen layer as electron injection and transport layer.[153] The peculiarity of this device is the device type. They made a white top-emitting OLED with a structure Ni/NPD/$Ir(ppz)_3$/CBP−IrPQ/UGH2−$Ir(46dfppy)_3$/BPhen/BPhen−Li/ITO. This device possesses a transparent top contact and a metal substrate, a structure that may be applicable in a light fixture. In this work, the authors made a reference device without Li doping as well. The doped OLED reached 9.8 lm/W, while the undoped device only showed 3.5 lm/W in an otherwise identical setup. A comparison to a conventional bottom-emitting OLED comprising a LiF interlayer beneath the top Al contact showed that the top emission device was on par regarding power efficiency. This is remarkable, because it is known that top-emitting devices with ITO top contacts tend to show lower efficiencies, which is mainly due to sputter damages caused by top contact deposition.

In 2003, D'Andrade showed the first p- and n-doped white OLED.[139] The devices followed a layer structure of ITO/MTDATA−$F_4$-TCNQ/electron blocker/emission layer/hole blocker/BPhen−Li/Al. The devices were compared with similar ones without doped transport layers. It was found that the internal quantum efficiency was higher for the undoped devices due to lower charge leakage to the undesired direction. In contrast, the lower driving voltage for the doped devices lead to a power efficiency equal to the one found for the undoped devices (11 lm/W). This means that the lower drive voltage was just compensating the losses caused by charge leakage. On the other hand, if one may further improve the charge and exciton blocking behavior of the electron and hole blocking layers, we expect that the doped devices should give higher power efficiency.

Very recently, Schwartz et al.[142,144] showed efficient white p−i−n OLEDs, comprising a quite complex emitter system of red and green triplet emitters combined with a blue singlet emitter. The peculiarity of this system is an exciton blocking interlayer between the blue singlet and red/green triplet emitting zones, which prevents triplet exciton quenching of the excitons created in the triplet emitter zone by the lower lying, nonradiative triplet gap of the blue singlet emitter. The resulting layer structure is the following: ITO/MeO-TPD−$F_4$-TCNQ/spiro-TAD/NPD−iridium(III)bis(2-methyldibenzo-[f,h]quinoxaline)(acelylacetonate)/TCTA−$Ir(ppy)_3$/TCTA−2,2′,2″(1,3,5-benzenetriyl)tris-(1-phenyl-1H-benzimidazole)/2,2′,7,7′-tetrakis(2,2′-diphenylyinyl)spiro-9,9′-bifluorene/BPhen/BPhen−Cs/Al.

The device characteristics of two different sample series following this white p−i−n OLED concept are shown in Figure 33a,b. Depending on the layer thickness of the green emission layer and the triplet exciton blocking interlayer between the blue and the green emission layers, different color points may be chosen (e.g., warm white standard illuminant A at CIE-1931 color coordinates of (0.44; 0.40) or cold white point E of equal energy with color coordinates of (0.33; 0.33)). The emission color determines significantly also the power efficiency of the device, see Figure 33. The cold white sample (circles) reaches 8.8 lm/W at 100 cd/$m^2$, while the warm white device reaches 17.4 lm/W.

### 4.3.5. Stability Issues of OLEDs with Doped Charge-Transport Layers

A very important issue for the relevance of a doping technology is the question of stability and lifetime. It is directly connected with the question under which circumstances dopants may diffuse in the device and what damage occurs to the device by dopant diffusion. In the section on

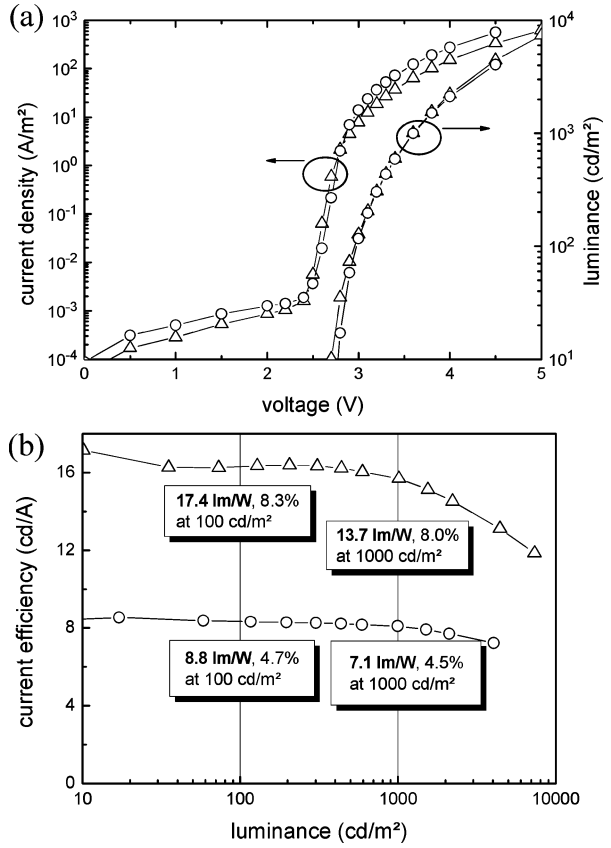


**Figure 33.** (a) Current−voltage and luminance−voltage curves for a white p−i−n OLED. A brightness of 1000 cd/m$^2$ is reached below 4 V. (b) Power efficiencies reached by white p−i−n OLEDs. Reused with permission from Gregor Schwarz, Karsten Fehse, Martin Pfeiffer, Karsten Walzer, and Karl Leo, *Applied Physics Letters*, *89*, 083509 (2006). Copyright 2006, American Institute of Physics.

Li doping, we already mentioned that the induced Li diffusion takes place upon metal deposition onto it. Thus, Li is a rather volatile material inside the OLED stack, such that special care must be taken when it is used. Further, applications that require storage or operation temperatures above room temperature are not appropriate for Li-doped devices. Another topic is the low glass transition and evaporation temperatures of typical dopants, such as $F_4$-TCNQ. For this reason, D'Andrade studied the operational stability of green phosphorescent OLEDs with CBP/Ir(ppy)$_3$ as emission layer with and without p−i−n-doped structure.[154] They used $F_4$-TCNQ-doped MTDATA and Li-doped BPhen−BAlq (BAlq = aluminum(III) bis(2-methyl-8-quinolinate)-4-phenylphenolate) as doped charge transport layers and as undoped charge transport layers CuPc/NPD for the p-side and BPhen−BAlq/BPhen/Li for the n-side. In this work, OLED lifetimes of 18 000 h for the doped and 60 000h for the undoped device were reported, both extrapolated to 100 cd/m$^2$. Compared with the undoped device, the Li-doped device had a significantly reduced lifetime. Using Cs for this purpose can overcome the problem, as we will show next.

Recently, Meerheim et al. proved that doped OLEDs with very high stability are possible.[120] In red OLEDs containing MeO-TPD/$F_4$-TCNQ as hole and BPhen/Cs as electron transporter, it could be shown that the lifetime limitation came mostly from the choice of emitter host and charge blockers, instead of from the electrically doped transport layers. The most stable devices in this study reached extrapolated lifetimes of several million hours when driven

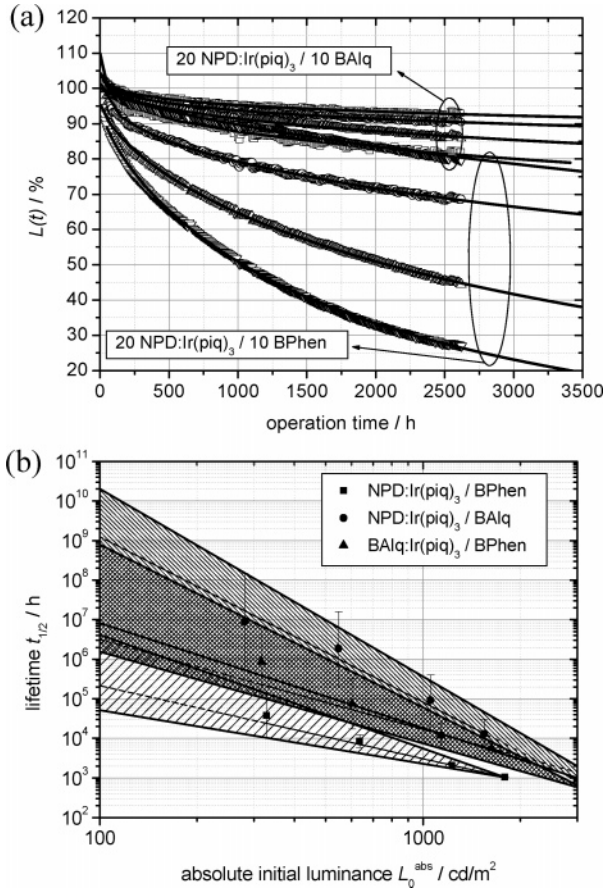


**Figure 34.** (a) Lifetime of red NPD/Ir(piq)$_3$ (piq = 1-(phenyl)-isoquinoline) p−i−n OLEDs with different hole blockers at different current densities (5, 10, 20, or 30 mA/cm$^2$), referring to different initial luminance. By exchanging the hole blocker to BAlq, a considerable stability enhancement is obtained. (b) Lifetime extrapolation for the OLEDs shown in panel a using the stretched exponential decay model. For 100 cd/m$^2$, we reach extrapolated lifetimes well above one million hours for different red devices. Reused with permission from Rico Meerheim, Karsten Walzer, Martin Pfeiffer, and Karl Leo, *Applied Physics Letters*, *89*, 061111 (2006). Copyright 2006, American Institute of Physics.

at 100 cd/m$^2$ at room temperature, see Figure 34. The higher stability as compared with the samples of ref 154 is explained by the significantly lower mobility of Cs as compared with Li due to its larger size, which prevents destruction of the emission layer, and the use of very stable materials for the emitter and blocker system.

A further step to go is the stabilization against heat. All dopants discussed so far will not allow operation under elevated temperatures. However, Novaled developed its p-dopant NDP-2,[127] which has significantly higher glass transition and evaporation temperatures than conventional p-dopants like $F_4$-TCNQ. In a recent study, it was shown that high-temperature stability can be obtained even for a molecularly doped electron transport system.[130] In this material system, both the glass transition temperature of the host and that of the dopant are significantly increased. Such an electron transport system could be driven up to temperatures of 160 °C without losing its electrical properties.

## 4.4. Top-Emitting and Transparent OLEDs

### *4.4.1. Top-Emitting OLEDs*

Standard OLED structures emit through the transparent substrate. However, for many applications, it would be useful

**Table 5. Lifetime Overview of Top-Emitting p−i−n OLEDs Forming a RGB System as Reported by Novaled in 2005[127]**

| | color coordinates CIE-1931 | lifetime |
|---|---|---|
| phosphorescent green p−i−n | 0.28/0.64 | 13000 h @ 500 cd/m$^2$ |
| phosphorescent red p−i−n | 0.69/0.31 | 30000 h @ 500 cd/m$^2$ |
| fluorescent blue p−i−n | 0.15/0.24 | 5000 h @ 500 cd/m$^2$ |

if the emission was away from the substrate (top emitters). In principle, this can be achieved with a transparent cathode. This is most relevant for active matrix displays, where the active matrix control electronics is opaque and therefore requires a top emission OLED setup. For this reason, top-emitting OLEDs have been recently studied by many researchers, both as conventional, undoped OLEDs and as doped p−i−n OLEDs, with the latter now reaching similar values of efficiency and lifetime as for bottom-emitting devices.[67,127] One of the main challenges of top-emitting OLEDs in general is the damage-free deposition of a transparent top contact onto the OLED stack. Two main paths have been followed to solve this problem: the sputter deposition of ITO onto the organics and the deposition of very thin, and thus transparent, metal contacts.

The use of doped charge transport layers is beneficial for both kinds of contacts. One reason is the wider choice of contact materials, since the work function of the top contact does not need to match the energy levels of the organics as precisely. This opens the way to select contact materials with respect to their optical and charge transport properties.

On the other hand, thick charge transport layers may act as sacrificial layer for ITO sputter deposition, such that the sensitive emitter−blocker system of the OLED remains undisturbed by sputtering. Meanwhile, top-emitting p−i−n OLEDs are well established and are beginning to show technologically relevant lifetimes as well, see Table 5. As Kanno et al. showed, top-emitting white p−i−n OLEDs can be made as well.[153] In case of white emission, it is not the underlying driver electronics that makes top-emitting devices interesting but the fact that untransparent substrates less expensive than glass may be used.

A very promising aspect of doped OLEDs, especially for top-emitting devices with their strong microcavity effects, is the opportunity to select thicknesses for the charge transport layers that allow for resonant light outcoupling. To achieve this, an optimized layer thickness for both the hole and the electron transport layers must be found. Further, we showed that an additional light outcoupling layer may improve the light extraction from a top-emitting OLED.[155] Combining this finding with optimized layer thicknesses, one could enhance the transmittance of the top contact, leading to top-emitting OLEDs with 78 cd/A current efficiency (see Figure 35). This was only possible by using the p−i−n approach, which allowed for layer thickness optimization and at the same time the choice of an optically matching top metal contact, independent of its work function.

In a recent series of papers, the group of Wu from Taiwan reported on outcoupling efficiency enhancements, which became possible by tuning the optical microcavity with help of electrically doped transport layers.[156,157] They used the established materials, $F_4$-TCNQ/MTDATA and BPhen/Cs, for enhancing the light outcoupling by microoptics optimization and made stacked tandem OLEDs with optimized microcavity. As a stacked microcavity device, a green tandem OLED with 200 cd/A and 10 V operation voltage for 1000 cd/m$^2$ was demonstrated, underlining the high device efficiency that may be reached by doped devices.[157]

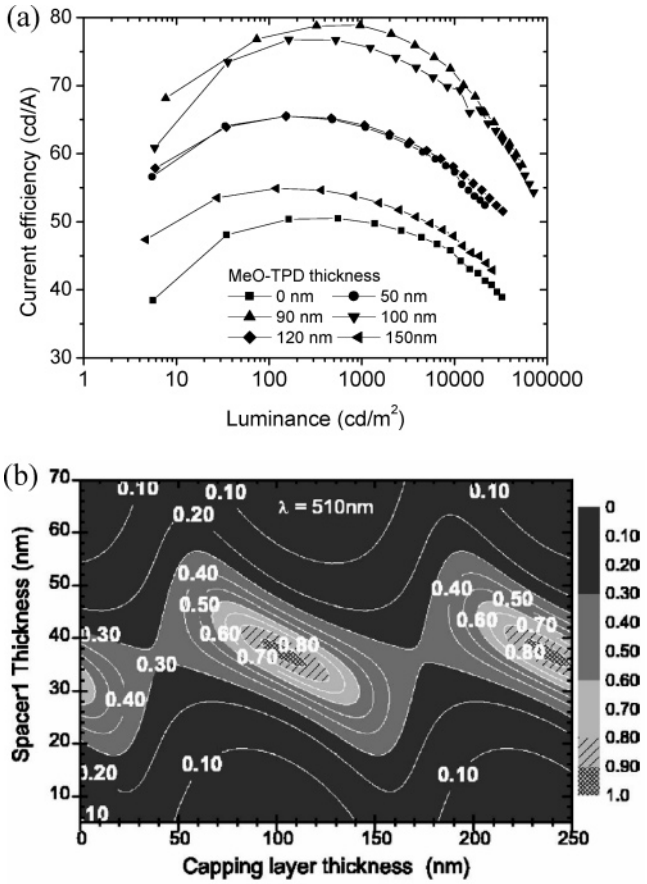


**Figure 35.** (a) Dependence of the external current efficiency of a top-emitting green p−i−n OLED on the thickness of the doped hole transport layer and (b) model calculation for the dependence of light transmission through the top contact on the thickness of electron transport layer and light outcoupling layer. Reused with permission from Qiang Huang, Karsten Walzer, Martin Pfeiffer, Vadim Lyssenko, Gufeng He, and Karl Leo, *Applied Physics Letters*, *88*, 113515 (2006). Copyright 2006, American Institute of Physics.

### 4.4.2. Transparent OLEDs

Transparent OLEDs with doped charge transport layers were demonstrated for the first time in 2002.[33] The model devices were inverted top emitters deposited on ITO as cathode using semitransparent gold as anode. Both voltage and quantum efficiency were comparable to a substrate emitting device. The low voltage drop over the doped charge transport layers allows the use of rather thick layers, which may protect the rest of the OLED against sputter damages from the ITO deposition. Using this approach, Pfeiffer et al.[158] reported a fully transparent and metal-free OLED, comprising a p−i−n OLED between two ITO layers (see Figure 36). As usual for doped devices, high luminance is reached at low driving voltage; for example, 100 cd/m$^2$ are reached at 3 V. Further, the device achieved a peak power efficiency of 23 lm/W at a remarkably high brightness of 500 cd/m$^2$, whereas most conventional undoped OLEDs reach their peak efficiencies well below 1 cd/m$^2$.

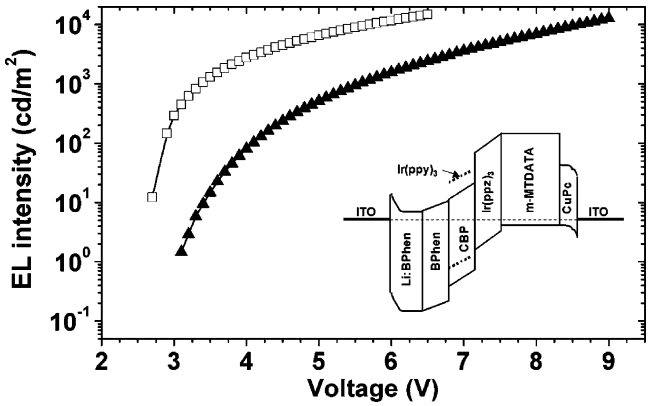


**Figure 36.** Electroluminescence (EL) intensity versus applied voltage for CBP/Ir(ppy)$_3$ based electrophosphorescent OLEDs: (□) transparent n−i−p OLED measured as the sum of the light emitted through the top and bottom contacts; (▲) conventional bottom emission OLED reference sample with undoped transport layers and a reflecting top contact. The inset shows a proposed equilibrium energy level diagram of the inverted transparent n−i−p OLED.

## 4.5. Application Examples

### *4.5.1. Example I: Doped p–i–n OLED on Low-Cost Substrates*

For the yield of an OLED manufacturing process, an important benefit of the doping technique is the fact that the thickness of the doped transport layers does not significantly influence the operation voltages. Since the voltage drop over the doped transport layers is small, a small fluctuation of organic layer thickness, for example, due to a rough substrate, does not significantly influence the electrical properties of the OLED. Thus, doped transport layers are very reproducible because the performance is less dependent on the actual state and uniformity of the substrate surface. This makes p−i−n OLEDs very promising for the integration with low-cost substrates of a certain roughness. More important than the roughness are the sealing properties of the substrate against water and gas penetration, such that metal substrates may be used without special gas barrier layers, while plastic substrates will require an elaborate gas barrier system. Thus, metal substrates may be a promising alternative to the glass−ITO system.

Further issues regarding replacement of ITO as a conductive transparent electrode need to be addressed, since ITO has become a very costly electrode due to a severe increase of the indium price on the world market: from 2002 to 2005, there has been an increase by a factor of 10 due to the increased demand of the flat panel display industry. For p−i−n-type OLEDs, the replacement of ITO by the highly conductive polymer PEDOT/PSS is possible.[159,160] Indeed, a special high-conductivity grade PEDOT could be even used to make OLEDs with superior performance. The significantly lower refractive index of the polymer as compared with ITO leads to improved light outcoupling, which may compensate the electrical losses. The highest conductivities possible so far for PEDOT/PSS layers are 500 S/cm, which is an order of magnitude less than that in standard ITO (6000 S/cm). In Figure 37, we compare two green p−i−n OLEDs of identical setup, but on different anodes. Due to the improved light outcoupling, the device on PEDOT/PSS reaches even higher efficiency than the one on ITO. Similar results were found also for blue and red devices.[160] However, because of the stronger absorption of PEDOT/PSS in the red, the efficiency

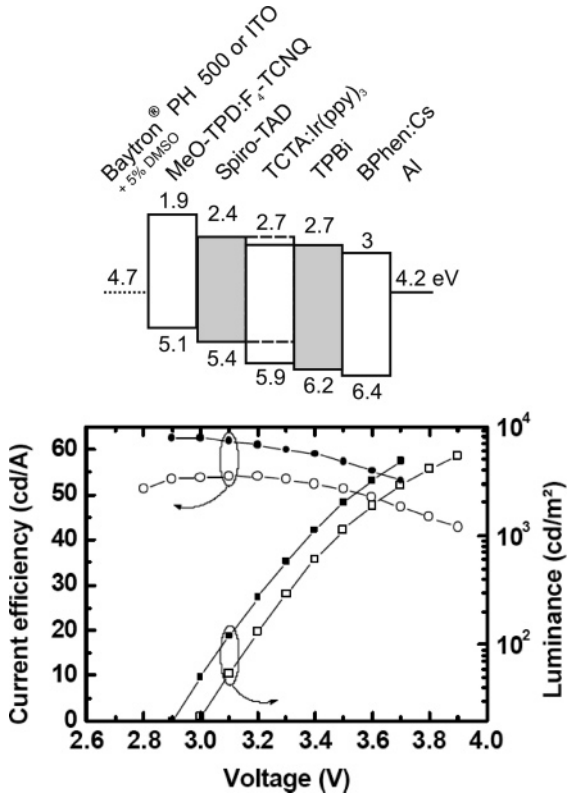


**Figure 37.** Performance of a green OLED, based on the triplet emitter Ir(ppy)$_3$, with an anode made of ITO (○,□) and PEDOT/PSS (●,■). Reprinted with permission from ref 159. Copyright 2006 the International Society for Optical Engineering (SPIE). Note that the device with the polymeric anode is improved both with respect to driving voltage and efficiency, as compared with the "standard" device on ITO. This is due to improved light outcoupling caused by the lower refractive index of PEDOT/PSS as compared with ITO. For details, see ref 160.

is only increased for blue and green devices, while for red it remains nearly unchanged when changing the anode.

### *4.5.2. Example II: Doped OLED for Silicon Microdisplays*

Another OLED application is microdisplays on silicon substrates. By combining silicon active matrix (AM) driver electronics and highly efficient p−i−n OLEDs, the group at Fraunhofer IPMS reported recently an active matrix p−i−n OLED microdisplay, see Figure 38.[161] The device needs a driving voltage of 3.2 V to reach a luminance of 100 cd/m$^2$, which is well compatible with complementary metal-oxide-semiconductor (CMOS) technology. Since microdisplays are used in near-eye applications, the typical operating luminance is 70 cd/m$^2$, which can be reached easily by this device.

### *4.5.3. Stacked OLEDs*

Doping may further be used for efficiently stacking OLEDs (Figure 39). The doped charge transport layers are by several means beneficial for stacked devices. First, they allow putting the emission layers at such positions where they may lead to improved light outcoupling by the optical mircoresonator effect. In this case, the doping leads only to low voltage losses when the thickness of the charge transport layers is increased. Second, it is possible to directly stack an ETL and a HTL on top of each other, which acts as charge converter. Following these ideas and incorporating a stack as reported by He,[123] Cho et al. showed stacked green OLEDs with up to 200 cd/A.[162]

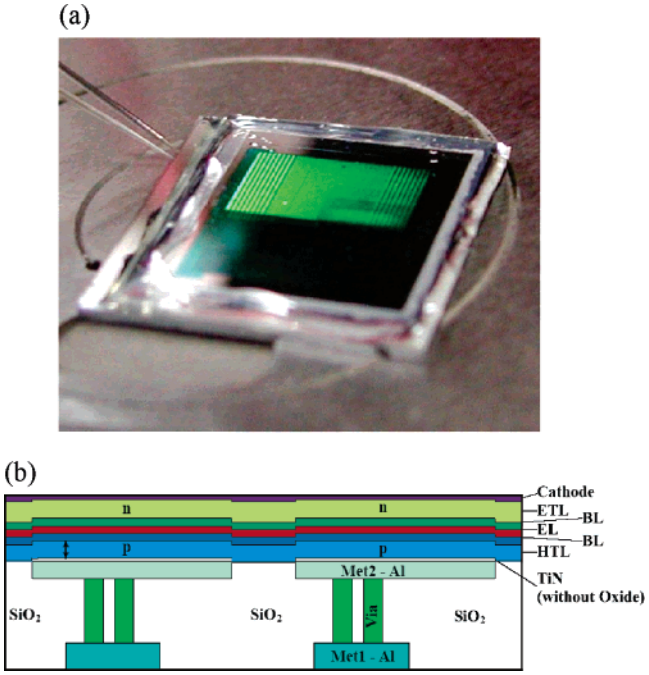


**Figure 38.** (a) Photograph of a green-emitting AM−p−i−n OLED microdisplay test chip with screen diagonal of 0.7 in. and a chip size of 0.85 × 0.85 in.$^2$ and (b) p−i−n OLED layer stack and interface to the CMOS substrate of the microdisplay test structure with TiN Al electrodes. Reprinted from ref 161. Permission for Reprint, courtesy Society for Information Display.

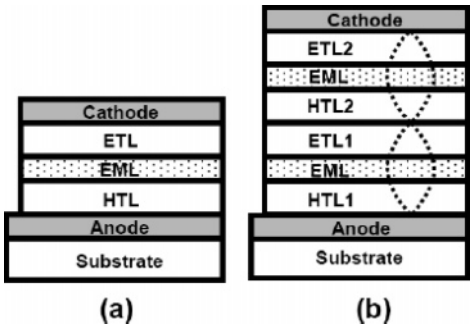


**Figure 39.** Standard OLED (a) and stacked OLED (b) in comparison. Doped charge transport layers allow putting the emission layers to optically beneficial positions within the microcavity formed from anode and cathode. Reused with permission from Ting-Yi Cho, Chun-Liang Lin, and Chung-Chih Wu, *Applied Physics Letters, 88*, 111106 (2006). Copyright 2006, American Institute of Physics.

## 4.6. Summary: OLEDs with Doped Transport Layers

Since its introduction in the late 1990s, the field of OLEDs with doped charge transport layers has undergone a significant development. It has been shown that doped transport layers can lead to superior power efficiency, regardless of the detailed structure of color of the OLED device. While devices without a complete p−i−n structure have shown very high efficiencies as well by using very thin transport layers,[163] the advantages of doped transport layers are obvious. The devices with the highest power efficiencies reported so far rely on a p−i−n-type structure.[131,130] Since power efficiency is the key for many applications, such as mobile devices, energy saving lighting technology, or environmentally friendly TV screens, the route of implementing doping technology into the transport layers of OLEDs will help the OLED technology to its technological breakthrough.

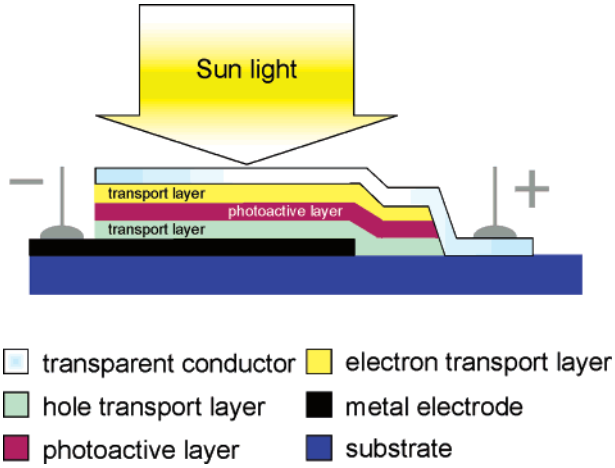


**Figure 40.** Basic layer sequence of an organic solar cell.

Finally, we want to mention that we have tried to summarize the most important results. There are still many more papers in the literature that cannot be discussed here due to lack of space.[126,164−168]

# 5. Organic Solar Cells with Doped Transport Layers

## 5.1. Introduction: Basics of Organic Solar Cells

Organic solar cells are a promising way toward large-area and low-price photovoltaic systems. The main advantages are the easy preparation, the low process temperatures, the low-cost materials and processing technology, and the possibility of producing flexible devices on plastic substrates. Organic solar cells are made of thin layers of organic materials with thickness in the 100 nm range (i.e., only about one tenth of a gram of organic material is needed for a square meter of solar cell). Such solar cells with acceptable power efficiency were first prepared by Tang at the Kodak Research Laboratories in 1986.[8] The motivation for using organic dyes is to replace the expensive silicon in conventional photovoltaics and to apply simple production techniques. Additionally, organic solar cells can be prepared on plastic foil and are ideal candidates for flexible and portable systems.

In Figure 40, the principle architecture of an organic solar cell is shown. Organic solar cells basically comprise the following layers: cathode, electron transport layer, photoactive layer, hole transport layer, and anode. In general, a solar cell absorbs light, separates the created electrons and holes from each other, and delivers the electrical power at the contacts.

There is a fundamental difference between the working principle of organic and inorganic solar cells. In a silicon solar cell, the light directly generates free charge carriers. In organic materials, the light absorption is followed by the creation of excitons. Excitons are quasi-particles consisting of an electron and a hole that attract each other through Coulomb interaction. The binding energy of these excitons is typically 0.2−0.5 eV.[19] Because the necessary electric field strength ($>10^6$ V/cm) to overcome this binding energy is not available in organic solar cells, excitons are normally separated at the interface between two different organic layers (heterojunction). As shown in Figure 41, the energy alignment of these two materials has to be optimized so that on one hand the excitons are efficiently separated but on the other hand no excess energy is lost in this process.

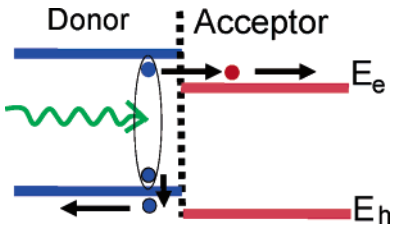


**Figure 41.** Exciton separation between two different organic materials with suitable charge carrier energy levels.

Nowadays, all efficient organic solar cells are based on the exciton separation at an interfacial heterojunction or a bulk heterojunction (mixed layer).

Three different types of organic solar cells are known. The organic semiconducting material can be comprised of either so-called small molecules (SM solar cells) or polymers (polymer solar cells).[169−172] A third type of organic solar cells is called the dye-sensitized solar cell (also called the Grätzel cell), which contains a highly porous layer of titanium dioxide as the electron transport layer.[173] Small molecule solar cells are processed in vacuum by physical vapor deposition, whereas polymer solar cells are processed by spin-coating or ink-jet printing (vacuum deposition is still necessary for metal deposition). Grätzel cells are processed by printing of titanium dioxide with subsequent sintering and dying. In this review, we concentrate on small molecule solar cells.

### *5.1.1. Short History of Small Molecule Solar Cells*

The first organic solar cells consisted of simple Schottky diodes.[174] In these structures, only a single organic layer was located between the metal electrodes.[175−177] The devices mainly suffered from inefficient charge carrier generation, and the achieved power efficiencies were below 0.1%.[174,178,179]

The general problem of using Schottky diodes is that the charge generation is efficient neither in the bulk nor at the interface to the metals, because at the metal contacts the charge carriers are not only separated but also efficiently quenched. In 1986, Tang reached a breakthrough in the efficiency of organic solar cells.[8] The cells were composed of a bilayer of a perylene derivative and a phthalocyanine and reached a power efficiency of around 1%. The advantage compared with Schottky diodes is that organic heterojunctions create efficient interfaces for charge separation. However, the small exciton diffusion length in organic polycrystalline and amorphous layers remains as a problem.

Solar cells consisting of polymer/polymer bilayers,[180,181] of polymer mixed layers,[182] and of polymer/fullerene bilayers were also investigated.[183] In 1995, Yu et al. published results about an organic solar cell containing a polymer/fullerene mixed layer as the photoactive region.[184] The breakthrough for polymer solar cells appeared in the year 2001.[169,170,171] Shaheen et al. reached a power efficiency of 2.5% using a mixed layer (following the bulk heterojunction concept) of the polymer MDMO-PPV (poly(2-methoxy-5-(3,7-dimethyl-octyloxy)-1,4-phenylene vinylene)) and the fullerene derivative PCBM (1-(3-methoxycarbonyl)-propyl-1-1-phenyl-(6,6)-$C_{61}$). A further increase of the efficiency of polymer solar cells was obtained by a postproduction treatment (heating and simultaneous applying voltage) of the devices.[172] The best polymer devices were presented by Heeger et al. and contained the polymer P3HT (poly(3-hexylthiophene))[185] reaching a power efficiency of 5%. Model calculations show that a further increase of the power efficiencies of polymer solar cells is possible.[186]

For organic solar cells consisting of small molecules, the bulk heterojunction concept was also successfully applied.[187−190] In 2000, Meissner et al. showed that by using a mixed layer of a fullerene ($C_{60}$) and a phthalocyanine (ZnPc), power efficiencies of 1% can be reached.[191] In this cell, the photoactive mixed layer was embedded between a phthalocyanine layer on one side and a perylene derivative on the other side. Additionally to the bulk heterojunction concept, small molecule solar cells containing bilayers were developed.[192,193] A high power efficiency of 3.6% was reached by Peumans et al. using a bilayer of a fullerene ($C_{60}$) and again a phthalocyanine (CuPc).[194,195] These cells contain an additional thin layer of neat BCP below the metal contact. The BCP layer acts as a very efficient exciton blocking layer. The first organic tandem cells were presented from Hiramoto et al. in 1990.[196] Hiramoto used a thin gold interstitial layer as recombination zone in the tandem cells. In 2004, Forrest et al. presented a small molecule tandem solar cell with the highest efficiency up to now of 5.7%, using a combination of a bilayer and bulk heterojunction structure with the materials CuPc and $C_{60}$.[197,198]

The first organic solar cells with doped layers contained small molecules like $O_2$ and $Br_2$ as dopants.[199,200] However, this causes problems since these small molecules rapidly diffuse through organic films.[192,201,202] In 2000, Pfeiffer et al. presented an organic solar cell containing a transport layer that was doped with a larger molecule, namely, the strong acceptor molecule $F_4$-TCNQ (tetrafluoro-tetracyanoquinodimethane).[35] By using a doped transport layer, the series resistance of the device was significantly lowered and the photocurrent was increased. This solar cell contained a p−i−i structure and was the first step toward an organic p−i−n structure containing a photoactive intrinsic region embedded between a p- and a n-doped transport layer. In 2004/2005, Maennig et al. demonstrated the p−i−n concept with controlled doping in more detail and showed that the power efficiency of the devices can be strongly increased by using doped wide-gap transport layers.[76,203] The best organic solar cell currently[197] with a 5.7% efficiency contains a wide-gap transport layer (*m*-MTDATA) doped with $F_4$-TCNQ.

## 5.2. Organic p–i–n Solar Cells

### *5.2.1. Basic Concept of Organic p–i–n Solar Cells with Doped Wide-Gap Transport Materials*

Most non-polymeric organic solar cells are based on a heterojunction between two highly light-absorbing materials. This heterojunction is needed to separate the excitons, which are rather strongly bound in organic semiconductors. Due to the small diffusion lengths in most of the organic semiconductors, the photoactive region of such cells is only a narrow layer at both sides of the hetero interface. However, the cells have to be much thicker than the active region to avoid shorts and recombination at the metallic contacts; that is, there are strongly absorbing regions that do not contribute to the photocurrent.

One concept is to replace these regions by transparent materials (wide-gap transport materials, see Figure 42). The layer sequence is therefore electrode, transparent layer, photoactive layer(s), second transparent layer, and electrode. The benefit of this concept is that the solar cells only absorb the light in the photoactive region and achieve very high

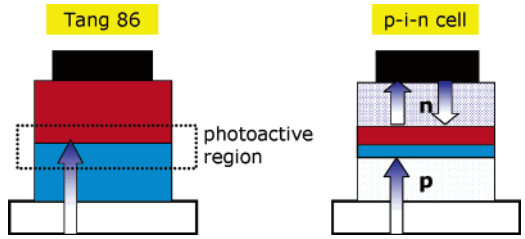


**Figure 42.** Comparison of the heterojunction solar cell first introduced by C. Tang in 1986 and the p−i−n solar cell structure with wide-gap transport materials. The arrows indicate incoming and reflected light.

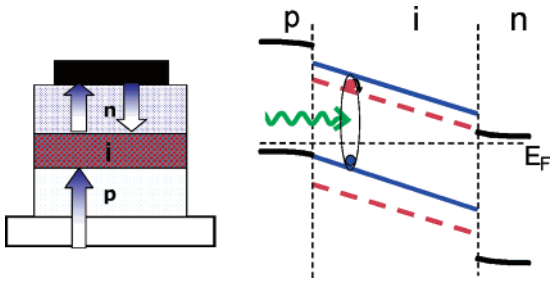


**Figure 43.** Schematic illustration and energy diagram of an ideal p−i−n solar cell containing a bulk heterojunction as photoactive region.

internal quantum efficiencies. The latter fact is crucial for preparing stacked cells (see below).

The second key technology for the organic p−i−n solar cell concept is the controlled doping of the wide-gap transport layers. In the first part of this review, we have shown that stable and reproducible doping in organic systems is possible and leads to comparatively high conductivities. For example, when matrix materials such as $C_{60}$ or MeO-TPD are used, conductivity values of higher than $10^{-5}$ S/cm are reached, which is already high enough to make Ohmic losses in doped transport layers of organic solar cells negligibly small.

Figure 43 shows the energy diagram of the p−i−n concept. Displayed is an ideal p−i−n-heterostructure for an organic solar cell. In such a cell, only the intrinsic layer absorbs visible light. This layer can be a bilayer of two highly absorbing materials or a bulk heterojunction (blended layer). The p- and n-layers are realized by doped wide-gap materials. The interfaces at the photoactive layers play an essential role in this concept. The transition of photogenerated charge carriers from the photoactive region to the respective transport layer must be barrier-free, and it should take place without loss in free energy. A good energy level alignment is necessary to achieve this goal including the challenge to find suitable materials. Additionally, the injection of photogenerated carriers into the transport layers as minority carriers should be suppressed by high barriers. Thus, the interfaces act as membranes allowing only the "correct" type of charge carriers to pass and to leave the photoactive layer.

A major benefit of doped wide-gap materials is the freedom to optimize the cells in terms of thin-film optics (see Figure 44). The cells do not suffer losses by parasitic absorption when the incident light passes the first organic layer toward the photoactive region. Furthermore, the light reflected at the back contact can be efficiently used. The thickness of the photoactive layer can be varied so that a high internal efficiency can easily be reached. Varying the thicknesses of the wide-gap layers allows the placement of the photoactive layer at the maximum of the optical field

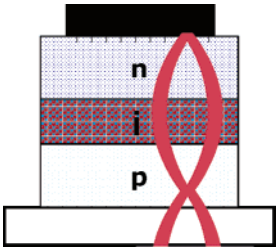


**Figure 44.** Schematic illustration of the optical field distribution within the device. The photoactive layer is placed at the maximum of the light intensity.

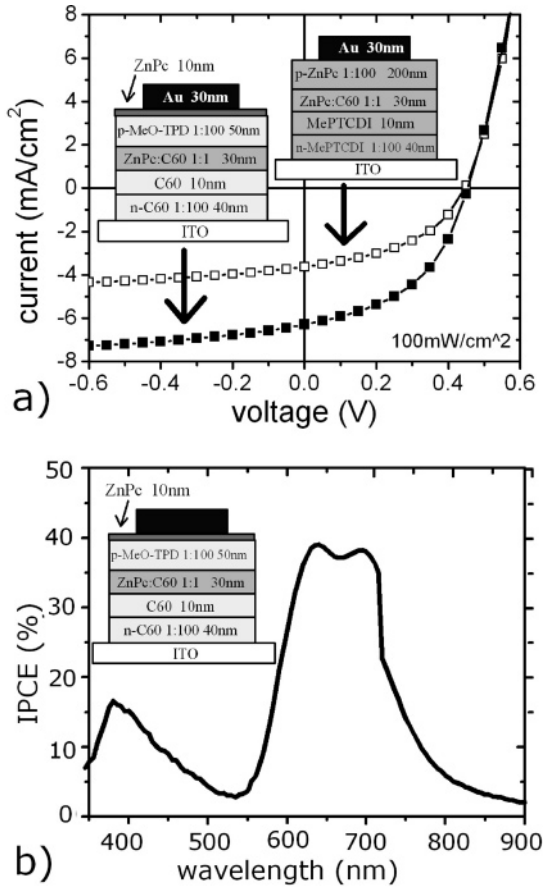


**Figure 45.** (a) Current−voltage characteristics of two p−i−n solar cells with the same active layer (ZnPc/$C_{60}$, 1:1, 30 nm) either with wide-gap transport layers (n-doped $C_{60}$ and p-doped MeO-TPD) or with low-gap transport layers (n-doped Me-PTCDI and p-doped ZnPc). By using wide-gap layers, the short circuit current is increased from 3.7 to 6.1 mA/cm$^2$ compared with the low-gap cell. (b) External quantum efficiency of the wide-gap cell. Reprinted from ref 76, Copyright 2004, with kind permission of Springer Science and Business Media.

distribution within the device, leading to increased absorption.

### 5.2.2. I–V Characteristics of p–i–n Solar Cells

We constructed the p−i−n structure using a photoactive donor−acceptor blend of ZnPc and $C_{60}$. As electron transport layer (ETL), we use *N*,*N*′-dimethylperylene-3,4,9,10-dicarboxyimide (Me-PTCDI); as hole transport layer (HTL), we use ZnPc. This is similar to a device reported by Rostalski and Meissner.[204] Since the n-type Me-PTCDI layer is the first layer on the ITO substrate in this device, we discuss here an n−i−p structure (Figure 45a). The Me-PTCDI layer is doped with rhodamine B and the ZnPc layer with

$F_4$-TCNQ. This structure acts as a reference cell with low-gap transport layers. For the wide-gap structure, we have tested NTCDA (1,4,5,8-naphthalene-tetracarboxylic-dianhydride), Me-NTCDI (*N*,*N*′-dimethyl-3,4,7,8-naphthalene-tetracarboxylic-diimide), and $C_{60}$ for the ETL and *m*-MTDATA and MeO-TPD for the HTL. It turns out that among these materials, $C_{60}$ and MeO-TPD are the best choice, giving the best solar cell performances. Accordingly, the layer sequence of the n−i−p-type device is ITO/n-$C_{60}$/$C_{60}$/ZnPc−$C_{60}$/p-MeO-TPD/p-ZnPc/Au. The reason for using a thin ZnPc layer under the gold electrode is again to obtain a better Ohmic contact behavior. Because this additional ZnPc layer absorbs light but does not contribute to the photocurrent, we have to avoid it in a further optimization step.

Figure 45a shows the current−voltage characteristics of the two n−i−p cells with low-gap and wide-gap transport layers, respectively. The characteristic parameters for the low-gap sample are an open circuit voltage of 0.45 V, a short circuit current density of 3.7 mA/cm$^2$, a fill factor of 45%, and a power efficiency of 0.75%, which are comparable to literature.[204] For the wide-gap cell, we observe a nearly doubled short circuit current, which is mainly attributed to lower parasitic absorption losses. The corresponding performance values of this cell are 0.46 V, 6.1 mA/cm$^2$, 47%, and 1.32%, respectively. We therefore achieve an almost 2-fold enhancement of the device performance without any change in the active layer. A linear dependence of the short circuit current on the illumination intensity in the range from 1 to 100 mW/cm$^2$ confirms the sufficient transport properties of the donor−acceptor blend without direct bimolecular recombination losses. Figure 45b shows the external quantum efficiency spectrum (IPCE) of the wide-gap cell. It peaks at 40% in the first absorption band of ZnPc between 640 and 700 nm. A second peak appears at 380 nm with a value of 17%, which is attributed to an additional smaller contribution from the $C_{60}$ in the blended layer. To avoid parasitic absorption in this range, it is obviously not ideal to use $C_{60}$ also for the electron transport layer. An integration of the IPCE spectrum over the AM 1.5 spectrum yields a photocurrent of 5.1 mA/cm$^2$ for a light intensity of 100 mW/cm$^2$, which is a bit below the measured short circuit current of 6.1 mA/cm$^2$. Because the IPCE measurements are carried out in ambient atmosphere, we attribute the difference mainly to a degradation of the sample, which is not encapsulated.

### 5.2.3. Modeling of the Optical Properties

To model the optical properties of our multilayer system, a transfer matrix formalism (TMF) is applied.[205−208] More details on the modeling can be found in Hoppe et al.[209] For the modeling, we chose a device with the layer sequence ITO/p-MeO-TPD/ZnPc−$C_{60}$/$C_{60}$/n-$C_{60}$/Al; that is, we have a p−i−n arrangement, in contrast to the previous n−i−p arrangement. The benefit is that we avoid the additional contact layer (ZnPc) under the metal electrode. The contacts ITO/p-MeO-TPD and n-$C_{60}$/Al are close to Ohmic. Here, we see another advantage of the wide-gap p−i−n concept, namely, that we can freely choose the stacking direction.

To find out the best position of the active region with respect to the maximum of the optical field distribution, we vary in the simulation the thicknesses of both transport layers, keeping the active layer unchanged. The thickness of the MeO-TPD layer has hardly any influence on the device performance because (i) its absorption in the visible range is negligible and (ii) the reflection coefficient at the ITO/MeO-TPD interface is low so that interference effects that depend on the MeO-TPD thickness play a minor role.[76] For a $C_{60}$ thickness of 40 nm, the active region is placed at the maximum of the optical field distribution and the photocurrent has a maximal value of 8.75 mA/cm$^2$. Comparing model and experiments, we can derive an internal quantum efficiency of around 82%.[76] We want to emphasize that this value of 82% is not the efficiency at one suitable wavelength but the internal efficiency averaged over the complete absorption range of ZnPc and $C_{60}$.

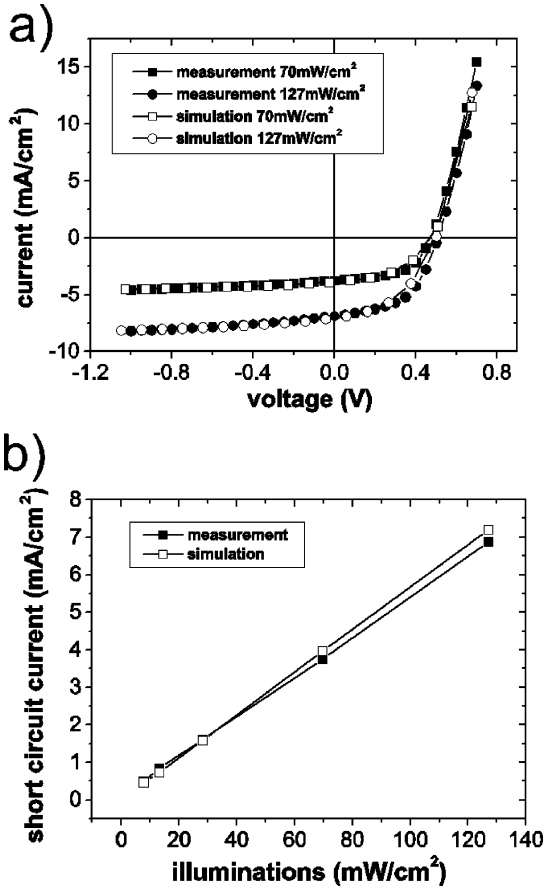


**Figure 46.** (a) *I*−*V* characteristics of a photovoltaic cell consisting of ITO/*p*-MeO-TPD/ZnPc−$C_{60}$/*n*-$C_{60}$/Al under illumination with 127 mW/cm$^2$. The empty symbols describe the simulation results; the filled symbols represent the measured data. (b) Linear dependence of short circuit current vs illumination for the same cell. The line with empty squares describes the simulation results; the full squares represent the measured data. Reprinted from ref 76, Copyright 2004, with kind permission of Springer Science and Business Media.

### 5.2.4. Modeling of the Electrical Properties

In order to obtain a deeper physical insight into the critical parameters of the device, we have set up a numerical model for the electrical properties of the p−i−n-type heterojunction solar cells.[76] The numerical simulation is based on a quasi-one-dimensional iteration algorithm proposed initially by Staudigel et al. to calculate the field distribution in organic light-emitting diodes.[210]

As model solar cell, the ITO/p-MeO-TPD/ZnPc−$C_{60}$/$C_{60}$/n-$C_{60}$/Al structure is simulated. To get an optimum agreement between the simulated and experimental current−voltage characteristics, we adjust the recombination rates, the trap density, and the resistance of ITO. Figure 46 presents the fitting of *I*−*V* curves for an illumination of 127 and 70 mW/

$cm^2$ white light. Here, the main limitations for the forward current are from ITO with about 150 Ω for the given contact geometry and of the photoactive blend layer, while the doped transport layers hardly play any role. To obtain quantitative results from the simulation, it will be necessary to have reliable independent measurements of the carrier mobility in the blend layer because, in a certain range, one can achieve equally good fits with either high mobility values and fast recombination or lower mobility and slower recombination.

A striking feature of the experimental curves is the slope of the $I-V$ curves at reverse bias, which cannot be interpreted in terms of a shunt resistance because the $I-V$ curves show very low reverse currents in the dark. Therefore, this slope is rather a hint for field-dependent recombination losses. At high fields, the carriers have a higher probability to leave the blend layer before recombination. This recombination affects both the short circuit photocurrent and the fill factor. However, the probability for direct bimolecular recombination of free carriers should increase with the illumination level, that is, the concentration of photogenerated charges, which is in contradiction to our finding that the short circuit photocurrent scales exactly linearly with illumination. Consequently, we have to introduce deep trap states that mediate recombination and provide the dominant recombination path. One might as well account for the observed behavior by assuming a field-dependent geminate recombination. However, the assumption of trap-induced recombination agrees better with the empirical finding that the slope of the reverse characteristics under illumination depends sensitively on the purity of the used materials. As shown in Figure 46, good agreement between experiment and simulation for different illumination levels was obtained assuming discrete levels of traps with concentration about $8.5 \times 10^{17}$ $cm^{-3}$. Figure 46b shows the linear dependence of a short circuit current on illumination in the range from 8 to 127 $mW/cm^2$ both in experiment and in simulation and confirms the good agreement.

### 5.2.5. Stacked p–i–n Cells

The single p−i−n devices shown in the previous sections feature good device characteristics with high fill factor and high internal quantum efficiencies (IQE). However, to achieve high power efficiencies, both IQE and absolute absorption need to be high. The single p−i−n cells suffer from too low absorption in two respects. At first, the absorption spectrum of the active layer of ZnPc and $C_{60}$ does not cover the complete visible range. The main absorption bands of the two materials rather leave a gap in the spectra between 420 and 600 nm where we observe only little absorption by weakly forbidden transitions in $C_{60}$. Second, the photoactive blend layers have to be very thin to avoid recombination losses and space charge limitation of the current flow. Therefore, they are optically thin even at the absorption maxima.

An approach to overcome these problems is to stack several junctions with either identical or complementary absorption spectra on top of each other. This concept has been demonstrated by Yakimov and Forrest who used single donor−acceptor heterojunctions of CuPc and a perylene dye (PTCBI) for the individual cells.[211] A maximum power conversion efficiency of 2.5% for the double stacked cell was reached. The open-circuit voltage ($V_{oc}$) can, in principle, be equal to the sum of the open-circuit voltages of the individual cells. The flow of photocurrent in stacked junction cells requires an efficient recombination of charge carriers with low energetic losses at the interface between the individual cells. This requirement could be met by depositing an ultrathin interfacial layer of silver clusters to create recombination centers. It is probable that these clusters also induce a favorable interface dipole. Otherwise, a pair of carriers would dissipate energy equal to the difference in the quasi-Fermi levels between the PTCBI and the CuPc upon recombination, which is exactly the energy stored in a photogenerated carrier pair. However, within this approach, thin film optics limits the application of stacking.

In our approach, we use the basic p−i−n cell, explained in the previous sections, as an optimized building block that can be introduced into a final stacked solar cell structure. The advantage compared with the investigation of Yakimov et al.[211] are the spacer layers between each photoactive layer sequence, namely, the wide-gap transport layers. The active layers of each single cell can thus be placed at the position of maximum optical field strength. With high doping of those transport layers, low Ohmic losses are expected. In Yakimov's studies, it turned out that stacking more than two junctions does not yield a further increase in power efficiency. The reason is probably that they cannot avoid placing one of the cells in a minimum of the optical field distribution. This is a severe drawback for the overall performance because it is always the cell with the lowest photocurrent generation that limits the overall photocurrent because several cells are connected in series. As explained before, Forrest et al. have also used doped transport layers (*m*-MTDATA), resulting in a tandem cell with 5.7% power efficiency.[197] In this cell, both photoactive layers are placed close to each other to profit from the same maximum of optical field.

Our approach of using p−i−n cells as a building block for stacking has the advantage that the recombination zone between the individual cells is placed between wide-gap transport layers so that they are hidden from excitons in the active layers. After all, within Yakimov's approach, one can hardly avoid that recombination centers for charge carriers act as recombination centers for excitons as well.

Figure 47 depicts the device structure for twofold stacked p−i−n cells. A schematic energy level diagram is given as well. The individual cells are built up similarly to the p−i−n cells described above. Between these cells, we introduce an ultrathin gold layer. It has been shown that metal layers as thin as a few nanometers grow in discontinuous layers.[210,212] In fact, the metal forms clusters that act as defects and improve interface recombination and generation dynamics at reverse and forward bias voltage, respectively.

To study the recombination and generation behavior at interfaces between highly p- and n-doped wide-gap layers, we use a somewhat simpler test structure that comprises one p−i−n cell and, instead of an Ohmic top contact on the n-layer, an additional p-layer with an Ohmic top contact to the p-layer. We call this arrangement a p−i−n cell with an electron-to-hole conversion contact.

Although such cells with conversion contact comprise a p−n junction with the opposite polarity with respect to the p−i−n junction, they may behave just as p−i−n junctions with Ohmic contacts if the doping level is high enough and carriers can tunnel through the p−n junction barrier. However, we have found that despite the high doping levels used here (2−4%), the contact performance improves significantly when an additional ultrathin metal layer is introduced

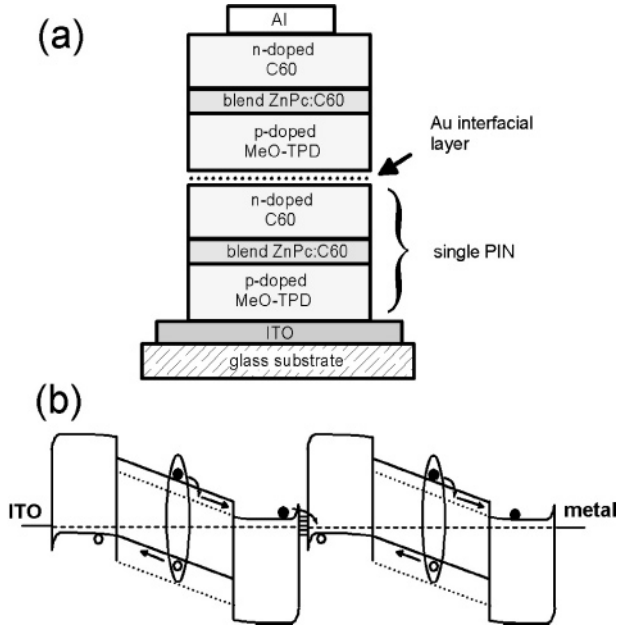


**Figure 47.** Organic solar cells based on multiple stacked p−i−n structures, each of them comprising a photoactive layer sandwiched between p- and n-type wide-gap transport layers: (a) layer sequence for a double p−i−n cell based on photoactive ZnPc−$C_{60}$ blend layers; (b) schematic energy level diagram for the cell shown in panel a in thermal equilibrium showing HOMO and LUMO levels and the Fermi level. In the blend layers, the solid lines represent the levels of ZnPc and the dashed lines those of $C_{60}$. The thin layer of metal clusters between the two p−i−n cells is represented by a series of discrete energy levels that assist recombination via tunneling. Reprinted from ref 76, Copyright 2004, with kind permission of Springer Science and Business Media.

between the p- and the n-layer of the conversion contact. This effect is demonstrated in Figure 48a where we compare two identical samples with the layer sequence ITO/50 nm p-doped MeO-TPD/30 nm blend ZnPc−$C_{60}$ (1:1)/30 nm n-doped $C_{60}$/1 nm Au (only sample B)/30 nm p-doped MeO-TPD/10 nm p-doped ZnPc/40 nm Au, that is, two samples that differ only by the thin gold interlayer of 1 nm. The 10 nm p-doped ZnPc layer ensures in all cases good Ohmic contact to the metal electrode.[213] Both samples are prepared simultaneously on the same substrate so that thickness variations can be excluded. The reverse currents under illumination coincide for both samples, which shows that the 1 nm gold layer hardly causes any absorption losses. However, sample B with gold interlayer features a smooth curve with a high fill factor (FF = 0.45), whereas sample A is s-shaped leading to a lower fill factor (FF = 0.32). Also, the forward currents are strongly decreased for sample A, which indicates limited generation of charge carriers at the interface at forward bias voltage. The gold interlayer provides gap states that assist tunneling through the p−n junction barrier. Therefore, we conclude that the function of the metal interlayer is somewhat different from those used in stacked undoped heterojunction cells.[211]

Next, we will show that the doping of the transport layers is indeed necessary within our approach: In Figure 48b, we compare again two samples with the device structure given in Figure 48a. However, we here dope either only one side of the conversion contact or both sides. All samples contain the interfacial layer of 1 nm of gold. As expected, only the characteristics of the cell doped on both sides of the interfacial metal layer indicates quasi-Ohmic behavior with high forward currents and a good fill factor. Obviously,

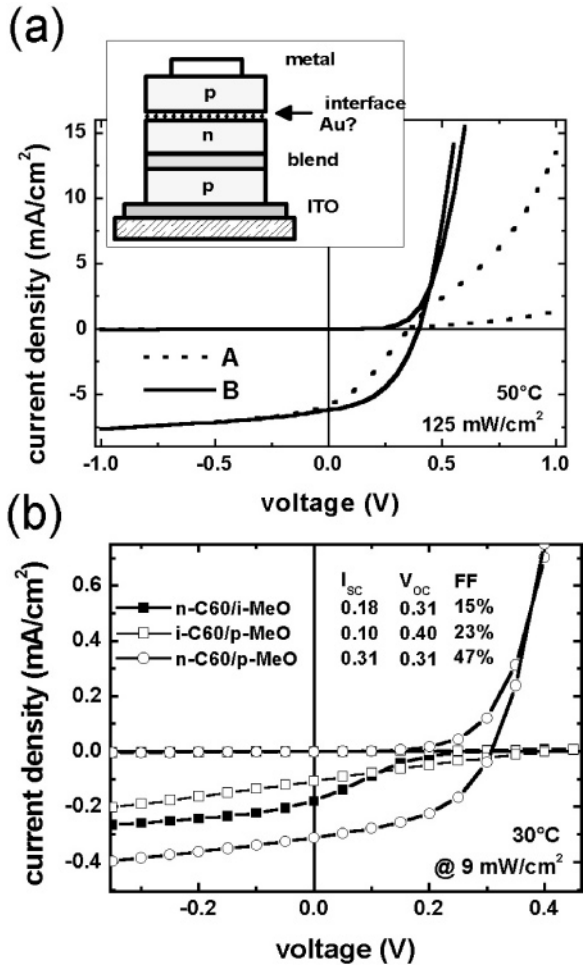


**Figure 48.** The influence of an ultrathin metal interlayer and of doping on "electron-to-hole conversion" contacts. The two samples shown here have the layer sequence ITO/50 nm p-doped MeO-TPD/30 nm ZnPc−$C_{60}$ (1:1)/30 nm n-doped $C_{60}$/1 nm Au (only sample B)/30 nm p-doped MeO-TPD/10 nm p-doped ZnPc/40 nm Au (see inset of panel a): (a) current−voltage characteristics in the dark and under 125 mW/cm$^2$ white light illumination for samples with an interlayer of 1 nm gold (sample A) and without this layer (sample B); (b) current−voltage characteristics in the dark and under 9 mW/cm$^2$ white light for samples with p- and n-doping in the layers adjacent to the conversion contact (○), with p-doping only (□), and with n-doping only (■). The solar cell performance parameters are given as an inset. Only samples with p- and n-doping and with the gold interlayer show smooth characteristics with high fill factor. Reprinted from ref 76, Copyright 2004, with kind permission of Springer Science and Business Media.

recombination and generation at the interface are efficient and do not create relevant losses. On the other hand, the cells with one undoped layer suffer from low forward currents. In contrast to Yakimov's stacked cells, the metal interlayer alone is not sufficient, here, to ensure easy recombination and generation at the interface. We rather have to provide very thin depletion layers on both sides of the interface to allow for easy tunneling.

Finally, we discuss the preparation of a complete tandem cell. The optimum tandem cell configuration was found with an optical simulation based on the optical constants of the layers.[76] The $I-V$ characteristics of an optimized tandem cell are given in Figure 49, together with the characteristics of the first single cell. The tandem cell exhibits a significantly higher power efficiency of 3.8% ± 0.2% compared with the single p−i−n cell (2.1% ± 0.2%) under 130 mW/cm$^2$ simulated AM 1.5 illumination. The open-circuit voltage of

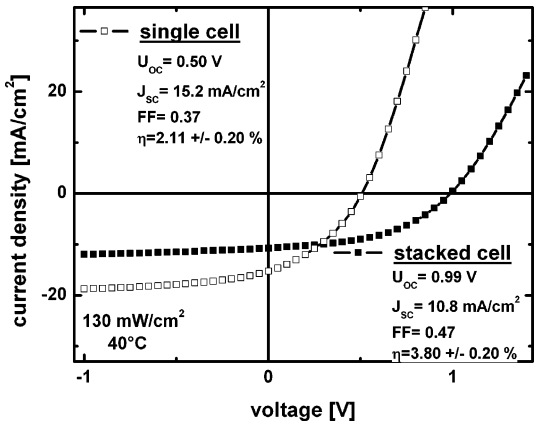


**Figure 49.** *I*−*V* characteristics of single and tandem p−i−n solar cells under 130 mW/cm$^2$ simulated AM 1.5 solar illumination. The tandem cell has an optimized device structure according to the distance of the two blend layers (see Figure 50), and the single cell is identical to the bottom cell in the tandem configuration prepared simultaneously. The performance parameters are given. Reused with permission from J. Drechsel, B. Männig, F. Kozlowski, M. Pfeiffer, K. Leo, and H. Hoppe, *Applied Physics Letters*, *86*, 244102 (2005). Copyright 2005, American Institute of Physics.

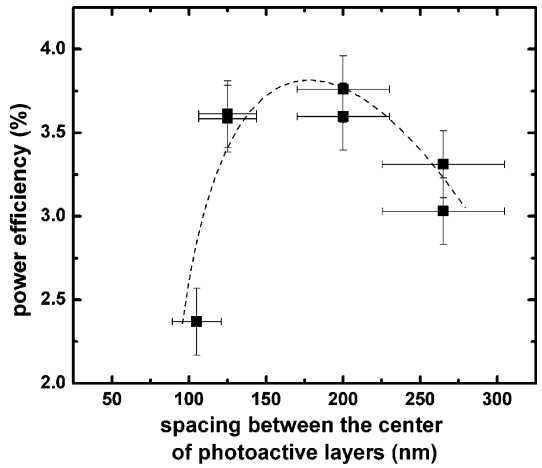


**Figure 50.** Power efficiencies for p−i−n tandem cells plotted vs the distance between the centers of the photoactive layers. The device structure has been kept constant except for the separating hole transport layer between the active layers of the tandem cell. The dashed line represents a guide for the eyes. Reused with permission from J. Drechsel, B. Männig, F. Kozlowski, M. Pfeiffer, K. Leo, and H. Hoppe, *Applied Physics Letters*, *86*, 244102 (2005). Copyright 2005, American Institute of Physics.

$V_{oc}$ = 0.99 V is doubled as compared with the single p−i−n cell ($V_{oc}$ = 0.50 V). The short circuit current of the tandem cell is reduced but still clearly exceeds one-half of the value of the single cell. We also note a remarkably improved fill factor of 0.47 for the tandem cell, as compared with 0.36 for the single cell, which we attribute mainly to the reduced impact of the series resistance. Additionally, the smaller thickness of the active blend layer (50 nm) in the tandem cell lowers the overall recombination losses of the complete device.

The *I*−*V* characteristics of the tandem cell show a reasonable saturation of the photocurrent with negative voltage. As both geminate and nongeminate recombination losses should be field dependent, we suggest that this saturation current corresponds to a recombination-free situation, that is, close to 100% internal quantum efficiency. If we compare the saturation value of 12.5 mA/cm$^2$ at 130 mW/cm$^2$ illumination with the simulated maximum photocurrents of 9.8 mA/cm$^2$ (exclusively blend layer) and 12.0 mA/cm$^2$ (blend layer and adjacent $C_{60}$), we conclude that indeed the neat $C_{60}$ contributes to the photocurrent. The reasonable agreement between experiment and calculation confirms the model.

In Figure 50, the power efficiencies of a series of stacked p−i−n cells are depicted as a function of the distance of the centers of the photoactive blend layers of the two cells. Except for the thickness of the hole transport layer of cell B (doped MeO-TPD), all thicknesses of transport layers and photoactive layers have been kept constant. A maximum shows up around the proposed optimized configuration, which confirms the optical model.

### *5.2.6. Efficient Heterojunction Organic Solar Cells with High Photovoltage Containing a Low-Gap Oligothiophene Derivative*

Finally, we discuss an example for a solar cell where the importance of the Fermi level control by doping for solar cells is demonstrated. In the cells mentioned above, the photoactive materials used are mostly ZnPc and $C_{60}$. However, the combined absorption spectra of these two materials show a pronounced minimum at around 530 nm.

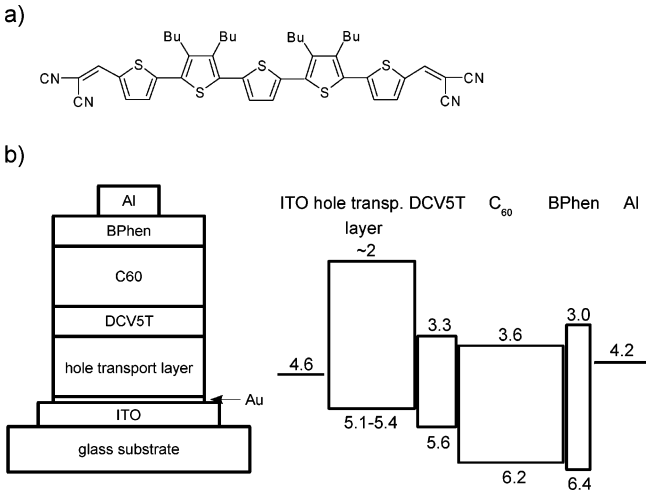


**Figure 51.** (a) Chemical structure of DCV5T and (b) structure and energy level alignment of the photovoltaic cells using a p-doped hole transport layer, an intrinsic layer of DCV5T and $C_{60}$, an exciton blocking layer, and an aluminum contact (data from refs 123 and 215−217; DCV5T, HOMO level determined with UPS, LUMO level determined with cyclic voltammetry in $CH_2Cl_2$). Reprinted with permission from ref 214. Copyright 2006 the International Society of Optical Engineering (SPIE).

To achieve an optimum coverage of the visible spectrum, one should therefore integrate an additional photoactive material into the device architecture that fills this gap. Perylene-based dyes such as Me-PTCDI having an absorption maximum at around 530 nm can be a proper choice. Recently, we have introduced a new oligothiophene α,α′-bis-(2,2-dicyanovinyl)-quinquethiophene (DCV5T; Figure 51a) comprising five α-conjugated thiophene rings (5T), substituted with two electron-withdrawing dicyanovinylene (DCV) groups at the terminal position.[214] This material shows an absorption maximum at 573 nm and acts as donor in heterojunctions in combination with the fullerene $C_{60}$. The oligothiophene carries electron-withdrawing substituents, which increase the ionization energy and even more strongly the electron affinity. In thin films, the absorption is significantly broadened compared with solution, and the optical

gap is reduced to 1.77 eV. Nevertheless, the material shows strong fluorescence with low Stokes shift (peak at 1.71 eV), that is, low energy loss upon reorganization in the excited state.

The charge separation process at the interface of DCV5T and $C_{60}$ involves only low energetic losses since both the HOMO and the LUMO offset of the two materials are below 0.6 eV, close to the expected exciton binding energy. We can thus reach high open-circuit voltages of up to 1.0 V. The most efficient solar cells are obtained when the photoactive heterojunction is embedded between a p-doped hole transport layer on the anode side and a combination of a thin exciton blocking layer and aluminum on the cathode side (Figure 51). Here, it is important to emphasize that the FF sensitively depends on the work function of the p-doped hole transport layer, which can be influenced by the doping ratio of the hole transport layer.[214] The highly doped HTL increases the hole injection behavior because a higher amount of dopant molecules lowers the Fermi level of the hole transport layer. In that way, holes lose less free energy when they leave the DCV5T toward the hole transport layer, and on the other hand, they can be injected more easily into the oligothiophene, which leads to better aligned forward current characteristics.

With these photovoltaic cells, open-circuit voltages of up to 1 V could be reached. Unfortunately, due to the high energetic barrier between the HOMO of the hole transport layer and the oligothiophene, the $I-V$ curve shows a characteristic S-shape, which lowers the fill factor. Especially a higher doping of the hole transport layer increases the hole injection and leads to FF of up to 49%.[214] After taking the spectral mismatch between the sun simulator used in the work and the AM 1.5 sun into account, solar cells with a power efficiency of $3.4\% \pm 0.3\%$ at 118 mW/cm$^2$ simulated sunlight could be fabricated.[217]

## 6. Summary and Outlook

In this review, we have discussed the controlled doping of organic semiconductors by coevaporation with suitable dopant molecules and its application for highly efficient devices, such as organic LED and organic solar cells. The experimental data show that the conductivities can be raised many orders of magnitude above the conductivity of nominally undoped materials. Due to low mobilities, the conductivity of the materials is still much lower than those of inorganic semiconductors but sufficient for many devices that do not need too high current densities, such as organic light-emitting diodes and solar cells.

Although some basic doping effects like Fermi level shifts can be well compared to the standard behavior of inorganic semiconductors, there are deviations that cannot be explained by the simple models used for crystalline inorganic semiconductors. A detailed understanding of the dependence of conductivity on doping concentration requires models that take effects like localization and percolation into account. While molecular p-type doping has been available for some time, impressive progress has recently also been made for n-type doping, which is more difficult since electrons have to be transferred into rather high-lying orbitals.

We have further discussed that doped organic semiconductors are well suited for device applications. For OLEDs, the conductivities achieved are high enough to avoid significant voltage drops even in thicker layers. A key effect of doping is the generation of Ohmic contacts by tunneling through a thin barrier formed by space charge layers, an effect which works in organic semiconductors very well. This is particularly important for OLED devices where the nominally undoped transport layers have required extensive measures to achieve low barriers at the interfaces and have made the devices very sensitive to the contact properties. It has been demonstrated that doped transport layers allow realization of very efficient inverted top-emitting and transparent OLED devices.

The application of doped transport layers to organic solar cells has progressed much less than that for OLEDs. Again, one key advantage is the decoupling of the electrical and optical optimization, which allows the placement of the active region of the solar cells at the regions where the optical field is the largest. Other points are that the use of doped window layers allows the extension of the quasi-Fermi level splitting from the active layers in the most efficient way toward the contacts, thus allowing maximum open-circuit voltage independent of the detailed nature of the contact materials.

Many of the aspects of doped organic layers that we have discussed here are directly taken from inorganic semiconductors. It is thus easily predictable that the multitude of device principles that have developed over decades in the field of inorganic semiconductors can be explored as well for organic semiconductors, with some modifications. We thus believe that in the future, there will be ample space for further investigations of organic devices with doped layers.

From a materials perspective, the progress on new organic semiconductors is rather rapid since the commercial application in devices like OLEDs has spurred large interest from industry, and a systematic search for new materials with improved properties has begun. Part of these investigations should also address new dopants, since the experiments and materials being reported here are still a very small part of what is possible.

## 7. Acknowledgments

The authors wish to thank all co-workers at Dresden involved in theses studies: Jan Blochwitz-Nimoth, Jens Drechsel, Karsten Fehse, Torsten Fritz, Kentaro Harada, Gufeng He, Qiang Huang, Jingsong Huang, Rudolf Lessmann, Fenghong Li, Rico Meerheim, Rico Schüppel, Kerstin Schulze, Gregor Schwartz, Christian Uhrich, Ansgar Werner, Xiang Zhou, and many others who cannot be mentioned here. We thank the groups of Neal R. Armstrong, Peter Bäuerle, Vladimir Dyakonov, C. Michael Elliott, Stephen Forrest, Andreas Hinsch, Norbert Karl, Hannes Lichte, Jürgen Parisi, Paul Simon, and N. Serdar Sariciftci for fruitful collaboration. Further, we thank Fraunhofer-IPMS and the companies Creaphys GmbH, Heliatek GmbH, and Novaled AG for continued collaboration. We acknowledge valuable discussions with Neal Armstrong, Stephen Forrest, Horst Hartmann, Harald Hoppe, Antoine Kahn, Junji Kido, Michael Niggemann, Ingo Riedel, Roland Schmechel, Karin Schmidt, Kazuhiko Seki, Ching Tang, Mark Thomson, Nobuo Ueno, and Hartmut Yersin. We thank Dominik Gronarz for extensive technical assistance in preparing this report. Finally, we acknowledge the continuous funding by the European Commission, German Ministry for Education and Research, German Ministry for Economy and Labor, Deutsche Forschungsgemeinschaft, Free State of Saxony, and further funding agencies. One of us (K.L.) thanks the Deutsche Forschungsgemeinschaft for the support via the Leibniz Prize, which has been a major impetus for the work presented here.

## 8. References


(1) Forrest, S. R. *Chem. Rev.* **1997**, *97*, 1793.
(2) Hung, L. S.; Chen, C. H. *Mater. Sci. Eng.* **2002**, *R 39*, 143.
(3) Berner, D.; Houili, H.; Leo, W.; Zuppiroli, L. *Phys. Status Solidi A* **2005**, *202*, 9.
(4) *Chem. Mater.* **2004**, *16* (23), Special issue on organic electronics.
(5) Peumans, P.; Yakimov, A.; Forrest, S. R. *J. Appl. Phys.* **2003**, *93*, 3693.
(6) *MRS Bull.*, **2005**, *30* (1), Special issue: Organic Based Photovoltaics.
(7) Karl, N. *Defect Control in Semiconductors*; North Holland: Amsterdam, 1990; Vol. II.
(8) Tang, C. W. *Appl. Phys. Lett.* **1986**, *48*, 183.
(9) Tang, C. W.; Van Slyke, S. A. *Appl. Phys. Lett.* **1987**, *51*, 913.
(10) Pfeiffer, M.; Beyer, A.; Fritz, T.; Leo, K. *Appl. Phys. Lett.* **1998**, *73*, 3202.
(11) Zhou, X.; Pfeiffer, M.; Blochwitz, J.; Werner, A.; Nollau, A.; Fritz, T.; Leo, K. *Appl. Phys. Lett.* **2001**, *78*, 410.
(12) Blochwitz, J.; Pfeiffer, M.; Fritz, T.; Leo, K.; Alloway, D. M.; Lee, P. A.; Armstrong, N. R. *Org. Electron.* **2001**, *2*, 97.
(13) Maennig, B.; Pfeiffer, M.; Nollau, A.; Zhou, X.; Leo, K.; Simon, P. *Phys. Rev. B* **2001**, *64*, 195208.
(14) Nollau, A.; Pfeiffer, M.; Fritz, T.; Leo, K. *J. Appl. Phys.* **2000**, *87*, 4340.
(15) Werner, A. G.; Li, F.; Harada, K.; Pfeiffer, M.; Fritz, T.; Leo, K. *Appl. Phys. Lett.* **2003**, *82*, 4495.
(16) Werner, A.; Li, F.; Harada, K.; Pfeiffer, M.; Fritz, T.; Leo, K.; Machill, S. *Adv. Funct. Mater.* **2004**, *14*, 255.
(17) Li, F.; Werner, A.; Pfeiffer, M.; Leo, K.; Liu, X. *J. Phys. Chem. B* **2004**, *108*, 17076.
(18) Harada, K.; Werner, A. G.; Pfeiffer, M.; Bloom, C. J.; Elliott, C. M.; Leo, K. *Phys. Rev. Lett.* **2005**, *94*, 036601.
(19) Pope, M.; Swenberg, C. E. *Electronic processes in organic molecular crystals*; Oxford University Press: New York, 1982.
(20) Seeger, K. *Semiconductor Physics*; Springer-Verlag: Berlin Heidelberg New York, 1997.
(21) Yamamoto, Y.; Yoshino, K.; Inuishi, Y. *J. Phys. Soc. Jpn.* **1979**, *47*, 1887.
(22) Parthasarathy, G.; Shen, C.; Kahn, A.; Forrest, S. R. *J. Appl. Phys.* **2001**, *89*, 4986.
(23) Kido, J.; Matsumoto, T. *Appl. Phys. Lett.* **1998**, *73*, 2866.
(24) Endo, J.; Matsumoto, T.; Kido, J. *Jpn. J. Appl. Phys., Part 2* **2002**, *41* (3B), L358.
(25) Kearns, D. R.; Tollin, G.; Calvin, M. J. *Chem. Phys.* **1960**, *32*, 1020.
(26) Maitrot, M.; Guillaud, G.; Boudjema, B.; André, J. J.; Simon, J. *J. Appl. Phys.* **1986**, *60*, 2396.
(27) Andre, J. J.; Simon, J.; Even, R.; Boudjema, B.; Guillaud, G.; Maitrot, M. *Synth. Met.* **1987**, *18*, 683.
(28) Marks, T. J. *Science* **1985**, *227*, 881.
(29) Lous, E. J.; Blom, P. W. M.; Molenkamp, L. W.; de Leeuw, D. M. *Phys. Rev. B* **1995**, *51*, 17251.
(30) Pfeiffer, M.; Fritz, T.; Blochwitz, J.; Nollau, A.; Plönnigs, B.; Beyer, A.; Leo, K. *Adv. Solid State Phys.* **1999**, *39*, 77.
(31) Blochwitz, J.; Pfeiffer, M.; Fritz, T.; Leo, K. *Appl. Phys. Lett.* **1998**, *73*, 729.
(32) Huang, J. S.; Pfeiffer, M.; Werner, A.; Blochwitz, J.; Leo, K.; Liu, S. Y. *Appl. Phys. Lett.* **2002**, *80*, 139.
(33) Zhou, X.; Pfeiffer, M.; Huang, J. S.; Blochwitz-Nimoth, J.; Qin, D. S.; Werner, A.; Drechsel, J.; Maennig, B.; Leo, K. *Appl. Phys. Lett.* **2002**, *81*, 922.
(34) Blochwitz, J.; Pfeiffer, M.; Hofmann, M.; Leo, K. *Synth. Met.* **2002**, *127*, 169.
(35) Pfeiffer, M.; Beyer, A.; Plönnigs, B.; Nollau, A.; Fritz, T.; Leo, K.; Schlettwein, D.; Hiller, S.; Wöhrle, D. *Sol. Energy Mater. Sol. Cells* **2000**, *63*, 83.
(36) Gebeyehu, D.; Maennig, B.; Drechsel, J.; Leo, K.; Pfeiffer, M. *Sol. Energy Mater. Sol. Cells* **2003**, *79*, 81.
(37) Fritzsche, H. *Solid State Commun.* **1971**, *9*, 1813.
(38) Pfeiffer, M.; Leo, K.; Zhou, X.; Huang, J. S.; Hofmann, M.; Werner, A.; Blochwitz-Nimoth, J. *Org. Electron.* **2003**, *4*, 89.
(39) Shirota, Y.; Kuwabara, Y.; Inada, H. *Appl. Phys. Lett.* **1994**, *65*, 807.
(40) Gao, W.; Kahn, A. *Appl. Phys. Lett.* **2001**, *79*, 4040.
(41) Yoshida, M.; Fujii, A.; Ohmori, Y.; Yoshino, K. *Appl. Phys. Lett.* **1996**, *69*, 734.
(42) Shirota, Y. *J. Mater. Chem.* **2000**, *10*, 1.
(43) Borsenberger, P. M.; Fitzgerald, J. J. *J. Phys. Chem.* **1993**, *97*, 4815.
(44) Krause, R. Diploma Thesis, TU Dresden, 2005.
(45) Adachi, C.; Kwong, R.; Forrest, S. R. *Org. Electron.* **2001**, *2*, 37.
(46) Görlich, P.; Schneider, H. G.; Hamann, C. *Organische Festkörper und dünne Schichten;* Akademische Verlagsgesellschaft: Berlin, 1978.
(47) Hiller, S.; Schlettwein, D.; Armstrong, N. R.; Wöhrle, D. *J. Mater. Chem.* **1998**, *8*, 945.
(48) Hoffmann, M.; Schmidt, K.; Fritz, T.; Hasche, T.; Agranovich, V. M.; Leo, K. *Chem. Phys. Lett.* **2000**, *258*, 73.
(49) Pfeiffer, M. Ph.D. thesis, TU Dresden, 1999.
(50) Garnier, F.; Horowitz, G.; Peng, X. Z.; Fichou, D. *Synth. Met.* **1991**, *45*, 163.
(51) Sze, S. M. *Physics of Semiconductor Devices*; Wiley: New York, 1981.
(52) Cheon, K. O.; Shinar, J. *Appl. Phys. Lett.* **2002**, *81*, 1738.
(53) Vissenberg, M. C. J. M.; Matters, M. *Phys. Rev. B* **1998**, *57*, 12964.
(54) Schmechel, R. *Phys. Rev. B* **2002**, *66*, 235206.
(55) Schmechel, R. *J. Appl. Phys.* **2003**, *93*, 4653.
(56) Ivory, D. M.; Miller, G. G.; Sowa, J. M.; Shacklette, L. W.; Chance, R. R.; Baughman, R. H. *J. Chem. Phys.* **1979**, *71*, 1506.
(57) Ramsey, M. G.; Steinmüller, D.; Netzer, F. P. *Phys. Rev. B* **1990**, *42*, 5902.
(58) Itoh, Y.; Tomikawa, N.; Kobayashi, S.; Minato, T. *Extended Abstracts. The 51th Autumn Meeting, The Japan Society of Applied Physics*, Tokyo, 1990; p 1040.
(59) Kido, J.; Nagai, K.; Okamoto, Y. *IEEE Trans. Electron Devices* **1993**, *40*, 1342.
(60) Mason, M. G.; Tang, C. W.; Hung, L. S.; Raychaudhuri, P.; Madathil, J.; Giesen, D. J.; Yan, L.; Le, Q. T.; Gao, Y.; Lee, S. T.; Liao, L. S.; Cheng, L. F.; Salaneck, W. R.; dos Santos, D. A.; Bredas, J. L. *J. Appl. Phys.* **2001**, *89*, 2756.
(61) Grozea, D.; Turak, A.; Feng, X. D.; Lu Z. H.; Johnson, D.; Wood, R., *Appl. Phys. Lett.* **2002**, *81*, 3173.
(62) T. Mori, T.; Fujikawa, H.; Tokito, S.; Taga, Y. *Appl. Phys. Lett.* **1998**, *73*, 2763.
(63) Kido, J.; Matsumoto, T. *Appl. Phys. Lett.* **1998**, *73*, 2866.
(64) Tanaka, S.; Kanai, K.; Kawabe, E.; Iwahashi, T.; Nishi, T.; Ouchi, Y.; Seki, K. *Jpn. J. Appl. Phys.* **2005**, *44*, 3760.
(65) Chan, C. K.; Amy, F.; Zhang, Q.; Barlow, S.; Marder, S.; Kahn, A. *Chem. Phys. Lett.* **2006**, *431*, 67.
(66) Bloom, C. J.; Elliott, C. M.; Schroeder, P. G.; France, C. B.; Parkinson, B. A. *J. Phys. Chem. B* **2003**, *107*, 2933.
(67) See www.novaled.com.
(68) Morris, D. E.; Hanck, K. W.; de Armond, M. K. *J. Electroanal. Chem.* **1983**, *149*, 115.
(69) Redox potentials can be related to an absolute energy scale by 0 V vs. $Ag/Ag^+ = 4.7$ eV, see: Bard, A.; Faulkner, L. R. *Electrochemical methods*; Wiley: New York, 2001.
(70) Schlettwein, D.; Hesse, K.; Gruhn, N. E.; Lee, P. A.; Nebesny, K. W.; Armstrong, N. R. *J. Phys. Chem. B* **2001**, *105*, 4791.
(71) Gregg, B. A.; Chen, S.; Branz, H. M. *Appl. Phys. Lett.* **2004**, *84*, 1707.
(72) Chan, C.; Kim, E.-G.; Brédas, J.-L.; Kahn, A. *Adv. Funct. Mater.* **2006**, *16*, 831.
(73) Lewis, E. S.; Perry, J. M.; Grinstein, R. H. *J. Am. Chem. Soc.* **1970**, *92*, 899.
(74) Naguib, Y. M. A.; Cohen, S. G.; Steel, C. *J. Am. Chem. Soc.* **1986**, *108*, 128.
(75) Yamamoto, S.; Sakurai, T.; Liu, Y. J.; Sueishi, Y. *Phys. Chem. Chem. Phys.* **1999**, *1*, 833.
(76) Maennig, B.; Drechsel, J.; Gebeyehu, D.; Simon, P.; Kozlowski, F.; Werner, A.; Li, F.; Grundmann, S.; Sonntag, S.; Koch, M.; Leo, K.; Pfeiffer, M.; Hoppe, H.; Meissner, D.; Saricifci, N. S.; Riedel, I.; Parisi, J. *Appl. Phys. A* **2004**, *79*, 1.
(77) Gao, W.; Kahn, A. *Appl. Phys. Lett.* **2003**, *82*, 4815.
(78) Seki, K.; Yanagi, H.; Kobayashi, Y.; Ohta, T.; Tani, T. *Phys. Rev. B* **1994**, *49*, 2760.
(79) Hirose, Y.; Kahn, A.; Aristov, V.; Soukiassian, P. *Appl. Phys. Lett.* **1996**, *68*, 217.
(80) Hill, I. G.; Rajagopal, A.; Kahn, A.; Hu, Y. *Appl. Phys. Lett.* **1998**, *73*, 662.
(81) Koch, N.; Kahn, A.; Ghijsen, J.; Pireaux, J.-J.; Schwartz, J.; Johnson, R. L.; Elschner, A. *Appl. Phys. Lett.* **2003**, *82*, 70.
(82) Cahen, D.; Kahn, A. *Adv. Mater.* **2003**, *15*, 271.
(83) Vazquez, H.; Flores, F.; Oszwaldowski, R.; Ortega, J.; Perez, R.; Kahn, A. *Appl. Surf. Sci.* **2004**, *234*, 107.
(84) Gao, W.; Kahn, A. *J. Phys.: Condens. Matter* **2003**, *15*, 82757.
(85) Xue, J.; Forrest, S. R. *Phys. Rev. B* **2004**, *69*, 245322.
(86) Koch, N.; Duhm, S.; Rabe, J. P.; Vollmer, A.; Johnson, R. L. *Phys. Rev. Lett.* **2005**, *95*, 237601.
(87) Yamashita, K.; Kunugi, Y.; Harima, Y.; Chowdhury, A. *Jpn. J. Appl. Phys.* **1995**, *34*, 3794.
(88) Hamm, S.; Wachtel, H. *J. Chem. Phys.* **1995**, *103*, 10689.
(89) Shockley, W. *Bell Syst. Tech. J.* **1949**, *28*, 435.
(90) van Berkel, C.; Powell, M. J.; Franklin, A. R.; French, I. D. *J. Appl. Phys.* **1993**, *73*, 5264.
(91) Kroon, M. A.; van Swaaij, R. A. C. M. M. *J. Appl. Phys.* **2001**, *90*, 994.
(92) Taretto, K.; Rau, U.; Werner, J. H. *Appl. Phys. A* **2003**, *77*, 865.
(93) Bernanose, A.; Comte, M.; Vouaux, P. *J. Chim. Phys.* **1953**, *50*, 64.

(94) Bernanose, A.; Vouaux, P. *J. Chim. Phys.* **1953**, *50*, 261.
(95) Tang, C. W.; Van Slyke, S. A. *Appl. Phys. Lett.* **1987**, *51*, 913.
(96) Burroughes, J. H.; Bradley, D. D. C.; Brown, A. R.; Marks, R. N.; Mackay, K.; Friend, R. H.; Burn, P. L.; Holmes, A. B. *Nature* **1990**, *347*, 539.
(97) Prototypes announced in press releases by Seiko-Epson (2004) and Samsung (2005).
(98) Meerheim, R.; Walzer, K.; He, G.; Pfeiffer, M.; Leo, K. *Proc. SPIE* **2006**, *6192*, 61920P/1.
(99) Kawamura, Y.; Goushi, K.; Brooks, J.; Brown, J. J.; Sasabe, H.; Adachi, C. *Appl. Phys. Lett.* **2005**, *86*, 071104.
(100) Baldo, M. A.; O'Brien, D. F.; You, Y.; Shoustikov, A.; Sibley, S.; Thompson, M. E.; Forrest, S. R. *Nature* **1998**, *395*, 151.
(101) O'Brien, D. F.; Baldo, M. A.; Thompson, M. E.; Forrest, S. R. *Appl. Phys. Lett.* **1999**, *74*, 442.
(102) Baldo, M. A.; Lamansky, S.; Burrows, P. E.; Thompson, M. E.; Forrest, S. R. *Appl. Phys. Lett.* **1999**, *75*, 4.
(103) Yersin, H. *Top. Curr. Chem.* **2004**, *241*, 1.
(104) Greenham, N. C.; Friend, R. H.; Bradley, D. C. C. *Adv. Mater.* **1994**, *6*, 491.
(105) Shiga, T.; Fujikawa, H.; Taga, Y. *J. Appl. Phys.* **2003**, *93*, 19.
(106) Feng, J.; Okamoto, T.; Kawata, S. *Appl. Phys. Lett.* **2005**, *87*, 241109.
(107) Tsutsui, T.; Yahiro, M.; Yokogawa, H.; Kawano, K. *Adv. Mater.* **2001**, *13*, 1149.
(108) Lupton, J. M.; Matterson, B. J.; Samuel, I. D. W.; Jory, M. J.; Barnes, W. L. *Appl. Phys. Lett.* **2000**, *77*, 3340.
(109) Huang, Q.; Walzer, K.; Pfeiffer, M.; Leo, K.; Hofmann, M.; Stübinger, T. *J. Appl. Phys.* **2006**, *100*, 064507.
(110) Sun, Y.; Forrest, S. R. *J. Appl. Phys.* **2006**, *100*, 073106.
(111) Lu, M. H.; Sturm, J. C. *J. Appl. Phys.* **2002**, *91*, 595.
(112) Drechsel, J.; Pfeiffer, M.; Zhou, X.; Nollau, A.; Leo, K. *Synth. Met.* **2002**, *127*, 201.
(113) Drechsel, J.; Petrich, A.; Koch, M.; Pfützner, S.; Meerheim, R.; Scholz, S.; Drechsel, J.; Walzer, K.; Pfeiffer, M.; Leo, K. *SID Symp Dig. Tech. Pap.* **2006**, *37*, 1692.
(114) Yamamori, A.; Adachi, Ch.; Koyama, T.; Taniguchi, Y. *Appl. Phys. Lett.* **1998**, *72*, 2147.
(115) Shirota, Y.; Kobata, T.; Noma, N. *Chem. Lett.* **1989**, *7*, 1145.
(116) Shirota, Y. *J. Mater. Chem.* **2005**, *15*, 75.
(117) Zhou, X.; Blochwitz, J.; Pfeiffer, M.; Nollau, A.; Fritz, T.; Leo, K. *Adv. Funct. Mater.* **2001**, *11*, 310.
(118) Hung, L. S.; Tang, C. W.; Mason, M. G. *Appl. Phys. Lett.* **1997**, *70*, 152.
(119) Pfeiffer, M.; Forrest, S. R.; Leo, K.; Thompson, M. E. *Adv. Mater.* **2002**, *14*, 1633.
(120) Meerheim, R.; Walzer, K.; Pfeiffer, M.; Leo, K. *Appl. Phys. Lett.* **2006**, *89*, 061111.
(121) Zhou, X.; Qin, D. S.; Pfeiffer, M.; Blochwitz-Nimoth, J.; Werner, A.; Drechsel, J.; Maennig, B.; Leo, K.; Bold, M.; Erk, P.; Hartmann, H. *Appl. Phys. Lett.* **2002**, *81*, 4070.
(122) He, G.; Schneider, O.; Qin, D.; Zhou, X.; Pfeiffer, M.; Leo, K. *J. Appl. Phys.* **2004**, *95*, 5773.
(123) He, G.; Pfeiffer, M.; Leo, K.; Hofmann, M.; Birnstock, J.; Pudzich, R.; Salbeck, J. *Appl. Phys. Lett.* **2004**, *85*, 3911.
(124) Watanabe, S.; Agata, Y.; Tanaka, D.; Kido, J. *J. Photopolym. Sci. Technol.* **2005**, *18*, 83.
(125) Gebeyehu, D.; Walzer, K.; He, G.; Pfeiffer, M.; Leo, K.; Brandt, J.; Gerhard, A.; Stössel, P.; Vestweber, H. *Synth. Met.* **2005**, *148*, 205.
(126) Ben Kalifa, M.; Vaufrey, D.; Tardy, J. *Org. Electron.* **2004**, *5*, 187.
(127) Wellmann, Ph.; Hofmann, M.; Zeika, O.; Werner, A.; Birnstock, J.; Meerheim, R.; He, G.; Walzer, K.; Pfeiffer, M.; Leo, K. *J. Soc. Inf. Display* **2005**, *13*, 393.
(128) Birnstock, J.; Hofmann, M.; Murano, S.; Vehse, M.; Blochwitz-Nimoth, J.; Huang, Q.; He, G.; Pfeiffer, M.; Leo, K. *SID Int. Symp. Dig. Tech. Pap.* **2005**, *36*, 40.
(129) He, G.; Walzer, K.; Pfeiffer, M.; Leo, K.; Pudzich, R.; Salbeck, J. *Proc. SPIE* **2004**, *5519*, 42.
(130) Birnstock, J.; Lux, A.; Ammann, M.; Wellmann, P.; Hofmann, M.; Stübinger, Th. *SID Int. Symp. Dig. Tech. Pap.* **2006**, *37*, 1866.
(131) Tanaka, D.; Sasabe, H.; Li, Y. J.; Su, S. J.; Takeda, T.; Kido, J. *Jpn. J. Appl. Phys.* **2007**, *46*, L10.
(132) Kido, J.; Kimura, M.; Nagai, K. *Science* **1995**, *267*, 1332.
(133) Deshpande, R. S.; Bulovic, V.; Forrest, S. R. *Appl. Phys. Lett.* **1999**, *75*, 888.
(134) Cheon, K. O.; Shinar, J. *Appl. Phys. Lett.* **2002**, *81*, 1738.
(135) Xie, Z. Y.; Huang, J. S.; Li, C. N.; Liu, S. Y.; Wang, Y.; Li, Y. Q.; Shen, J. C. *Appl. Phys. Lett.* **1999**, *74*, 641.
(136) Jiang, X.; Zhang, Z.; Zhao, W.; Zhu, W.; Zhang, B.; Xu, S. *J. Phys. D: Appl. Phys.* **2000**, *33*, 473.
(137) Adamovich, V.; Brooks, J.; Tamayo, A.; Alexander, A. M.; Djurovich, P. I.; D'Andrade, B. W.; Adachi, C.; Forrest, S. R.; Thompson, M. E. *New J. Chem.* **2002**, *26*, 1171.
(138) Tokito, S.; Iijima, T.; Tsuzuki, T.; Sato, F. *Appl. Phys. Lett.* **2003**, *83*, 2459.
(139) D'Andrade, B. W.; Forrest, S. R. *J. Appl. Phys.* **2003**, *94*, 3101.
(140) Cheng, G.; Li, F.; Duan, Y.; Feng, J.; Liu, S.; Qiu, S.; Lin, D.; Ma, Y.; Lee, S. T. *Appl. Phys. Lett.* **2003**, *82*, 4224.
(141) Qin, D.; Tao, Y. *Appl. Phys. Lett.* **2005**, *86*, 113507.
(142) Schwartz, G.; Walzer, K.; Pfeiffer, M.; Leo, K. *Proc. SPIE* **2006**, *6192*, 61920Q/1.
(143) Sun, Y.; Giebink, N. C.; Kanno, H.; Ma, B.; Thompson, M. E.; Forrest, S. R. *Nature* **2006**, *440*, 908.
(144) Schwartz, G.; Fehse, K.; Pfeiffer, M.; Walzer, K.; Leo, K. *Appl. Phys. Lett.* **2006**, *89*, 083509.
(145) Thompson, J.; Blyth, R. I. R.; Mazzeo, M.; Anni, M.; Gigli, G.; Cingolani, R. *Appl. Phys. Lett.* **2001**, *79*, 560.
(146) Mazzeo, M.; Pisignano, D.; Della Sala, F.; Thompson, J.; Blyth, R. I. R.; Gigli, G.; Cingolani, R.; Sotgiu, G.; Barbarella, G. *Appl. Phys. Lett.* **2003**, *82*, 334.
(147) Duggal, A. R.; Shiang, J. J.; Heller, C. M.; Foust, D. F. *Appl. Phys. Lett.* **2002**, *80*, 3470.
(148) D'Andrade, B. W.; Forrest, S. R. *Adv. Mater.* **2004**, *16*, 1585.
(149) Huang, Y. S.; Jou, J. H.; Weng, W. K.; Liu, J. M. *Appl. Phys. Lett.* **2002**, *80*, 2782.
(150) Chuen, C. H.; Tao, Y. T.; Wu, F. I.; Shu, C. F. *Appl. Phys. Lett.* **2004**, *85*, 4609.
(151) Gue, F.; Ma, D.; Wang, L.; Jin, X.; Wang, F. *Semicond. Sci. Technol.* **2005**, *20*, 310.
(152) Li, G.; Shinar, J. *Appl. Phys. Lett.* **2003**, *83*, 5359.
(153) Kanno, H.; Sun, Y.; Forrest, S. R. *Appl. Phys. Lett.* **2005**, *86*, 263502.
(154) D'Andrade, B. W.; Forrest, S. R.; Chwang, A. B. *Appl. Phys. Lett.* **2003**, *83*, 3858.
(155) Huang, Q.; Walzer, K.; Pfeiffer, M.; Lyssenko, V.; He, G.; Leo, K. *Appl. Phys. Lett.* **2006**, *88*, 113515.
(156) Lin, C. L.; Cho, T. Y.; Chang, C. H.; Wu, C. C. *Appl. Phys. Lett.* **2006**, *88*, 081114.
(157) Cho, T. Y.; Lin, C. L.; Wu, C. C. *Appl. Phys. Lett.* **2006**, *88*, 111106.
(158) Pfeiffer, M.; Forrest, S. R.; Zhou, X.; Leo, K. *Org. Electron.* **2003**, *4*, 21.
(159) Fehse, K.; Walzer, K.; He, G.; Pfeiffer, M.; Leo, K.; Lövenich, W.; Elschner, A. *Proc. SPIE* **2006**, *6192*, 61921Z/1.
(160) Fehse, K.; Walzer, K.; Leo, K.; Lövenich, W.; Elschner, A. *Adv. Mater.* **2007**, *19*, 441.
(161) Kreye, D.; Toerker, M.; Vogel, U.; Amelung, J. *SID Int. Symp. Dig. Tech. Pap.* **2006**, *37* (2), 979.
(162) Cho, T. Y.; Lin, C. L.; Wu, C. C. *Appl. Phys. Lett.* **2006**, *88*, 111106.
(163) Ikai, M.; Tokito, S.; Sakamoto, Y.; Suzuki, T.; Taga, Y. *Appl. Phys. Lett.* **2001**, *79*, 156.
(164) Huang, J.; Pfeiffer, M.; Blochwitz, J.; Werner, A.; Salbeck, J.; Liu, S.; Leo, K. *Jpn. J. Appl. Phys.* **2001**, *40*, 6630.
(165) Huang, J.; Blochwitz-Nimoth, J.; Pfeiffer, M.; Leo, K. *J. Appl. Phys.* **2003**, *93*, 838.
(166) Dobbertin, T.; Werner, O.; Meyer, J.; Kammoun, A.; Schneider, D.; Riedl, T.; Becker, E.; Johannes, H.-H.; Kowalsky, W. *Appl. Phys. Lett.* **2003**, *83*, 5071.
(167) Tardy, J.; Ben Khalifa, M.; Vaufrey, D. *Mater. Sci. Eng. C* **2006**, *26*, 196.
(168) Zhu, X. L.; Sun, J. X.; Peng, H. J.; Meng, Z. G.; Wong, M.; Kwok, H. S. *Appl. Phys. Lett.* **2005**, *87*, 083504.
(169) Shaheen, S. E.; Brabec, C. J.; Padinger, F.; Fromherz, T.; Hummelen, J. C.; Sariciftci, N. S. *Appl. Phys. Lett.* **2001**, *78*, 841.
(170) Gebeyehu, D.; Brabec, C. J.; Padinger, F.; Fromherz, T.; Hummelen, J. C.; Badt, D.; Schindler, H.; Sariciftci, N. S. *Synth. Met.* **2001**, *118*, 1.
(171) Brabec, C. J.; Sariciftci, N. S.; Hummelen, J. C. *Adv. Funct. Mater.* **2001**, *11*, 15.
(172) Padinger, F.; Rittberger, R. S.; Sariciftci, N. S. *Adv. Funct. Mater.* **2003**, *13*, 85.
(173) O'Regan, B.; Grätzel, M. *Nature* **1991**, *353*, 737.
(174) Loutfy, R. O.; Sharp, J. H. *J. Chem. Phys.* **1979**, *71*, 1211.
(175) Antoniadis, H.; Hsieh, B. R.; Abkowitz, M. A.; Stolka, M.; Jenekhe, S. A. *Polym. Prepr.* **1993**, *34*, 490.
(176) Antoniadis, H.; Hsieh, B. R.; Abkowitz, M. A.; Stolka, M.; Jenekhe, S. A. *Synth. Met.* **1994**, *62*, 265.
(177) Riess, W.; Karg, S.; Dyakonov, V.; Meier, M.; Schwoerer, M. *J. Lumin.* **1994**, *60*, 906.
(178) Yu, G.; Zhang, C.; Heeger, A. J. *Appl. Phys. Lett.* **1994**, *64*, 1540.
(179) Karg, S.; Riess, W.; Dyakonov, V.; Schwoerer, M. *Synth. Met.* **1993**, *54*, 427.
(180) Tada, K.; Onoda, M.; Nakayama, H.; Yoshino, K. *Synth. Met.* **1999**, *102*, 982.
(181) Jenekhe, S. A.; Yi, S. *Appl. Phys. Lett.* **2000**, *77*, 2635.
(182) Granström, M.; Petritsch, K.; Arias, A. C.; Lux, A.; Andersson, M. R.; Friend, R. H. *Nature* **1998**, *395*, 257.

(183) Sariciftci, N. S.; Braun, D.; Zhang, C.; Srdanov, V. I.; Heeger, A. J.; Stucky, G.; Wudl, F. *Appl. Phys. Lett.* **1993**, *62*, 585.
(184) Yu, G.; Gao, J.; Hummelen, J. C.; Wudl, F.; Heeger, A. J. *Science* **1995**, *270*, 1789.
(185) Ma, W.; Yang, C.; Gong, X.; Lee, K.; Heeger, A. J. *Adv. Funct. Mater.* **2005**, *15*, 1617.
(186) Koster, L. J. A.; Mihailetchi, V. D.; Blom, P. W. M. *Appl. Phys. Lett.* **2006**, *88*, 093511.
(187) Hiramoto, M.; Fujiwara, H.; Yokoyama, M. *J. Appl. Phys.* **1992**, *72*, 3781.
(188) Hiramoto, M.; Suemori, K.; Yokoyama, M. *Jpn. J. Appl. Phys.* **2002**, *41*, 2763.
(189) Pannemann, Ch.; Dyakonov, V.; Parisi, J.; Hild, O.; Wöhrle, D. *Synth. Met.* **2001**, *121*, 1585.
(190) Murgia, M.; Biscarini, F.; Cavallini, M.; Taliani, C.; Ruani, G. *Synth. Met.* **2001**, *121*, 1533.
(191) Rostalski, J.; Meissner, D. *Sol. Energy Mater. Sol. Cells* **2000**, *61*, 87.
(192) Wöhrle, D.; Meissner, D. *Adv. Mater.* **1991**, *3*, 129.
(193) Petritsch, K.; Dittmer, J. J.; Marseglia, E. A.; Friend, R. H.; Lux, A.; Rozenberg, G. G.; Moratti, S. C.; Holmes, A. B. *Sol. Energy Mater. Sol. Cells* **2000**, *61*, 63.
(194) Peumans, P.; Forrest, S. R. *Appl. Phys. Lett.* **2001**, *79*, 126.
(195) Peumans, P.; Yakimov, A.; Forrest, S. R. *J. Appl. Phys.* **2003**, *93*, 3693.
(196) Hiramoto, M.; Suezaki, M.; Yokoyama, M. *Chem. Lett.* **1990**, *19*, 327.
(197) Xue, J.; Uchida, S.; Rand, B. P.; Forrest, S. R. *Appl. Phys. Lett.* **2004**, *85*, 5757.
(198) Xue, J.; Rand, B. P.; Uchida, S.; Forrest, S. R. *Adv. Mater.* **2005**, *17*, 66.
(199) Hiramoto, M.; Ihara, K.; Yokoyama, M. *Jpn. J. Appl. Phys.* **1995**, *34*, 3803.
(200) Hiramoto, M.; Ihara, K.; Fukusumi, H.; Yokoyama, M. *J. Appl. Phys.* **1995**, *78*, 7153.
(201) Law, K.-Y. *Chem. Rev.* **1993**, *93*, 449.
(202) Simon, J.; Andre, J.-J. *Molecular Semiconductors*; Springer-Verlag: Berlin, 1985.
(203) Drechsel, J.; Maennig, B.; Kozlowski, F.; Pfeiffer, M.; Leo, K.; Hoppe, H. *Appl. Phys. Lett.* **2005**, *86*, 244102.
(204) Meissner, D.; Rostalski, J. *Sol. Energy Mater. Sol. Cells* **2000**, *61*, 87.
(205) Petterson, L. A. A.; Roman, L. S.; Inganäs, O. *J. Appl. Phys.* **1999**, *86*, 487.
(206) Harbecke, B. *Appl. Phys. B* **1986**, *39*, 165.
(207) Heavens, O. S. *Optical properties of thin solid films*; Dover Publications: New York, 1991.
(208) Furman, S. A.; Tikhonravov, A. V. *Basics of Optics of Multilayer Systems*; Frontiers: Paris, 1996.
(209) Hoppe, H.; Arnold, N.; Sariciftci, N. S.; Meissner, D. *Sol. Energy Mater. Sol. Cells* **2003**, *80*, 105.
(210) Staudigel, J.; Stössel, M.; Steuber, F.; Simmerer, J. *J. Appl. Phys.* **1999**, *86*, 3895.
(211) Yakimov, A.; Forrest, S. R. *Appl. Phys. Lett.* **2002**, *80*, 1667.
(212) Westphalen, M.; Kreibig, U.; Rostalski, J.; Luth, H.; Meissner, D. *Sol. Energy Mater. Sol. Cells* **2000**, *61*, 97.
(213) Drechsel, J.; Männig, B.; Gebeyehu, D.; Hoppe, H.; Pfeiffer, M.; Leo, K. *Org. Electron.* **2004**, *5*, 175.
(214) Schulze, K.; Uhrich, C.; Schüppel, R.; Leo, K.; Pfeiffer, M.; Brier, E.; Reinold, E.; Bäuerle, P. *Proc. SPIE* **2006**, *6192*, 32.
(215) Sato, N.; Saito, Y.; Shinohara, H. *Chem. Phys.* **1992**, *162*, 433.
(216) Reed, C. A.; Bolskar, R. D. *Chem. Rev.* **2000**, *100*, 1075.
(217) Schulze, K.; Uhrich, C.; Schüppel, R.; Leo, K.; Pfeiffer, M.; Brier, E.; Reinold, E.; Bäuerle, P. *Adv. Mater.* **2006**, *18*, 2872.

CR050156N